

AD-A167 306

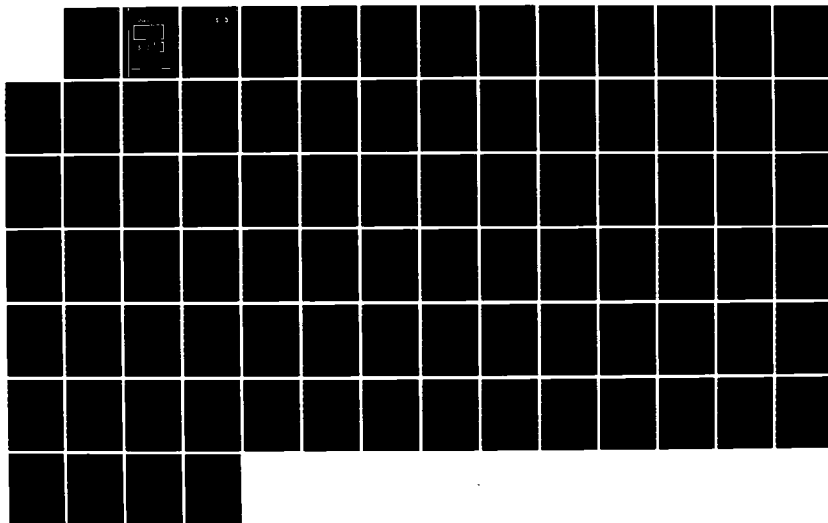
SEMICONDUCTOR ALLOY THEORY(U) AUBURN UNIV ALA DEPT OF
PHYSICS A CHEN 14 JAN 86 AFOSR-TR-86-0160
AFOSR-84-0282

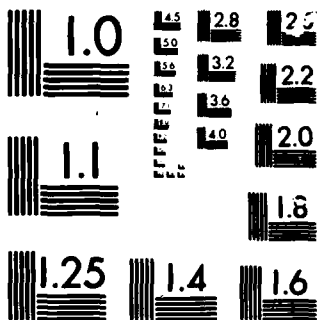
1/1

UNCLASSIFIED

F/G 11/6

NL





MICROCOPY

CHART

AFOSR-TR- 86 - 0160

(2)

AD-A167 306

PHYSICS

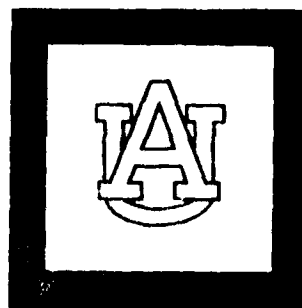
SEMICONDUCTOR ALLOY THEORY

FINAL REPORT

AIR FORCE OFFICE OF SCIENCE RESEARCH

AFOSR-84-0282

DTIC
ELECTE
APR 29 1986
S D



DTIC FILE COPY

AUBURN UNIVERSITY
AUBURN, ALABAMA

Approved for public release;
distribution unlimited.

2

DTIC
ELECTE
APR 29 1986
S D
D

SEMICONDUCTOR ALLOY THEORY
FINAL REPORT
AIR FORCE OFFICE OF SCIENCE RESEARCH
AFOSR-84-0282

September 1, 1984 to December 31, 1985

Submitted by
An-Ban Chen, Physics Department
Auburn University, AL 36849

Date: January 14, 1986

AIR FORCE OFFICE OF SCIENTIFIC RESEARCH (AFOSR)
NOTICE OF TRANSMITTAL TO DTIC
This technical report has been reviewed and is
approved for public release under ESR 190-12.
Distribution is unlimited.
MATTHEW J. KEMPER
Chief, Technical Information Division

Unclassified

SECURITY CLASSIFICATION OF THIS PAGE (When Data Entered)

REPORT DOCUMENTATION PAGE		READ INSTRUCTIONS BEFORE COMPLETING FORM
1. REPORT NUMBER AFOSR-TR- 86-0160	2. GOVT ACCESSION NO. AD-A16	3. RECIPIENT'S CATALOG NUMBER 7306
4. TITLE (and Subtitle) Semiconductor Alloy Theory		5. TYPE OF REPORT & PERIOD COVERED Final 84-9-1 to 85-12-31
7. AUTHOR(s) An-Ban Chen		6. PERFORMING ORG. REPORT NUMBER
9. PERFORMING ORGANIZATION NAME AND ADDRESS Auburn University AL, 36849		8. CONTRACT OR GRANT NUMBER(s) AFOSR-84-0282
11. CONTROLLING OFFICE NAME AND ADDRESS AFOSR/ AND ME Building 410 Boiling AFB DC 20332		10. PROGRAM ELEMENT, PROJECT, TASK AREA & WORK UNIT NUMBERS 61102F 2306/B1
14. MONITORING AGENCY NAME & ADDRESS (if different from Controlling Office)		12. REPORT DATE 86-1-14
		13. NUMBER OF PAGES 7
		15. SECURITY CLASS. (of this report) Unclassified
		15a. DECLASSIFICATION/DOWNGRADING SCHEDULE
16. DISTRIBUTION STATEMENT (of this Report) The United States Government is authorized to reproduce and distribute this report for government purpose Approved for public release; distribution unlimited.		
17. DISTRIBUTION STATEMENT (of the abstract entered in Block 20, if different from Report)		
18. SUPPLEMENTARY NOTES		
19. KEY WORDS (Continue on reverse side if necessary and identify by block number) Electron Mobility, Lattice Relaxation, Bond Length, Bond Energy, Mixing Enthalpies, Band Structure, Core Exciton, Alloy Statistics, Non-random Distribution, Dipolar Energy		
20. ABSTRACT (Continue on reverse side if necessary and identify by block number) See Reverse Side		

DD FORM 1 JAN 73 1473

EDITION OF 1 NOV 65 IS OBSOLETE

Unclassified

SECURITY CLASSIFICATION OF THIS PAGE (When Data Entered)

ABSTRACT

This grant supported our work on semiconductor alloy theory. Many useful results have been obtained, including: (1) generalization of Brooks' formula for alloy-scattering limited electron mobility to including multiple bands and indirect gaps, (2) calculation of SiGe alloys band structure, electron mobility and core-exciton binding energy and linewidth, (3) comprehensive calculation of bond energy, bond length and mixing enthalpy for all III-V and II-VI pseudo-binary alloys, (4) development of a statistical theory which shows a non-random distribution of atoms in most alloys, (5) studying the sensitivity of defect levels to band structures and impurity potentials, (6) a study of the dipolar contribution to the mixing energy and its implication to the long-range order in alloys, e.g., GaAlAs, and (7) a model which allows a simple but detailed calculation of alloy band-edge properties.

SUMMARY

This grant supported our work on semiconductor alloy theory. Through interactions with Dr. Arden Sher's group at SRI International, many useful results have been obtained under this grant. Below we summarize the highlights. The details will be discussed in the publications enclosed with this report.

A. Generalized Brooks' Formula and the Electron Mobility in SiGe Alloy

Although Brooks' formula has been used widely for calculating the alloy-scattering limited electron mobility, we show that this formula is only valid for a direct-gap semiconductor. There are also questions about the scattering parameter and the effective mass. We generalized the formula for indirect-gap alloys with multiple bands and applied it to SiGe alloy. Our results, correlated well with experiments, showed that the electron mobility drops fast with alloying. The mobility has a dip at 15% Si concentration, corresponding a transition from the X to the L edge.

B. Bond Lengths, Lattice Relaxation and Mixing Enthalpies in Semiconductor Alloys

We treated the problem with a model which combines Harrison's bonding theory with a valence force model and an



Dist	Special
A-1	

elastic continuum. While the local strain is the main driving force for the bimodal bond-length distribution in pseudo-binary alloys found in the EXAFS experiment, we found that the chemical shifts arising from different bond lengths and polarities of the constituent bonds can have a significant contribution to the mixing enthalpies. In fact, the sizable negative values of the chemical shifts in the cation substitutional alloys, e.g. $\text{Ga}(x)\text{In}(1-x)\text{As}$, may be important for stabilizing the mixture. We also deduced a simple criterion for separating miscible from immiscible alloys.

C. Sensitivity of Defect Levels to Host Band Structures and Impurity Potentials

Our calculation of defect levels for more than 30 impurities in CdTe showed that the discrepancies caused by different host band structures and impurity potentials ranged from less than 0.1 eV to the whole band gap (1.6 eV). This result casts some doubt about the quantitative nature of the empirical tight binding method for deep-level studies. We also suggested ways to improve the theory.

D. SiGe Alloys - Band Structure and Core-Exciton

SiGe binary alloy has regained research interests recently, because it has a potential for high-speed devices in the strained superlattice configuration. We have applied our

technique to obtain high-quality band structures for Si and Ge, and have performed alloy calculation for $\text{Si}(x)\text{Ge}(1-x)$. The results have been checked against available optical data and have been applied to the mobility calculation mentioned earlier. Another interesting result is that the alloy band parameters allowed us to correlate the Si 2p core-exciton binding energy with its linewidth in the alloy. The observed minimum in the linewidth near $x=0.15$ can be explained as a result of competition between an intrinsic broadening due to screening and an extrinsic alloy scattering. The most reasonable binding energy in pure Si was found to be 0.15 eV. This work thus has helped resolve the controversy about the unusually large binding energy for the core exciton in Si.

E. Calculation of the Alloy Band-Edge Properties

There are two basic techniques for calculating the band structure in semiconductor alloys: empirical formula and detailed theory such as the coherent-potential approximation (CPA). The former is handy to use, but provides very little insight. The latter is usually very time consuming, and for energies near band edges the numerical accuracy is often questionable. For III-V and most of the II-VI pseudo-binary alloys, these difficulties can be circumvented by using perturbation theory. Moreover, the CPA results are sensitive

the band models used for the constituent compounds. By examining the overall structures of the Green's function, partial densities of states, and the tight-binding interaction parameters involved in the band-edge states and in the perturbation theory, we have concluded a procedure for a simple but detailed calculation of the various contributions to the band gap bowing and the low-field electron mobility in these alloys.

F. Dipolar Contribution to Alloy Mixing Energy and Its Implication to Long Range Order

The alloy formation energy (F.E.), defined as the difference between the alloy total energy and the average of the constituents' values, and mixing entropy are two competing factors which govern the alloy thermodynamics. While a negative F.E. favors a long-range order (LRO) at low temperature, a positive F.E. tends to cause spinodal decomposition. It was suggested recently that the long-range electrostatic interaction among cations and anions contributes to a negative F.E., and hence serves as a driving force for the LRO found in GaAlAs grown by MBE and MOCVD. We showed analytically that, when all terms are included, this dipolar contribution to F.E. is positive. Therefore, it is not a force to stabilize the LRO phase. However, the value of the dipolar F.E. in the ordered phase is smaller than that in the disordered one. Since the

initial distribution of atoms in the growth process is closer to the LRO phase than to the spinodally decomposed one, the dipolar force may tend to drive the system toward the former - a metastable phase.

G. Statistics and Micro-clustering in Alloys

One of our major efforts was to develop a statistical theory for semiconductor alloys which will cover three aspects: energetics, statistics and phase diagram. Because of the smallness of the mixing enthalpies, typically several Kcal/mol, the present first-principle theory is not accurate enough for this purpose. We found that a combination of Harrison's model and a valence force field model provides an adequate approach. We then generalized Guggenheim's quasi-chemical approximation to treat the tetrahedral clusters. Our results showed a non-random atomic distributions in most alloys. This non-random distribution will affect the band structure, mobility and mechanical properties of alloys, and will reflect in many measurable properties such as phonon spectra, EXAFS, deep level spectra etc.. The study of these effects is one of our current efforts.

PUBLICATION RESULTED FROM THE WORK UNDER THIS GRANT

1. "Semiconductor Alloys: Local Bond Lengths, Mixing Enthalpies, and Micro-clusters", A.-B. Chen and A. Sher, Mat. Res. Soc. Symp. Proc. Vol 46, 137 (1985).
2. "Sensitivity of Defect Levels to Host Band structures and Impurity potentials in CdTe", A.-B. Chen and A. Sher, Phys. Rev. B31, 6490 (1985).
3. "Dislocation Energies and Hardness of Semiconductors", A. Sher, A.-B. Chen and W. E. Spicer, Appl. Phys. Lett. 46, 54 (1985).
4. "Generalized Brooks' Formula and Electron Mobility in $\text{Si}(x)\text{Ge}(1-x)$ Alloys", S. Krishnamurphy, A. Sher and A.-B. Chen, Appl. Phys. Lett. 47, 54 (1985).
5. "Binding Energy and Spectral Width of Si 2p Core Exciton in $\text{Si}(x)\text{Ge}(1-x)$ Alloys", S. Krishnamurphy, A. Sher and A.-B. Chen, Phys. Rev. Lett. 55, 320 (1985).
6. "Semiconductor Pseudo-Binary Alloys: Bond Length Relaxation and Mixing Enthalpies", A.-B. Chen and A. Sher, Phys. Rev. B32, 3695 (1985).
7. "Band Structure of $\text{Si}(x)\text{Ge}(1-x)$ Alloys", S. Krishnamurphy, A. Sher and A.-B. Chen, Accepted for Publ. in Phys. Rev. B.

THESIS WORK SUPPORTED BY THIS GRANT

"Band-Gap Bowing in III-V and II-VI Semiconductor Pseudo-Binary Alloys", W.-M. Lai-Hsu, Master Thesis, Auburn University, Expected completion date: Spring, 1986.

REPRINTS OF PUBLICATIONS

Semiconductor pseudobinary alloys: Bond-length relaxation and mixing enthalpies

A.-B. Chen

Department of Physics, Auburn University, Alabama 36849

A. Sher

SRI International, Menlo Park, California 94025

(Received 1 March 1985)

Harrison's bonding theory, the valence force field (VFF), and an elastic continuum are combined in a study of the substitution energies Δ_i and local (first-shell) bond lengths d_i of isoelectronic impurities in semiconductors. Explicit expressions for Δ_i and d_i are derived, which enable us to absorb measured elastic constants into the calculation and to study the chemical effects arising from differences in the covalent radii and polarities. Several models based on VFF alone are also derived for comparison. The full theory and at least five VFF models are found to produce impurity bond lengths in excellent agreement with experiment. The substitution energies are shown to provide good estimates of the mixing enthalpies Ω of pseudobinary alloys and to predict miscibility gaps properly. The chemical shifts in Ω are found to be negative for most cation alloys but positive for anion substitutions.

I. INTRODUCTION

The discovery of a bimodal distribution of the nearest-neighbor bond lengths¹ in $\text{Ga}_x\text{In}_{1-x}\text{As}$ has sparked considerable interest in the bonding nature of semiconductor alloys.²⁻⁶ This finding has changed the conventional picture of the alloy crystal bond configuration, which has far-reaching implications about the electronic structure, structural stability, and thermodynamics of these materials. Because of the complexity of both the structural and the potential disorder in these alloys, *ab initio* band-structure techniques have not yet evolved to a stage suitable for direct calculations. Therefore, we have extended Harrison's bonding theory⁷ to study the alloy structural properties.^{8,9} In this paper, we apply an intermediate version of the theory to the dilute-limit case of an isoelectronic impurity.

A particularly useful application of the theory is its perturbation-expansion form, in which measured elastic constants are incorporated to obtain accurate results. This form is also useful for comparison with other previously published models^{3,8,9} that are based on the valence-force-field (VFF) (Ref. 10) model alone. Thus, all the factors influencing bond-length relaxation, e.g., strains, boundary conditions, and chemical effects, can be studied. The ability to incorporate the chemical effects is one major difference between this theory and other VFF models.

The remainder of the paper contains the following sections: Sec. II describes a theory for calculating impurity substitution energies. Section III casts the theory into perturbation form and combines it with a valence force field and an elastic continuum. Several VFF models are derived in Sec. IV. The modifications of numerical results due to chemical effects on local bond lengths and alloy mixing enthalpies are summarized and discussed in Sec. V. Conclusions are drawn in the last section, Sec. VI.

II. IMPURITY-SUBSTITUTION ENERGY

Consider the problem of substituting an isoelectronic atom A for a B atom in a zinc-blende compound BC (e.g., In substitutes for Ga in GaAs, as shown in Fig. 1). In

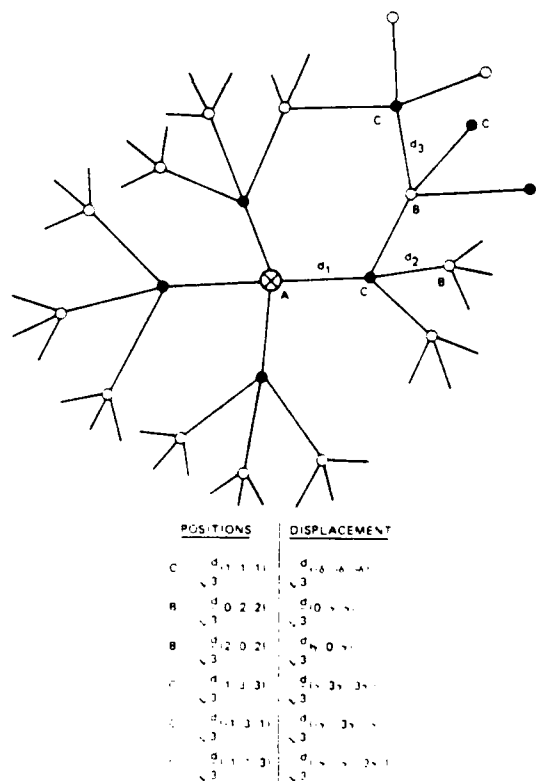


FIG. 1. A sketch of the flattened picture of a single impurity A in a BC compound. The positions and displacements for those atoms labeled are used in Appendix B.

general, the bond lengths d_1, d_2, d_3, \dots for the first-, second-, and third-shell bonds surrounding the impurity are different from the equilibrium values of either the pure BC compound, denoted as d , or the "impurity" compound AC , denoted as $d_I = d(1 - \delta_0)$. If A starts being a free atom and B also ends being a free atom, then the energy difference between the final and initial states is defined as the substitution energy and is given by

$$\Delta_s = (E_{\text{def}} + \epsilon_B) - (E_{\text{pure}} + \epsilon_A), \quad (1)$$

where ϵ_A and ϵ_B are free-atom energies for A and B , respectively, E_{def} is the total energy of the semiconductor with a defect as sketched in Fig. 1, and E_{pure} is that of the pure host BC crystal. Equation (1) can be written as

$$\begin{aligned} \Delta_s &= (E_{\text{def}} - E_{\text{dis}}) - (\epsilon_A - \epsilon_B) + (E_{\text{dis}} - E_{\text{pure}}) \\ &= \Delta_R - (\epsilon_A - \epsilon_B) + \Delta_{\text{dis}}, \end{aligned} \quad (2)$$

where we have added and subtracted a term E_{dis} , which is the total energy of a distorted BC compound with all the atoms held at the positions specified in Fig. 1, except that the central atom is a B atom. Clearly, $\Delta_R = E_{\text{def}} - E_{\text{dis}}$ is a replacement energy, and the distortion energy $\Delta_{\text{dis}} = E_{\text{dis}} - E_{\text{pure}}$ is the energy required to deform a pure BC crystal from its equilibrium lattice to that specified in Fig. 1. Δ_R contains all the chemical terms that arise from different bond lengths and polarities between AC and BC bonds.

Δ_R can be treated most easily by Harrison's bonding theory.⁷ In this theory, the energy per bond relative to the vacuum state is

$$E_b \approx 2\epsilon_b + V_0 + 6\epsilon_m^+ + 6\epsilon_m^-, \quad (3)$$

where ϵ_b is the energy of the bonding state constructed from the two hybrid orbitals facing each other along the bond direction

$$E_b \approx \frac{1}{2}(\epsilon_h^A + \epsilon_h^C) - (V_2^2 + V_3^2)^{1/2}, \quad (4)$$

with ϵ_h^A and ϵ_h^C being the energies of the anion and cation hybrid orbitals, respectively. The antibonding energy ϵ_a has the same form as in Eq. (4), except with a plus sign. V_2 is called the covalent energy, which is the total electronic Hamiltonian matrix element between the two hybrids in question, and the polar energy V_3 is the difference $V_3 = \frac{1}{2}(\epsilon_h^C - \epsilon_h^A)$. The ϵ_m^+ and ϵ_m^- , the metallization energies, are the shifts of the bonding level caused by interactions with the neighboring antibonding states, where $+$ and $-$ indicate whether the common adjacent atom is a cation or anion. For example, this term for an AC bond labeled by d_1 in Fig. 1 due to an antibonding state labeled by d_2 is given by

$$\epsilon_{m,C}^{B,A}(2,1) = \frac{U_b^A(1)^2 \cdot U_a^B(2)^2 \cdot V_1^2}{\epsilon_b^A(1) - \epsilon_b^B(2)}, \quad (5)$$

where A and B denote AC and BC bonds, respectively, $V_1 = \frac{1}{2}(\epsilon_s^C - \epsilon_p^C)$, with ϵ_s^C and ϵ_p^C being the s - and p -term values of the common adjacent atom C . $U_b^A(1)$ is the probability amplitude of finding an electron in the hybrid orbital of the C atom in the bonding state of an AC bond

with a bond length d_1 , whereas $U_a^B(2)$ is the corresponding probability amplitude for the antibonding state of a BC bond of bond length d_2 . Finally, V_0 is a repulsive pair potential required to prevent the crystal from collapsing and to guarantee a correct equilibrium bond length. The local perturbation, Eq. (5), is applicable because the square root of the numerator is much smaller than the separation between the antibonding and bonding levels and the valence band is completely filled, so the interaction between the bonding states only spreads the ϵ_b levels into bands without affecting the center of gravity of the occupied states.

The replacement energy Δ_R of Eq. (2) can now be written explicitly:

$$\begin{aligned} \Delta_R &= 4[2\epsilon_b^A(1) + V_0^A(1) + 6\epsilon_{m,A}^{A,A}(1,1) + 6\epsilon_{m,C}^{B,A}(2,1) \\ &\quad - 2\epsilon_b^B(1) - V_0^B(1) - 6\epsilon_{m,B}^{B,B}(1,1) - 6\epsilon_{m,C}^{B,B}(2,1) \\ &\quad + 6\epsilon_{m,C}^{A,B}(1,2) - 6\epsilon_{m,C}^{B,B}(1,2)]. \end{aligned} \quad (6)$$

The distortion energy Δ_{dis} of Eq. (2) now involves only BC bonds of different bond lengths. It can be treated with exactly the same procedure for any given set of bond-length distributions. Thus, a straightforward energy minimization procedure can be carried out. The accuracy of this procedure, however, depends in turn on the accuracy of scaling rules for V_2 and V_0 and the input parameters. At present, Harrison's model⁷ with $V_2 \propto 1/d^2$ and $V_0 \propto 1/d^4$ and his universal parameters are only semiquantitative. We are improving the quantitative nature of the theory so that the full theory will yield accurate predictions of the structural and thermal properties of semiconductor defects and alloys.

III. PERTURBATION EXPANSION, VALENCE FORCE FIELD, AND ELASTIC MEDIUM

As pointed out earlier, a perturbation expansion of the theory is instructive. This is feasible because the differences $\Delta V_2 = V_2(AC) - V_2(BC)$ and $\Delta V_3 = V_3(AC) - V_3(BC)$ are small compared to each individual value for many of the isoelectronic impurities in III-IV and II-VI compounds. To this end, Eq. (6) is rewritten as

$$\begin{aligned} \frac{1}{4}\Delta_R &= E_b^A(1) - E_b^B(1) + 6[\epsilon_{m,C}^{B,A}(2,1) - \epsilon_{m,C}^{A,A}(1,1)] \\ &\quad - 6[\epsilon_{m,C}^{A,B}(2,1) - \epsilon_{m,C}^{B,B}(1,1)] \\ &\quad + 6[\epsilon_{m,C}^{A,B}(1,2) - \epsilon_{m,C}^{B,B}(2,2)] \\ &\quad - 6[\epsilon_{m,C}^{B,B}(1,2) - \epsilon_{m,C}^{B,B}(2,2)], \end{aligned} \quad (7)$$

where $E_b^A(1)$ and $E_b^B(1)$ are energies per bond in Eq. (3) for AC and BC compounds, respectively, with the relaxed bond length $d_I = d(1 - \delta_I)$. The difference between these energies E_b and the corresponding values at their respective equilibrium bond lengths d_I and d are just the strain energies per bond in uniform deformation:

$$\begin{aligned} E_b^A(1) - E_b^A(d_I) &+ 2\sqrt{3}B_I d_I(d_I - d)^2, \\ E_b^B(1) - E_b^B(d) &+ 2\sqrt{3}B d(d - d_I)^2, \end{aligned} \quad (8)$$

where B_I and B are the bulk moduli for the impurity AC and host BC crystals. The rest of the terms in Eq. (7) are all due to changes in ϵ_m caused by the differences ΔV_3 and ΔV_2 . We shall use Harrison's scaling rules to deduce them.⁷ Expanding Eq. (7) to second order in ΔV_3 and $\Delta d = d_2 - d_1$, we write

$$6[\epsilon_m^B C(2,1) - \epsilon_m^A C(1,1)] \\ = f_I \Delta d - g_I \Delta V_3 + h_I (\Delta d)^2 - W_I \Delta d \Delta V_3 + U_I (\Delta V_3)^2, \quad (9)$$

where f_I, g_I , and so on, are appropriate derivatives evaluated for the impurity crystal AC . When similar expansions are made for the rest of the terms in Eq. (7), it becomes [with $d_1 = d(1-\delta)$, $d_I = d(1-\delta_0)$]

$$\frac{1}{4} \Delta E = \Delta E_b + (f_I - f) \Delta d - (g_I - g) \Delta V_3 + (h_I + h) (\Delta d)^2 \\ - (W_I + W) \Delta d \Delta V_3 + (U_I + U) (\Delta V_3)^2 \\ + 2\sqrt{3} B_I d^3 (\delta - \delta_0)^2 - 2\sqrt{3} B d^3 \delta^2, \quad (10)$$

where

$$\Delta E_b = E_b^A(d_I) - E_b^B(d) - \frac{1}{4} (\epsilon_A - \epsilon_B) \quad (11)$$

is just the difference in the binding energy per bond between the "BC" and "AC" crystals. In Eq. (10) the coefficients f, g without a subscript are those for the host BC system. It is convenient to define an excess energy $\Delta E = \Delta_s/4 - \Delta E_b$, which is the extra energy per bond required for the impurity substitution over and above the binding-energy difference between the BC and AC crystals. The binding-energy difference accounts for much of the substitution energy; however, the correction measured by the excess energy can be significant. The excess energy results from strain energies and chemically driven charge redistributions around the defect. Using Eqs. (2) and (10) and defining $F = f_I - f$ and $G = g_I - g$, we can write ΔE up to second order in ΔV_3 and Δd as

$$\Delta E = 2\sqrt{3} B_I d^3 (\delta - \delta_0)^2 - 2\sqrt{3} B d^3 \delta^2 + F \Delta d - G \Delta V_3 \\ + H (\Delta d)^2 + W \Delta d \Delta V_3 + U (\Delta V_3)^2 + \frac{1}{4} \Delta_{dis}, \quad (12)$$

where $H = h_I + h$, $W = w_I + w$, and $U = u_I + u$.

To treat the distortion energy Δ_{dis} , we divide the crystal into two regions. Inside a sphere of some radius R measured from the impurity, the strain energy is taken to be the valence-force-field¹⁰ value:

$$\Delta_{dis}^{(in)} = \frac{3}{8d^2} \sum_i \alpha_i [\Delta(\mathbf{d}_i \cdot \mathbf{d}_i)]^2 \\ + \frac{3}{8d^2} \sum_i \sum_{(j < i)} \beta_{ij} [\Delta(\mathbf{d}_i \cdot \mathbf{d}_j)]^2, \quad (13)$$

where i sums over all the bonds inside R and the pairs in the β terms include those that have adjacent atoms inside R and on the boundary. The parameters α and β are force constants to be considered later. $\Delta(\mathbf{d} \cdot \mathbf{d}_j) = \mathbf{d} \cdot \mathbf{d}_j - \mathbf{d}_i^{(0)} \cdot \mathbf{d}_j^{(0)}$ measures the change of the dot product between bond vectors due to distortions. Outside R we assume an elastic continuum with radial displacements in-

versely proportional to the square of the distance from the center. The elastic energy in this medium can be shown to be (see Appendix A)

$$\Delta_{dis}^{(out)} = R C u^2, \quad (14)$$

where the effective shear coefficient is

$$C = 4\pi[0.4(C_{11} - C_{12}) + 1.2C_{44}]$$

and u is the displacement at R . In view of the fact that the bonds d_1 and d_2 are coupled through the chemical terms in Eq. (10), the smallest logical radius R is the second-shell atomic distance, namely $R = 2\sqrt{2}d/\sqrt{3}$. Atoms on this boundary have displacements of the forms $\mathbf{u} = d(\gamma, \gamma, 0)/\sqrt{3}, \dots$. Thus, $u = \sqrt{2}\gamma d/\sqrt{3}$ and the elastic energy in the continuum is

$$\Delta_{dis}^{(out)} = \frac{4}{3} \sqrt{2/3} C \gamma^2 d^3. \quad (15)$$

The distortion energy represented by Eq. (14) contains six different contributions (see Appendix B): the bond-stretching energy of the four first-shell bonds $6\alpha\delta^2 d^2$, the β terms from the first-shell bonds, $\beta\delta^2 d^2$, the α terms from the second-shell bonds, $2\alpha(\delta + 2\gamma)^2 d^2$, the β terms between the first- and second-shell bonds, $2\beta(\delta + \gamma)^2 d^2$, the β terms among the second-shell bonds, $2\beta\delta^2 d^2$, and finally the β terms between the second-shell bonds and those in the continuum,

$$\frac{1}{2} \beta d^2 [(3\delta + \lambda_1 \gamma)^2 + (\delta + \lambda_2 \gamma)^2],$$

where $\lambda_1 = 40\sqrt{2}/(19\sqrt{19})$ and $\lambda_2 = 2 - 40\sqrt{2}/(11\sqrt{11})$.

To assemble all the contributions to Eq. (12), we need to consider the assignments of the elastic constants and the force constants α and β in VFF. While the experimental values¹¹ of C_{11} , C_{12} , and C_{44} can be used for the elastic constants, α and β have to be deduced. If Martin's original procedure¹⁰ (also followed by Martins and Zunger³) is used, then Eq. (13) alone will not produce the correct (experimental) bulk moduli. There are small corrections due to Madelung terms, which are hard to treat in the case of nonuniform distortions. A simpler procedure is adopted here. We use the experimental bulk moduli for B_I and B in Eq. (12) and experimental elastic constants to calculate C of Eq. (14) and then force α and β in the VFF to produce the correct bulk moduli B and shear coefficients $C_{11} - C_{12}$. Such an approach is also consistent with Harrison's bonding theory⁷ and other approaches in which the Coulomb forces are automatically incorporated in the band and bond energies, and do not need to be redundantly treated. With our procedure, the bulk modulus is simply related to the force constants by $B = (3\alpha + \beta)/(4\sqrt{3}d)$. Table I lists our α and β values. We want to point out in advance, however, that the numerical results deduced from our sets and those of Martin of α and β do not introduce differences more than the present experimental uncertainties in the local bond length (~ 0.01 Å) and the mixing enthalpies (> 0.5 kcal/mole).

Using the above procedure and adding all contributions, the excess energy per bond from Eqs. (10) and (12) is the full perturbation theory (FPT) result

TABLE I. The bond lengths d (in Å), valence force constants α and β (N/m), shear coefficients C of the continuum (in 10^{11} ergs/cm³), melting temperatures T_m (K), and Liederma ratios χ_m for the compounds used in this paper.

Compound	d	α	β	C	T_m^a	χ_m
AlP	2.367	44.323	8.068	122.396	1773	0.070
AlAs	2.451	40.849	8.717	112.695	1873	0.073
AlSb	2.656	34.073	6.900	85.351	1323	0.062
GaP	2.360	44.764	10.737	145.921	1510	0.064
GaAs	2.448	39.235	9.159	121.844	1738	0.071
GaSb	2.640	31.876	7.347	89.372	985	0.055
InP	2.541	40.363	6.543	91.785	1343	0.059
InAs	2.622	33.203	5.752	78.816	1215	0.061
InSb	2.805	28.557	4.891	60.721	798	0.049
ZnS	2.342	40.429	5.273	89.272	2123	0.081
ZnSe	2.454	32.200	4.562	82.687	1788	0.080
ZnTe	2.637	29.445	4.659	62.430	1511	0.071
CdTe	2.806	26.569	2.722	38.453	1371	0.067
HgTe	2.798	26.396	2.746	40.363	943	0.056

^aReference 30.

$$\Delta E = [3\alpha_I(\delta - \delta_0)^2/2 + \beta_I(\delta - \delta_0)^2/2 + \alpha(\delta + 2\gamma)^2/2 + \beta(\delta + \gamma)^2/2 + \beta\delta^2/4 + \beta(3\delta + \lambda_1\gamma)^2/8 + \beta(\delta + \lambda_2\gamma)^2/4]d^2 + \sqrt{2}C\gamma^2d^3/(3\sqrt{3}) + \Delta E_{ch}, \quad (16)$$

where the chemical contribution is written as

$$\begin{aligned} \Delta E_{ch} &= F_{ch}\Delta d + H(\Delta d)^2 + \Delta E_p \\ &= \frac{2}{3}F_{ch}(2\delta + \gamma)d + \frac{4}{9}H(2\delta + \gamma)^2d^2 \\ &\quad + [U(\Delta V_3)^2 - G\Delta V_3], \end{aligned} \quad (17)$$

where $\Delta F_{ch} = F - W\Delta V_3$ and $\Delta E_p = U(\Delta V_3)^2 - G\Delta V_3$. F_{ch} is a chemical force, which when it is positive tends to push the C atom away from the impurity atom A . This force arises from the difference in the bond tensions induced between the AC and BC bonds adjacent to C because the neighboring antibonding states are different from those of their respective host states. ΔE_p is due to the difference in the polarities ΔV_3 alone and is independent of the displacement. Finally, H can be regarded as a chemically induced force constant, which when it is positive tends to restrain the lattice from distortion and increases the elastic energy.

The equilibrium requirements $\partial(\Delta E)/\partial\delta = 0$ and $\partial(\Delta E)/\partial\gamma = 0$ then lead to the solution $\gamma = Q\delta$, and δ is given by

$$\delta = (\delta_0 + \delta'_0)/[1 + \{\alpha(1 - 2Q) + \beta(17/4 - \lambda Q) + 16H(1 - 2Q)/9\}/(3\alpha_I + \beta_I)], \quad (18)$$

where the constant λ is $1 + 3\lambda_1/4 + \lambda_2/2$, and

$$\delta'_0 = -4F_{ch}(1 - Q/2)/[3d(3\alpha_I + \beta_I)], \quad (19)$$

with $Q = 2J/K$, $J = \alpha + \lambda\beta/2 + 8H/9$, and

$$K = 4\alpha + 2\sqrt{2}Cd/(3\sqrt{3}) + (1 + \lambda_1^2/4 + \lambda_2^2/2)\beta + 8H/9.$$

IV. VALENCE-FORCE-FIELD MODELS

In this section we consider several models based on the valence force field. These models have been used frequently to explain the impurity bond relaxation.^{3,4,8,9} We shall first derive the explicit expressions for these models and then connect them with the existing results.

A. Model A: Third-shell atoms and beyond are fixed at their pure crystal positions

Let the bond lengths surrounding the impurity again be $d_1 = d(1 - \delta)$ and let the second-shell atoms have radial displacements of the forms $(d/\sqrt{3})$, $(\gamma, \gamma, 0)$, etc. Beyond and including the third shell, all the other atoms are held at their pure-crystal positions. There are nine different contributions to the strain energy in VFF (see Appendix B): the α terms from the four bonds surrounding the impurity, $6\alpha_I(\delta - \delta_0)^2d^2$; the β terms among the six pairs of these bonds, $\beta_I(\delta - \delta_0)^2d^2$; the β terms between the first- and second-shell bonds, $2\beta(\delta + \gamma)^2d^2$; the α terms from the second-shell bonds, $2\alpha(\delta + 2\gamma)^2d^2$; the β terms among the second-shell bonds, $2\beta\delta^2d^2$; the β terms between the second- and third-shell bonds, $\frac{9}{2}\beta\delta^2d^2 + \beta(\delta + 2\gamma)^2d^2$; the α terms from the third-shell bonds, $8\alpha\gamma^2d^2$; the β terms among the third-shell bonds, $4\beta\gamma^2d^2$; and the β terms between the third- and fourth-shell bonds, $6\beta\gamma^2d^2$. Thus,

the excess energy (in this case $\frac{1}{4}$ times the strain energy) becomes

$$\Delta E = \left[\frac{1}{2} \alpha_I (\delta - \delta_0)^2 + \frac{1}{4} \beta_I (\delta - \delta_0)^2 + \frac{1}{2} \beta (\delta + \gamma)^2 + \frac{1}{2} \alpha (\delta + 2\gamma)^2 + \frac{11}{8} \beta \delta^2 + \frac{1}{4} \beta (\delta + 2\gamma)^2 + 2\alpha\gamma^2 + \frac{1}{2} \beta \gamma^2 \right] d^2. \quad (20)$$

The minimization of ΔE with respect to δ and γ leads Eq. (20) to $\gamma = -\delta/4$, and

$$\delta = \delta_0 / [1 + (\alpha + 17\beta/2) / (6\alpha_I + \beta_I)]. \quad (21)$$

We note that there is some ambiguity in the third contribution listed above for the β terms between the impurity and host bonds. The value of β could be chosen as one of these combinations β , β_I , $\frac{1}{2}(\beta + \beta_I)$, $\sqrt{\beta\beta_I}$, or other proper combinations. Because the values of β and β_I are comparable and β values are much smaller than α (see Table I), the results for δ and ΔE are not too sensitive to the choice. There is also some ambiguity in the values for $d_i^{(0)}$, $d_j^{(0)}$ for the "undistorted" crystal. The $-d^2/3$ used is the simplest choice. A different choice will not affect the results for δ at all, but will make ΔE slightly different. In fact, model A was first used by Martins and Zunger.³ However, their expression for δ is different from Eq. (21) because they made different choices of the two quantities just mentioned. Nevertheless, Sec. IV will show that these two expressions yield very similar results. These ambiguities do not occur in the full theory in Sec. III, where the impurity-host interactions are taken into account naturally by the replacement energy Δ_R [see Eq. (10)].

B. Model B: Second-shell atoms connect to a fixed boundary

This model corresponds to $\gamma = 0$ in model A. So we have

$$\Delta E = \left[\frac{1}{2} \alpha_I (\delta - \delta_0)^2 + \frac{1}{4} \beta_I (\delta - \delta_0)^2 + \frac{1}{2} \alpha (\delta + 2\gamma)^2 + \frac{1}{2} \beta (\delta + \gamma)^2 + \frac{1}{2} \beta \delta^2 + \frac{1}{8} \beta (3\delta + \lambda_1 \gamma)^2 + \frac{1}{4} \beta (\delta + \lambda_2 \gamma)^2 + \frac{\sqrt{2}}{3\sqrt{3}} C d \gamma^2 \right] d^2, \quad (26)$$

where λ_1 and λ_2 are the same as the constants that appear in Eq. (16). The corresponding equilibrium condition can be shown to be

$$\delta = \delta_0 / \{ 1 + [\alpha(1 - 2Q) + 19\beta/4 - \beta(1 + 3\lambda_1/4 + \lambda_2/4)Q] / (3\alpha_I + \beta_I/2) \}. \quad (27)$$

where

$$Q = \frac{(2\alpha + \beta + 3\lambda_1\beta/4 + \lambda_2\beta/2)}{(4\alpha + 2\sqrt{2}Cd/3\sqrt{3} + \beta + \frac{1}{4}\lambda_1^2\beta + \frac{1}{2}\lambda_2^2\beta)}. \quad (28)$$

2. Model D2

A comparison between Eq. (26) and the full perturbation theory, Eq. (16), shows two major differences. First, all the chemical terms are absent in Eq. (26). Secondly, the terms

$$\Delta E = \left[\frac{1}{2} \alpha_I (\delta - \delta_0)^2 + \frac{1}{4} \beta_I (\delta - \delta_0)^2 + \frac{1}{2} \alpha \delta^2 + \frac{19}{8} \beta \delta^2 \right] d^2 \quad (22)$$

and

$$\delta = \delta_0 / [1 + (\alpha + 19\beta/4) / (3\alpha_I + \frac{1}{2}\beta_I)]. \quad (23)$$

This expression will be used to study the effect of truncation.

C. Model C: Simple spring model

If all the β 's in Eqs. (22) and (23) are set equal to zero, we have the simple spring model with

$$\Delta E = \left[\frac{1}{2} \alpha_I (\delta - \delta_0)^2 + \frac{1}{2} \alpha \delta^2 \right] d^2 \quad (24)$$

and

$$\delta = \delta_0 / (1 + \frac{1}{3} \alpha / \alpha_I). \quad (25)$$

The spring model recently discussed by Shih *et al.*⁸ corresponds to Eq. (25) with $\alpha = \alpha_I$, so $\delta/\delta_0 = \frac{3}{4}$.

D. Model D: VFF with the continuum connected to the second-shell atoms

1. Model D1

In this case, ΔE only contains the first five contributions listed for case A plus the elastic energy in the continuum. However, the β terms between the second- and third-shell bonds are modified because atoms outside R in the continuum now have radial displacements proportional to the inverse of the square of the radius. The result is

$$\frac{1}{2} \beta_I (\delta - \delta_0)^2 d^2 + \frac{1}{4} \beta \delta^2 d^2$$

in Eq. (16) become

$$\frac{1}{4} \beta_I (\delta - \delta_0)^2 d^2 + \frac{1}{2} \beta \delta^2 d^2$$

in Eq. (26). This difference in the strain energy will mask the true effects of chemical forces if δ from Eq. (26) is compared with FPT. A better way to study the chemical effects is to use the following equation.

$$\Delta E = \left[\frac{1}{2} \alpha_I (\delta - \delta_0)^2 + \frac{1}{2} \beta_I (\delta - \delta_0)^2 + \frac{1}{2} \alpha (\delta + 2\gamma)^2 + \frac{1}{2} \beta (\delta + \gamma)^2 + \frac{1}{4} \beta \delta^2 + \frac{1}{4} \beta (3\delta + \lambda_1 \gamma)^2 + \frac{1}{4} \beta (\delta + \lambda_2 \gamma)^2 \right] d^2 + \frac{\sqrt{2}}{3\sqrt{3}} C \gamma^2 d^3, \quad (29)$$

which is Eq. (16) with all the chemical terms neglected. The corresponding δ becomes

$$\delta = \delta_0 / \left\{ 1 + [\alpha(1 - 2Q) + \frac{1}{4} \beta - \beta(1 + \frac{1}{4} \lambda_1 + \frac{1}{4} \lambda_2)Q] / (3\alpha_I + \beta_I) \right\}, \quad (30)$$

with Q still given by Eq. (28).

E. Model E: Continuum connected to the first-shell atoms

In this case, $\gamma = -3\sqrt{3}\delta/(8\sqrt{2})$ and ΔE only includes the first three contributions listed in model A plus the strain energy of the continuum:

$$\Delta E = \left[\frac{1}{2} \alpha_I (\delta - \delta_0)^2 + \frac{1}{4} \beta_I (\delta - \delta_0)^2 + \frac{1}{2} \beta \left[1 - \frac{3\sqrt{3}}{8\sqrt{2}} \right]^2 \gamma^2 + \frac{1}{4} C d \delta^2 \right] d^2. \quad (31)$$

The relaxation parameter is given by

$$\delta = \delta_0 / \left\{ 1 + \left[\frac{1}{2} C d + \left[1 - \frac{3\sqrt{3}}{8\sqrt{2}} \right]^2 \beta \right] / (3\alpha_I + \frac{1}{2} \beta_I) \right\}. \quad (32)$$

We note that the continuum model used to estimate the bond-length relaxation by Baldereschi and Hopfield⁹ corresponds to Eq. (32) without the β terms, which yields $\delta/\delta_0 \approx 0.4$ to 0.5 , rather than the proper values around 0.7 to 0.8 .

V. ALLOY MIXING ENTHALPY

The impurity-substitution excess energies ΔE provide a first estimate of the mixing enthalpies of pseudobinary alloys. Most current thermodynamics theories of semiconductor alloys are based on an extension of the binary solution model.¹² In this model, the mixing Helmholtz energy of an $A_x B_{1-x} C$ alloy is defined as

$$\Delta F_m = F_{\text{alloy}} - (xF_{AC} + yF_{BC}), \quad (33)$$

where $y = 1 - x$, and F_{AC} and F_{BC} are the respective free energies of the pure AC and BC compounds at the same temperature. Because the C atoms occupy a sublattice, the nearest neighbors of A and B atoms in the alloy are the C atoms. Thus, the pair potentials that enter the binary solution theory are now the second-neighbor interactions. Let N_{AA} , N_{AB} , and N_{BB} be, respectively, the numbers of the second-neighbor AA , AB , and BB pairs, with corresponding pair interaction energies ϵ_{AA} , ϵ_{AB} , and ϵ_{BB} . For tetrahedral semiconductors, there are a total of $6N$ second-neighbor pairs for a crystal containing N unit cells. Denote the ratios N_{AA} , N_{AB} , and N_{BB} to $6N$ as r_{AA} , $r_{AB} = r$, and r_{BB} , respectively. Then those ratios are related to the alloy composition by $r_{AA} = x - r/2$ and $r_{BB} = y - r/2$. The mixing free energy has two terms,

$$\Delta F_m = \Delta E_m - T \Delta S, \quad (34)$$

where the mixing energy is given by

$$\begin{aligned} \Delta E_m &= E_{\text{alloy}} - (xE_{AC} + yE_{BC}) \\ &= 6N(\epsilon_{AA}r_{AA} + \epsilon_{AB}r_{AB} + \epsilon_{BB}r_{BB}) - 6N(x\epsilon_{AA} + y\epsilon_{BB}) \\ &= 6Nr \Delta \epsilon, \end{aligned} \quad (35)$$

where

$$\Delta \epsilon = \epsilon_{AB} - \frac{1}{2}(\epsilon_{AA} + \epsilon_{BB}). \quad (36)$$

The mixing entropy ΔS can also be written from a simple generalization of the random distribution.¹² For modest pressure, ΔE is the same as the mixing enthalpy ΔH_m .

Now the pair interaction energies can be approximately related to the impurity-substitution energies by

$$\Delta_s(A \text{ in } BC) \approx 12(\epsilon_{AB} - \epsilon_{BB}) \quad (37)$$

and

$$\Delta_s(A \text{ in } BC) \approx 12(\epsilon_{AB} - \epsilon_{AA}). \quad (38)$$

Thus, $\Delta \epsilon$ of Eq. (36) becomes

$$\begin{aligned} \Delta \epsilon &= \frac{1}{24} [\Delta_s(A \text{ in } BC) + \Delta_s(B \text{ in } AC)] \\ &= \frac{1}{6} [\Delta E(A \text{ in } BC) + \Delta E(B \text{ in } AC)]. \end{aligned} \quad (39)$$

Usually, the experimental ΔH_m is written as

$$\Delta H_m = x(1-x)\Omega, \quad (40)$$

which is equivalent to assuming a random distribution, i.e., $r = 2x(1-x)$. Using this expression for r and comparing Eqs. (40) and (35), we see that the mixing enthalpy parameter Ω is given by

$$\Omega = 2[\Delta E(A \text{ in } BC) + \Delta E(B \text{ in } AC)]. \quad (41)$$

This connection provides a further check of the theory.

VI. NUMERICAL RESULTS AND DISCUSSION

A. Chemical terms

Table II lists $\delta_0 = 1 - d_I/d$, $\delta = 1 - d_1/d$, the excess energy (per bond) ΔE for the full theory and its corresponding VFF model D2, and the terms derived from the metallization energies, δ_0 [Eq. (19)], F_{ch} , H , ΔE_p , and ΔE_{ch} [Eq. (17)]. The appropriate derivatives f , g , h , ... [see Eq. (9)] are computed using the atomic-term values that we have generated from impurity-level¹³ and structural studies.

For substitutions involving the cation pair (Ga,Al), F_{ch} has the same sign as δ_0 , which means that F_{ch} prevents relaxation and thus tends to increase the strain energy. The chemical forces H are also significant. As a result,

TABLE II. Comparison between the full theory and the corresponding VFF model D2 to study the effects of chemical terms. All ΔE 's are in units of kcal/mole band.

Impurity	Host	Model D2			Full theory						
		δ_0	δ	ΔE	δ'_0	δ	F_{ch} ($10^{-10}N$)	H (N/m)	ΔE_f	ΔE_{ch}	ΔE
Ga	AlP	0.003	0.002	0.001	-0.001	0.001	0.150	4.581	-0.016	-0.016	-0.013
Al	GaP	-0.003	-0.002	0.001	0.001	-0.001	-0.150	4.581	-0.016	-0.016	-0.013
Ga	AlAs	0.001	0.001	0.000	-0.002	-0.001	0.243	5.733	-0.020	-0.021	-0.018
Al	GaAs	-0.001	-0.001	0.000	0.002	0.001	-0.243	5.733	-0.020	-0.021	-0.018
Ga	AlSb	0.006	0.004	0.005	-0.004	0.001	0.389	5.632	-0.054	-0.053	-0.039
Al	GaSb	-0.006	-0.004	0.005	0.004	-0.001	-0.389	5.632	-0.054	-0.053	-0.039
In	GaP	-0.077	-0.052	0.959	-0.006	-0.054	0.699	3.778	-0.188	-0.219	0.742
Ga	InP	0.071	0.056	0.734	0.005	0.057	-0.699	3.778	-0.188	-0.206	0.530
In	GaAs	-0.071	-0.048	0.752	-0.009	-0.050	0.804	4.778	-0.257	-0.283	0.472
Ga	InAs	0.066	0.052	0.592	0.007	0.054	-0.804	4.778	-0.257	-0.265	0.330
In	GaSb	-0.062	-0.043	0.554	-0.004	-0.042	0.352	5.201	-0.363	-0.308	0.247
Ga	InSb	0.059	0.046	0.445	0.004	0.044	-0.352	5.201	-0.363	-0.287	0.160
In	AlP	-0.074	-0.053	0.761	-0.007	-0.056	0.769	3.506	-0.035	-0.087	0.679
Al	InP	0.068	0.053	0.674	0.006	0.056	-0.769	3.506	-0.035	-0.083	0.596
In	AlAs	-0.070	-0.048	0.705	-0.010	-0.051	0.942	4.437	-0.048	-0.111	0.602
Al	InAs	0.065	0.052	0.576	0.008	0.054	-0.942	4.437	-0.048	-0.099	0.485
In	AlSb	-0.056	-0.039	0.440	-0.008	-0.041	0.689	4.979	-0.061	-0.073	0.369
Al	InSb	0.053	0.042	0.368	0.007	0.044	-0.689	4.979	-0.061	-0.061	0.310
Cd	ZnTe	-0.064	-0.048	0.432	-0.003	-0.050	0.202	-0.484	-0.005	-0.064	0.373
Zn	CdTe	0.060	0.050	0.314	0.002	-0.053	-0.202	-0.484	-0.005	-0.072	0.247
Hg	CdTe	0.003	0.002	0.001	0.004	0.005	-0.278	-0.753	-0.018	-0.026	-0.018
Cd	HgTe	-0.003	-0.002	0.001	-0.004	-0.005	0.278	-0.753	-0.018	-0.026	-0.018
Hg	ZnTe	-0.061	-0.045	0.392	-0.001	0.046	0.075	0.002	0.052	0.037	0.429
Zn	HgTe	0.058	0.048	0.286	0.001	0.049	-0.075	0.002	0.052	0.035	0.322
As	AlP	-0.035	-0.026	0.179	0.001	-0.025	-0.085	0.717	-0.005	0.008	0.187
P	AlAs	0.034	0.025	0.185	-0.001	0.025	0.085	0.717	-0.005	0.008	0.194
As	GaP	-0.037	-0.025	0.226	0.002	-0.024	-0.181	1.078	-0.011	0.012	0.240
P	GaAs	0.036	0.027	0.211	-0.001	0.025	0.181	1.078	-0.011	0.014	0.228
As	InP	-0.032	-0.023	0.136	0.001	-0.022	-0.057	0.919	-0.003	0.008	0.144
P	InAs	0.031	0.024	0.128	-0.001	0.024	0.057	0.919	-0.003	0.009	0.138
Sb	AlAs	-0.084	-0.058	1.024	0.008	-0.051	-0.815	0.644	-0.180	0.002	1.060
As	AlSb	0.077	0.059	0.919	-0.007	0.053	0.815	0.644	-0.180	0.027	0.984
Sb	GaAs	-0.078	-0.052	0.908	0.018	-0.040	-1.599	0.927	-0.363	0.106	0.929
As	GaSb	0.073	0.055	0.823	-0.014	0.044	1.599	0.927	-0.363	0.061	0.904
Sb	InAs	-0.070	-0.051	0.603	0.010	-0.042	-0.824	0.855	0.171	0.009	0.645
As	InSb	0.065	0.051	0.551	-0.009	0.044	0.824	0.855	-0.171	0.008	0.613
Sb	AlP	-0.122	-0.085	2.007	0.010	-0.077	-0.944	0.645	0.241	0.074	2.127
P	AlSb	0.109	0.085	1.855	-0.008	0.078	0.944	0.645	-0.241	0.123	2.030
Sb	GaP	-0.119	-0.075	2.132	0.021	-0.061	-1.868	0.930	-0.505	-0.046	2.244
P	GaSb	0.106	0.083	1.806	-0.015	0.070	1.868	0.930	0.505	0.093	2.084
Sb	InP	0.104	0.072	1.383	0.011	-0.063	0.922	0.854	0.214	0.059	1.501
P	InSb	0.094	0.077	1.191	-0.008	0.069	0.922	0.854	0.214	0.123	1.379
Se	ZnS	-0.048	-0.036	0.231	-0.001	-0.036	0.077	0.645	0.003	0.000	0.231
S	ZnSe	0.046	0.037	0.221	0.001	0.037	-0.077	0.645	0.003	0.001	0.222
Te	ZnSe	-0.075	-0.056	0.550	0.000	-0.056	0.028	0.635	0.008	0.024	0.574
Se	ZnTe	0.069	0.054	0.532	0.000	0.054	-0.028	0.635	0.008	0.025	0.557
Te	ZnS	-0.126	-0.092	1.565	-0.001	-0.092	0.101	0.644	0.022	0.041	1.606
S	ZnTe	0.112	0.091	1.446	0.001	0.091	-0.101	0.644	0.022	0.051	1.496

all six cases involving this pair have nearly equal d_1 and d_2 , i.e., the small bond-length differences are made even smaller in the alloy. The excess energies all become negative, mainly because ΔE_p is negative. For the systems involving the (Ga,In) and (In,Al) pairs, F_{ch} has the opposite sign from δ_0 , so δ'_0 and δ_0 have the same sign. The chemical force favors bond distortion. However, because H is positive and introduces an increase in the denominator of Eq. (18), most of the effect of δ'_0 is cancelled. For cases involving (Ga,In), the polarity contributions ΔE_p are all negative. The $F_{ch} \Delta d$ term is negative, but $H(\Delta d)^2$ is positive, so they cancel to a certain degree and leave ΔE lowered primarily because of ΔE_p . While ΔE_p is still negative for the (In,Al) substitutions, its magnitude is reduced considerably. The other chemical energies $F_{ch} \Delta d + H(\Delta d)^2$ can be as large as ΔE_p , but the overall reductions of ΔE are only a fraction of those for the (Ga,In) cases. For the several II-VI systems studied, both F_{ch} and H are small and the net changes in δ have the same sign as δ_0 . However, because δ_0 is small in the (Cd,Hg) substitutions, F_{ch} actually causes a reversal in which the short bond length becomes shorter and the longer one becomes longer. This is the only exceptional case of this type found for all the systems studied. The change of ΔE due to chemical terms in the (Hg,Zn) substitution is also peculiar—it increases mainly because ΔE_p is positive.

Next, we examine the anion substitutions. For the groups involving the (P,As) pair, the chemical shifts are all small, but the trend is less toward relaxation and larger ΔE . The groups involving (As,Sb) and (P,Sb) pairs behave very similarly: F_{ch} are significant and are opposing relaxations, i.e., δ'_0 and δ_0 have opposite signs. At the same time, the H values are several times smaller than those for the corresponding III-V cation substitution case. Thus, most of δ'_0 translates into a real reduction of the ratio δ/δ_0 and consequently introduces extra strain energy. Although the ΔE_p energies are significant and negative, $F_{ch} \Delta d$ are positive and the net ΔE_{ch} can be either positive or negative. However, the induced-strain energy due to reduction of the δ/δ_0 makes all ΔE positive for these two groups of systems. For II-VI systems, all the chemical effects again are small, but the net chemical changes on ΔE are slightly positive.

The above discussion can be summarized in Fig. 2, where the excess energies ΔE calculated from the full perturbation theory and Model D2 are plotted normalized to the results of the simple spring model of Shih, Spicer, Harrison, and Sher (SSHS) (Ref. 8), i.e., Eq. (24) with $\alpha_I = \alpha$, so $\Delta E / (\frac{1}{8} \alpha d^2) = \delta_0^2$. The calculated ΔE rises faster for $\delta_0 \geq 0$ than for $\delta_0 \leq 0$, mainly because $\alpha/\alpha_I = 1$. In fact, if the relation^{7,10} $\alpha/\alpha_I = (d_1/d)^S$ with S of order of 3 to 5 is used in Eq. (24), we obtain a percentage correction of $S\delta_0/4$ to the SSHS results, which explains the skewed behavior of the curve. It is also clear that ΔE rises faster than δ_0^2 for larger δ_0 . However, the zeroth-order theory of SSHS is clearly an excellent representation of the global features of ΔE . The results from model D2 are closer to the parabolic form than those from FPT. The figure clearly shows the general trends; the chemical terms cause negative shifts in ΔE for cation substitutions

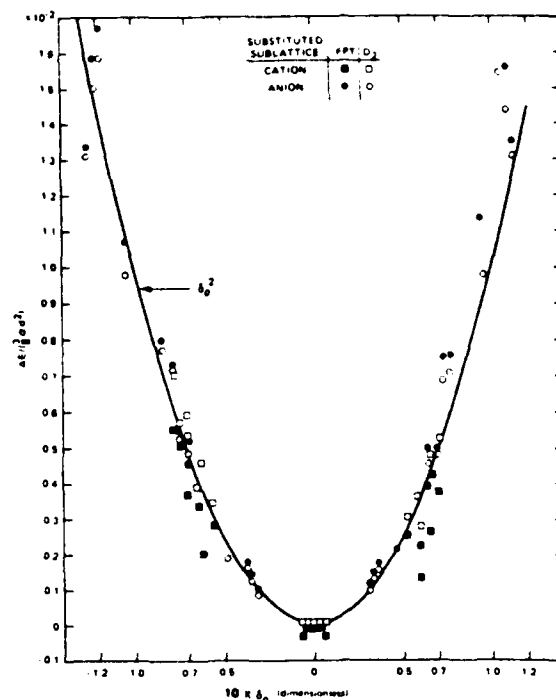


FIG. 2. The excess energies ΔE over $\frac{1}{8}\alpha d^2$ calculated from the full perturbation theory (FPT) and its corresponding valence-force-field model D2. The solid curve corresponds to Eq. (24) with $\alpha = \alpha_I$.

and positive shifts for anion impurities. It is also clear that the chemical shifts can be very large. These effects will have important consequences on the alloy mixing enthalpies to be discussed later.

B. Impurity bond length

Table III lists the impurity bond lengths d_1 calculated from different models, while a comparison of theory and the available experimental data^{1,14,15} is presented in Table IV. The actual size of changes in d_1 induced by the chemical terms can be seen by comparing model D2 with the full theory. Except for the systems involving the substitution of (Ga,As) and (P,Sb) pairs (where changes range from 0.01 to 0.03 Å), all the chemically induced changes are less than 0.01 Å. Comparison among models A, B, and C shows that, while extending the boundary helps the relaxation (compare model B to A), i.e., δ/δ_0 is closer to 1, the inclusion of the bond-bending forces (the β terms) (compare model B with C) prevents it. The simple spring model (model C), which contains neither of these terms, evidently represents a delicate cancellation of these effects and predicts results close to those of the full perturbation theory and experiment. Although the d_1 values of model C are often very close to those of model A, there are cases [e.g., Ga(P,Sb)] in which model C can differ from model

TABLE III. Calculated impurity local bond lengths (in Å) from the full theory and several valence force models discussed in Sec. III, and their comparison with the values calculated by Martins and Zunger (Ref. 3).

Impurity	Host	A	B	C	D1	D2	E	FPT	MZ
Ga	AlP	2.362	2.363	2.362	2.362	2.362	2.364	2.364	
Al	GaP	2.365	2.364	2.365	2.365	2.365	2.365	2.363	
Ga	AlAs	2.449	2.449	2.449	2.449	2.449	2.450	2.452	
Al	GaAs	2.450	2.450	2.450	2.450	2.450	2.450	2.447	
Ga	AlSb	2.645	2.646	2.644	2.645	2.644	2.649	2.653	
Al	GaSb	2.651	2.650	2.652	2.652	2.652	2.650	2.644	
In	GaP	2.477	2.462	2.492	2.479	2.483	2.435	2.487	2.474
Ga	InP	2.406	2.421	2.402	2.395	2.399	2.409	2.396	2.409
In	GaAs	2.559	2.544	2.573	2.561	2.565	2.518	2.570	2.556
Ga	InAs	2.492	2.506	2.486	2.482	2.485	2.496	2.481	2.495
In	GaSb	2.747	2.734	2.760	2.749	2.754	2.710	2.750	2.739
Ga	InSb	2.683	2.697	2.678	2.673	2.676	2.686	2.680	2.683
In	AlP	2.487	2.472	2.494	2.490	2.493	2.447	2.498	2.480
Al	InP	2.412	2.427	2.408	2.401	2.405	2.415	2.400	2.414
In	AlAs	2.561	2.546	2.572	2.563	2.568	2.523	2.575	2.553
Al	InAs	2.493	2.506	2.487	2.483	2.487	2.497	2.480	2.495
In	AlSb	2.754	2.741	2.763	2.756	2.760	2.721	2.765	2.746
Al	InSb	2.693	2.705	2.689	2.685	2.687	2.696	2.683	2.693
Cd	ZnTe	2.756	2.740	2.760	2.760	2.763	2.720	2.770	2.755
Zn	CdTe	2.673	2.688	2.676	2.660	2.665	2.671	2.658	2.674
Hg	CdTe	2.800	2.801	2.800	2.800	2.799	2.801	2.790	
Cd	HgTe	2.804	2.803	2.804	2.805	2.805	2.804	2.813	
Hg	ZnTe	2.750	2.735	2.754	2.753	2.757	2.715	2.758	2.748
Zn	HgTe	2.671	2.685	2.674	2.659	2.664	2.671	2.662	2.673
As	AlP	2.425	2.418	2.429	2.427	2.428	2.406	2.427	2.422
P	AlAs	2.392	2.399	2.387	2.387	2.389	1.394	2.390	2.395
As	GaP	2.417	2.409	2.424	2.417	2.420	2.396	2.416	2.414
P	GaAs	2.386	2.393	2.380	2.382	2.383	2.389	2.386	2.387
As	InP	2.596	2.589	2.599	2.598	2.600	2.579	2.598	2.595
P	InAs	2.561	2.568	2.558	2.557	2.558	2.563	2.560	2.562
Sb	AlAs	2.584	2.566	2.597	2.587	2.592	2.539	2.577	2.574
As	AlSb	2.506	2.522	2.496	2.495	2.498	2.511	2.514	2.510
Sb	GaAs	2.569	2.553	2.584	2.571	2.576	2.524	2.546	2.564
As	GaSb	2.501	2.516	2.489	2.492	2.495	2.508	2.525	2.505
Sb	InAs	2.747	2.730	2.754	2.750	2.754	2.705	2.733	2.739
As	InSb	2.669	2.683	2.663	2.658	2.662	2.672	2.683	2.667
Sb	AlP	2.555	2.529	2.569	2.561	2.568	2.488	2.550	2.542
P	AlSb	2.440	2.462	2.426	2.425	2.430	2.447	2.448	2.444
Sb	GaP	2.526	2.503	2.551	2.529	2.537	2.461	2.504	2.519
P	GaSb	2.431	2.451	2.414	2.418	2.422	2.440	2.454	2.436
Sb	InP	2.712	2.687	2.720	2.719	2.725	2.654	2.702	2.700
P	InSb	2.599	2.619	2.591	2.585	2.590	2.604	2.611	2.597
Se	ZnS	2.420	2.409	2.421	2.424	2.426	2.396	2.426	2.420
S	ZnSe	2.367	2.376	2.365	2.360	2.364	2.370	2.363	2.367
Te	ZnSe	2.586	2.569	2.588	2.589	2.592	2.540	2.591	2.584
Se	ZnTe	2.501	2.517	2.497	2.490	2.494	2.504	2.495	2.502
Te	ZnS	2.543	2.513	2.544	2.552	2.558	2.478	2.557	2.539
S	ZnTe	2.406	2.429	2.400	2.390	2.396	2.410	2.396	2.407

TABLE IV. Deviations of the calculated impurity bond lengths (in Å) as compared with the experimental values from EXAFS.

Impurity	Host	A	C	D1	FPT	MZ	SSHS ^a	Expt.
In	GaAs	-0.028	-0.014	-0.025	-0.017	-0.031	-0.009	2.587 ^b
Ga	InAs	0.004	-0.001	-0.005	-0.006	0.008	0.005	2.487 ^b
Cd	ZnTe	0.004	0.008	-0.008	0.018	0.003	0.012	2.75(2) ^c
Zn	CdTe	-0.01 to -0.02	0.0 to -0.01	-0.02 to -0.03	-0.02 to -0.03	-0.01 to -0.02	0.0 to -0.01	2.68 to 2.69 ^c
Te	ZnSe	-0.009	-0.07	-0.003	-0.004	-0.011	-0.004	2.595 ^d
Se	ZnTe	0.005	0.01	-0.006	-0.001	0.006	0.004	2.496 ^d
Mean		0.011	0.006	0.012	0.012	0.012	0.006	
absolute deviation								

^aSSHS, Ref. 8.^bRef. 1.^cQuoted in Ref. 3.^dReference 14.

A by 0.025 Å. Model A produces about the same d_1 values as model D1, where the maximum difference in d_1 is only 0.015 Å. Martins and Zunger³ used the same model as model A; however, their analytic expression for δ is different from that given by Eq. (21). Nevertheless, numerical results indicate that these two calculations agree to 0.01 Å. The slightly different forms of strain energies used in models D2 and D1 only introduce a small change in d_1 , with the largest difference being less than 0.01 Å. The first-shell continuum model (model E) allows too little relaxation, so while the other models produce a ratio δ/δ_0 ranging from 0.6 to 0.8, model E only ranges from 0.4 to 0.6. The reason that the fixed boundary in model A works is that the effective shear coefficient C (see Table I) characterizing the strain energy in the elastic continuum is large. However, model B is too rigid and does not provide enough buffer between the impurity bond and the fixed boundary.

The comparison of the theoretical results with the available experimental data in Table IV indicates that models B and E are the least accurate. Models A, D1, that of Martins and Zunger (MZ), and the full theory are comparable in that all have an average absolute deviation of 0.012 Å, which is about the experimental uncertainty in extended x-ray-absorption fine structure (EXAFS). The agreement between theory and experiment, however, is not uniform. The most surprising result in Table IV is that the simple spring model (model C) and its cruder version used by Shih *et al.*⁸ ($\alpha=\alpha_1$ so $\delta/\delta_0=0.75$, labeled as SSHS) have the smallest variance in d_1 , about 0.006 Å. We know this does not imply that the simple spring model represents the real picture of bond-length relaxation. For example, if we let all the shear coefficients be 0, i.e., $\beta=C=0$ in our model, then as the range of the boundary is gradually extended, the local bond length will eventually relax to the impurity bond length $d_1=d_I$, or $\delta=\delta_0$. This can be seen in model A from Eq. (21), where δ reduces to $\delta_0/(1+\alpha/6\alpha_1)$, rather than $\delta_0/(1+\alpha/3\alpha_1)$ as predicted by model C, and in model D from Eqs. (27) and (30), δ becomes δ_0 , if the continuum is taken to be shearless. Considering that various effects are included that may mask the absolute accuracy of d_1 predictions (e.g., while low-temperature bond lengths are used in the calculation, the room-temperature values of elastic constants are adopted), the agreement of various models with experiments in Table IV should be regarded as excellent. There are, however, many other impurity systems in which the simple-spring-model predictions differ considerably from other models, as is shown in Fig. 3, where δ is plotted against δ_0 for the full theory. Those points that deviate significantly from the 0.75-slope line are the systems with (As,Sb) or (P,Sb) substitutions. Additional EXAFS measurements on these systems are needed to test these predictions.

C. Mixing enthalpies

Table V lists the mixing enthalpy parameters Ω (in kcal/mole) for a number of alloys estimated from Eq. (41) for all the models considered, along with other theoretical^{3,16-18} and experimental values.^{16,19} As already dis-

TABLE V. Mixing enthalpy parameter Ω (in kcal/mole) estimated from the full perturbation theory and several valence force models discussed in Sec. III, and comparison with experiments and other theories.

	A	B	C	D1	D2	E	FPT	MZ ^a	DL ^b	FM ^c	VV ^d	Expt. ^e
(Ga,Al)P	0.00	0.01	0.00	0.01	0.01	0.01	-0.05					
(Ga,Al)As	0.00	0.00	0.00	0.00	0.00	0.00	-0.07	0.02	0.02	0.03	0.11	0.0
(Ga,Al)Sb	0.02	0.03	0.02	0.02	0.02	0.03	-0.15	0.02	0.02	0.03		0.0
(Ga,In)P	3.76	4.79	3.0	3.29	3.39	5.24	2.54	4.56	3.63	2.94		3.25, 3.5
(Ga,In)As	2.97	3.76	2.36	2.61	2.69	4.14	1.60	2.49	2.81	2.42	1.25	1.65, 2.0, 3.0
(Ga,In)Sb	2.22	2.83	1.77	1.95	2.00	3.09	0.81	2.53	1.85	1.83		1.47, 1.9
(In,Al)P	3.24	4.22	2.77	2.78	2.87	4.60	2.55					
(In,Al)As	2.86	3.65	2.32	2.49	2.56	3.93	2.17	3.60	2.81	2.37		2.5
(In,Al)Sb	1.81	2.33	1.49	1.57	1.61	2.50	1.36	2.06	1.46	1.45		0.6
(Cd,Zn)Te	1.80	2.43	1.73	1.43	1.49	2.45	1.24	2.12	1.97	1.63		1.34
(Hg,Cd)Te	0.00	0.00	0.00	0.00	0.00	0.00	-0.07					0.7, 1.4
(Hg,Zn)Te	1.63	2.20	1.56	1.30	1.36	2.23	1.50	1.91	1.81	1.48		3.0
Al(P,As)	0.81	1.03	0.65	0.71	0.73	1.14	0.76					
Ga(P,As)	0.95	1.18	0.70	0.86	0.87	1.32	0.94	1.15	0.98	0.66	0.12	0.4, 1.0
In(P,As)	0.60	0.78	0.52	0.51	0.53	0.84	0.57	0.72	0.58	0.52		0.4
Al(As,Sb)	4.31	5.45	3.38	3.80	3.88	5.92	4.09					
Ga(As,Sb)	3.77	4.69	2.81	3.40	3.46	5.22	3.67	4.58	3.35	2.76		4.0, 4.5
In(As,Sb)	2.61	3.39	2.23	2.24	2.31	3.67	2.52	2.89	2.29	2.17	6.65	2.25, 2.9
Al(P,Sb)	8.60	10.99	6.99	7.54	7.73	12.00	8.32					
Ga(P,Sb)	8.54	10.61	6.36	7.72	7.88	11.66	8.66					
In(P,Sb)	5.87	7.64	5.08	4.99	5.15	8.04	5.76					
Zn(S,Se)	1.04	1.39	0.98	0.85	0.90	1.49	0.90					
Zn(S,Te)	1.04	1.39	0.98	0.85	0.90	1.49	0.90					
Zn(Se,Te)	2.47	3.27	2.23	2.09	2.16	3.63	2.26	2.91	3.11	2.12	3.12	1.55
Zn(S,Te)	7.02	9.34	6.45	5.80	6.02	9.72	6.20					

^aReference 3, column A of Table III.^bReference 16.^cReference 18.^dReference 17.^eReferences 16 and 19.

cussed, the chemical terms reduce the excess energies in the cation impurities and increase them for anion impurities. The corresponding changes in Ω are the differences between the FPT and model D2. We note that the reductions of Ω for the (Ga,In) alloys are very large (>1 kcal/mole) and also significant for (In,Al) alloys. However, the increases in Ω for the anion substitutional alloys are not as large. Also, the Ω differences between models D1 and D2 are less than 10%. Model A produces Ω values about 20% larger than model D1, model B in turn is 20% higher than model A, and model E is 10% higher than model B. The Ω values in the simple spring model (model C) are seen to be about the same as model D1, although the differences among systems can be positive or negative. Although MZ used the same strain model as model A, their Ω values do not agree with our model A values because their way of estimating Ω is different. In

fact, the values of MZ are closer to model B than to A.

To distinguish the quantitative nature of different theoretical models, we note that there are also important factors that may mask the comparison between theory and experiment for Ω . One important factor is that the mixing enthalpies extracted from phase-diagram analysis are sensitive to sample and experimental conditions. These ΔH_m contain contributions from various nonideal structures such as vacancies, impurities, dislocations, grain boundaries, and surface conditions, in addition to the ideal ΔH_m considered here for solid solutions. Thus, our theoretical ΔH_m should represent a lower bound. Another complication comes from the version of the theory of solid solution adopted. The theory used for analysis so far assumes a regular solid solution with second-neighbor pair interactions as was outlined in Sec. V. Recent experimental²⁰⁻²² and theoretical²³ studies

TABLE VI. Comparison of the critical temperature T_c of mixing and melting temperatures of the constituents T_1 and T_2 , in the order of their appearance in the parentheses. Also tabulated are the averaged absolute values of $|\delta_0|$ and the ratio $|\delta_0|/\delta_m$.

System	$ \delta_0 $ (%)	T_c (K)	T_c/T_1	T_c/T_2	$ \delta_0 /\delta_m$
(Al,Ga)Sb	0.6	0	0	0	0.067
(Al,Ga)As	0.1	0	0	0	0.009
(Al,Ga)P	0.3	0	0	0	0.029
(Al,In)Sb	5.5	342	0.25	0.42	0.679
(Ga,In)Sb	5.8	204	0.21	0.25	0.716
(Al,In)As	6.8	547	0.29	0.45	0.687
(Ga,In)As	6.9	403	0.23	0.34	0.697
(Al,In)P	7.1	642	0.36	0.48	0.732
(Ga,In)P	7.4	639	0.43	0.48	0.763
In(P,As)	3.2	144	0.11	0.12	0.330
Ga(P,As)	3.7	236	0.14	0.15	0.352
Ga(P,As)	3.5	191	0.10	0.11	0.307
In(As,Sb)	6.8	635	0.52	0.79	0.840
Ga(As,Sb)	7.6	924	0.53	0.94	0.844
Al(As,Sb)	8.1	1030	0.56	0.78	0.810
In(P,Sb)	9.9	1450	1.08	1.82	1.222
Ga(P,Sb)	11.3	2180	1.25	2.21	1.256
Al(P,Sb)	11.6	2095	1.19	1.58	1.116
(Cd,Hg)Te	0.3	0	0	0	0.033
(Zn,Hg)Te	6.0	377	0.25	0.40	0.659
(Zn,Cd)Te	6.2	312	0.21	0.23	0.564
Zn(S,Se)	4.7	226	0.11	0.13	0.362
Zn(Se,Te)	7.2	569	0.32	0.38	0.615
Zn(S,Te)	11.9	1560	0.74	1.03	1.017

ficient C in Eq. (14) to be composition dependent, which will cause Ω to increase. Despite these uncertainties, useful comparisons across the board in Table V can still be made.

Based on the above considerations, we can conclude that models B, E, and MZ predict Ω values that are too high. We should emphasize that all the Ω numbers for models from A through MZ are directly calculated without any adjustable parameters. The fact that models A, C, and D1,D2, and the FPT agree with the experiment as well as or even slightly better than the one-parameter theories, the delta-lattice (DL) model¹⁶ and the model of Fedder and Muller¹⁸ (FM), is already quite an accomplishment. The few numbers taken from Van Vechten's calculations¹⁷ (VV) indicate that the dielectric model predicts results at larger variance with experiments. There are two important implications about the FPT that can be drawn from Table III. First, the theory predicts a small but negative Ω value for several alloys. This not only means that there is no miscibility gap in these alloys but also implies a tendency toward ordering, in which the substitutional atoms tend to be surrounded by different second-neighbor species. For stoichiometric compositions, this implies a

tendency toward compound formation. Secondly, the FPT tends to predict smaller Ω values than observed experimentally, which should be expected according to our discussion. To the extent that the FPT predicts the correct ΔH_m values for an ideal solution, the difference $\Delta H_m^{\text{expt}} - \Delta H_m$ may be attributed to imperfect conditions and deviations from the ideal solution theory.

Finally, the calculated Ω values in Table V provide some guidance in separating the completely miscible alloys from immiscible ones.^{26,27} In a true random alloy, the criteria²⁸ for alloy mixing at a temperature T is that $T \geq T_c$, where the critical temperature T_c is given by $\Omega/(2R_g)$, with R_g being the universal gas constant.²⁹ For an $A_xB_{1-x}C$ alloy to be miscible throughout the whole concentration range, the requirement is that both the melting temperatures T_1 and T_2 of the pure AC and BC compounds be greater than T_c . Table VI lists the values of T_c associated with the Ω values in the FPT, the ratios T_c/T_1 and T_c/T_2 , and the average absolute values of δ_0 for the alloys considered in Table V. In Table VI, T_c is set equal to zero if Ω is negative and T_2 is chosen to be the lower value of the two melting temperatures, so the criterion for not having a miscibility gap is $T_c/T_2 < 1$.

There is an empirical rule²⁶ stating that this will be satisfied if the lattice mismatch $|\delta_0|$ between the two alloy components is less than 7.5%. However, we find that (see Appendix C) a more precise rule is $|\delta_0| > \delta_m$, where $\delta_m = 1.63\chi_m$ and χ_m is the ratio of the rms bond-length amplitude fluctuation to the bond length at the melting temperature T_2 . The values of T_m for the compounds involved³⁰ and the associate χ_m values estimated from Eqs. (C2) and (C3) are tabulated in Table I. The model used in Appendix C yields $T_c/T_2 = (\delta_0/\delta_m)^2$. This suggests that it is instructive to plot T_c/T_2 as a function of $|\delta_0|/\delta_m$, as is shown in Fig. 4 for the T_c calculated from FPT. This plot is similar to the ΔE versus δ_0 curve in Fig. 2 because, in fact, Ω is proportional to the sum of the ΔE values of the two constituents [see Eq. (41)]. However, if T_c/T_2 is plotted against $|\delta_0|$ alone, the FPT points are much more scattered, and those of SSHS would not even exhibit a smooth simple quadratic form because the lower melting temperature T_2 is not a smooth function of $|\delta_0|$. This result suggests that $|\delta_0|/\delta_m < 1$ is a better criterion than $|\delta_0| < 0.075$. Figure 3 also clearly shows the chemical effects: all the cation-substitution alloy points lie below the solid curve and all the anion-substitution alloys have (T_c/T_2) values on or above the curve, corresponding to negative and positive shifts in ΔE due to the chemical terms. Again, the curve based on the SSHS model is an excellent universal representation. From the figure, we see that all (P,Sb) alloys should have miscibility gaps and all (As,Sb) alloys are predicted to be miscible, although on the borderline, because the actual mixing enthalpies are larger than these ideal calculated values. The figure also shows that Zn(S,Te) has a miscibility gap but a smaller value of T_c/T_2 than the (P,Sb) alloys, despite the fact that its $|\delta_0|$ value is larger. All these predictions are consistent with the available experimental evidence.

VII. SUMMARY AND CONCLUSION

In this paper a simple theory of defect substitution energies is formulated. The substitution energy is compactly separated into a replacement energy Δ_R and a distortion energy of the pure host crystal [see Eq. (2)]. However, a rigorous application of this theory requires an improvement in certain quantitative aspects of Harrison's bonding theory,⁵ particularly the elastic constants.⁶ The most interesting application of this theory presented in this paper is its perturbation form which enables us to absorb the measured elastic coefficients into the calculation and, more importantly, to study the chemical effects. The origin of chemical influences on impurity bond relaxation can be attributed to three mechanisms [see Eq. (17)]: a chemical force F_{ch} that either helps or hinders lattice relaxation, depending on whether it has the same or opposite sign from the bond-length difference $d-d_i$ between the host and impurity, a chemical energy that depends on the difference of the polarities between the impurity and host bonds, ΔV_i , and an effective elastic force constant H that, when positive, also tends to restrain the lattice from distortion. To study the effect of boundaries between the core atoms around an impurity and the rest of the elastic medium, various models based on the valence force field¹⁰

are derived and their results are compared with the full perturbation theory and available experimental data. We found at least five models, including the FPT, that produce the correct impurity bond lengths with variances for the compounds studied about equal to the experimental uncertainties in EXAFS^{1,4,14} (~ 0.01 Å). However, some models are oversimplified and will certainly not predict other properties equally well. However, more experimental lattice constant measurements to further test the theory, particularly on (As,Sb) and (P,Sb) substitution systems for which there are larger differences between different models, are needed. It would also be instructive to see if the predicted reversal for (Hg,Cd)Te is found.

The excess energies of impurity substitution are also shown to provide good estimates of the mixing enthalpies Ω of pseudobinary alloys. The chemical shifts are found to have a negative net contribution to Ω for most cation substitutions, but positive contributions for anion substitutions. The chemical reduction of Ω in (Ga,In) alloys is larger than 1 kcal/mole (30–100%). Several VFF models and the full perturbation theory produce results for Ω that are as good as the best theories with one adjustable parameter. However, the full theory tends to yield answers on the low side of the experimental values, which we argue is as it should be because there are nonideal structures that also contribute to Ω . The calculated Ω values and the melting temperatures are used to predict the existence of alloy miscibility gaps, and the results correlate well with experiments.

Finally, we wish to comment on the accuracy of the theories that are connected to the present model. The perturbation theory has already been stretched beyond its expected region of validity and predicts d_i to within experimental uncertainties (~ 0.01 Å) even for cases with large bond-length differences ($\delta_i > 0.1$). The accuracy can only be improved if the full nonperturbation theory outlined in Sec. II is used. This calculation is needed for the strong substitution cases that were not considered in this paper: examples are B,Ga, B,In, N,P, N,As, N,Sb, O,S, O,Se, and O,Te substitutions. Although we believe that for the properties treated, the model with a continuum attached to the second shell is as accurate as the perturbation theory used, it remains to be seen if this is true for other properties, especially strain coefficients. Finally, the present theory has been extended to study alloys^{5,6} by embedding clusters in an effective medium. This enables us to study the bond length and energy variations throughout the whole concentration range. However, a quantitative calculation still awaits an improvement of the accuracy of Harrison's theory. A similar procedure is also being extended to a study of the alloy electronic structure for which a cluster CPA (coherent-potential approximation) involving both potential and structural disorder³¹ will be used.

ACKNOWLEDGMENTS

This work benefited from useful discussions with Professor W. A. Harrison and Professor A. Zunger. One of us (A.-B. C.) would like to thank Professor W. E. Spicer for his hospitality. The work is supported in part by U.S.

Air Force Office of Scientific Research Contract No. AFOSR-84-0284 and U.S. Defense Advanced Projects Agency DARPA Contract No. MDA-903-83-C-0108.

APPENDIX A: ELASTIC ENERGY IN CONTINUUM

In Sec. III the elastic energy outside a sphere of radius R centered at the impurity is assumed to be a continuum with a radial displacement $u \propto \hat{r}/r^2$. If the displacement at R is u_0 , then $u(r) = u_0(R^2/r^2)\hat{r}$. The energy density in the continuum is given by

$$\begin{aligned} \delta E(r) = & \frac{1}{2} C_{11}(e_{xx}^2 + e_{yy}^2 + e_{zz}^2) \\ & + C_{12}(e_{yy}e_{zz} + e_{xx}e_{yy} + e_{xx}e_{zz}) \\ & + \frac{1}{2} C_{44}(e_{xy}^2 + e_{yz}^2 + e_{zx}^2), \end{aligned}$$

where

$$\begin{aligned} e_{xx} &= \frac{\partial u_x}{\partial x} = R^2 u_0 (r^2 - 3x^2)/r^5, \\ e_{xy} &= \frac{\partial u_x}{\partial y} + \frac{\partial u_y}{\partial x} = -6R^2 u_0 xy/r^5, \dots \end{aligned}$$

Thus, the total elastic energy in the continuum is

$$\begin{aligned} \Delta_{dis}^{(out)} &= \int_R^\infty \delta E(r) d^3r \\ &= 4\pi R u_0^2 \left(\frac{1}{3} C_{11} - \frac{2}{3} C_{12} + \frac{5}{3} C_{44} \right) \\ &= C R u_0^2, \end{aligned}$$

where the effective shear coefficient is given by

$$C = \pi(1.6C_{11} - 1.6C_{12} + 4.8C_{44}).$$

APPENDIX B: DISTORTION ENERGY

In this Appendix we count the detailed contributions of the bond-stretching terms $\Delta(r_i, r_j)$ and "bond-bending" terms $\Delta(r_i, r_j)$ for $i \neq j$ in VFF [Eq. (13)] that enter Eq. (16) in FPT and in the VFF models in Sec. III.

1. α and β terms from the first-shell bonds

The four bond vectors pointing away from the central impurity according to Fig. 1 are

$$\begin{aligned} \mathbf{r}_1 &= (1 - \delta, 1 - \delta, 1 - \delta)d/\sqrt{3}, \\ \mathbf{r}_2 &= (1 - \delta, -1 - \delta, -1 - \delta)d/\sqrt{3}, \dots \end{aligned}$$

Thus, $\Delta(r_1, r_1) = 2\delta d^2$ and $\Delta(r_1, r_2) = \frac{1}{3}\delta d^2$. The α terms contribute

$$4 \times 3\alpha_1 \left(\frac{1}{3}\delta d^2 \right)^2 / 8d^2 = 6\alpha_1 \delta^2 d^2,$$

and the β terms contribute

$$6 \times 3\beta_1 \left(\frac{1}{3}\delta d^2 \right)^2 / 8d^2 = \beta_1 \delta^2 d^2.$$

If an A atom is replaced by a B atom, as was done in FPT, the α_1 and β_1 are replaced by α and β , respectively.

2. α terms from the second-shell bonds, β terms between the first- and second-shell bonds and among the second-shell bonds

For these terms we need to consider the four bond vectors pointing away from C . They are

$$\begin{aligned} \mathbf{r}_1 &= (-1 + \delta, -1 + \delta, -1 + \delta)d/\sqrt{3}, \\ \mathbf{r}_2 &= (-1 + \delta, 1 + \delta + \gamma, 1 + \delta + \gamma)d/\sqrt{3}, \\ \mathbf{r}_3 &= (1 + \delta + \gamma, -1 + \delta, 1 + \delta + \gamma)d/\sqrt{3}, \dots \end{aligned}$$

Then $\Delta(r_2, r_2) = \frac{2}{3}(\delta + 2\gamma)d^2$, $\Delta(r_1, r_2) = -\frac{2}{3}(\delta + \gamma)d^2$, and $\Delta(r_2, r_3) = \frac{2}{3}\delta d^2$. Thus, the α terms from the second-shell bonds become

$$4 \times 3 \times 3\alpha \left[\frac{2}{3}(\delta + 2\gamma)d^2 \right]^2 / 8d^2 = 2\alpha(\delta + 2\delta)^2 d^2,$$

the β term between the first- and second-shell bonds are

$$4 \times 3 \times 3\beta \left[\frac{2}{3}(\delta + \gamma)d^2 \right]^2 / 8d^2 = 2(\gamma + \delta)^2 \beta d^2,$$

and the β terms among the second-shell bonds are

$$4 \times 3 \times 3\beta \left(\frac{2}{3}\delta d^2 \right)^2 / 8d^2 = 2\delta^2 \beta d^2.$$

3. α terms for the third-shell bonds, β terms between the second- and third-shell bonds and among the third-shell bonds adjacent to the second-shell atoms

For these terms we need to consider the bond vectors pointing away from B in Fig. 1. They are

$$\begin{aligned} \mathbf{r}_2 &= (1 - \delta, -1 - \gamma - \delta, -1 - \gamma - \delta)d/\sqrt{3}, \\ \mathbf{r}_1 &= (1 + \gamma', 1 + 3\gamma' - \gamma, 1 + 3\gamma' - \gamma)d/\sqrt{3}, \\ \mathbf{r}_3 &= (-1 - \gamma'', 1 + 3\gamma'' - \gamma, -1 + \gamma'' - \gamma)d/\sqrt{3}, \end{aligned}$$

and

$$\mathbf{r}_4 = (-1 - \gamma'', -1 + \gamma'' - \gamma, 1 + 3\gamma'' - \gamma)d/\sqrt{3}.$$

Thus, we have

$$\Delta(r_1, r_2) = -\frac{d^2}{3}(3\delta + 5\gamma'),$$

$$\Delta(r_2, r_3) = \frac{d^2}{3}(\delta + 2\gamma - 5\gamma''),$$

$$\Delta(r_3, r_4) = \frac{d^2}{3}d^2\gamma'',$$

$$\Delta(r_1, r_3) = \frac{d^2}{3}(-2\gamma - \gamma' + 3\gamma''),$$

$$\Delta(r_3, r_4) = \frac{d^2}{3}(6\gamma''),$$

and

$$\Delta(r_1, r_1) = \frac{d^2}{3}(14\gamma' + 4\gamma).$$

For model A, $\gamma' = \gamma'' = 0$, so the α terms of the third-shell bonds become

$$4 \times 3 \times 3\alpha [2 \times \Delta(r_3, r_3)^2 + \Delta(r_1, r_1)^2] / 8d^2 = 8\alpha\gamma^2 d^2.$$

the β terms between the second- and third-shell bonds are

$$4 \times 3 \times 3\beta[(\Delta \mathbf{r}_1 \cdot \mathbf{r}_2)^2 + 2(\Delta \mathbf{r}_2 \cdot \mathbf{r}_3)^2]/8d^2 \\ = \frac{9}{2}\beta d^2[\delta^2 + \frac{2}{9}(\delta + 2\gamma)^2] = \frac{9}{2}\beta\delta^2 d^2 + \beta(\delta + 2\gamma)^2 d^2,$$

and the β terms among the third-shell bonds adjacent to the second-shell atoms are

$$4 \times 3 \times 3\beta[2(\Delta \mathbf{r}_1 \cdot \mathbf{r}_3)^2/(8d^2) + (\Delta \mathbf{r}_3 \cdot \mathbf{r}_4)^2] = 4\beta\gamma^2 d^2.$$

For continuum and the only contribution from this group are the β terms between the second- and third-shell bonds. Since the displacements in the continuum are proportional to $1/R^2$, $\gamma' = 8\sqrt{2}\gamma/(19\sqrt{19})$ and $\gamma'' = 8\sqrt{2}\gamma/(11\sqrt{11})$. Thus, these β terms become

$$\frac{9}{2d^2}\beta \left[\frac{d^4}{9}(3\delta + 5\gamma')^2 + \frac{2d^4}{9}(\delta + 2\gamma - 5\gamma'')^2 \right] \\ = \frac{1}{2}\beta \left[\left[3\delta + \frac{40\sqrt{2}}{19\sqrt{19}}\gamma \right]^2 \right. \\ \left. + 2 \left[\delta + 2\gamma - \frac{40\sqrt{2}}{11\sqrt{11}}\gamma \right]^2 \right] d^2.$$

4. β terms for bonds adjacent to the third-shell atoms

These terms only enter model A, so $r' = r'' = 0$. There are two different groups, one like those adjacent to C' and another like those meeting at C'' . The four bond vectors pointing away from C' are

$$\mathbf{r}_1 = (-1, -1 + \gamma, -1 + \gamma)d/\sqrt{3},$$

$$\mathbf{r}_2 = (-1, 1, 1)d/\sqrt{3},$$

$$\mathbf{r}_3 = (1, -1, 1)d/\sqrt{3},$$

and

$$\mathbf{r}_4 = (1, 1, -1)d/\sqrt{3}.$$

Thus, the only contribution from this group is

$$4 \times 3 \times 3\beta[(\Delta \mathbf{r} \cdot \mathbf{r}_i)^2]/8d^2 = 2\beta\gamma^2 d^2.$$

The four bond vectors around C'' are

$$\mathbf{r}_1 = (-1 + \gamma, -1 - \gamma, -1)d/\sqrt{3},$$

$$\mathbf{r}_2 = (-1, 1, 1)d/\sqrt{3},$$

$$\mathbf{r}_3 = (1, -1 + \gamma, 1 + \gamma)d/\sqrt{3},$$

and

$$\mathbf{r}_4 = (1, 1, -1)d/\sqrt{3},$$

which only results in the first-order term $\Delta(\mathbf{r}_2 \cdot \mathbf{r}_3) = \frac{2}{3}\gamma d^2$. Thus, the group contributes to

$$4 \times 3 \times 3\beta[2(\Delta \mathbf{r}_2 \cdot \mathbf{r}_3)^2]/8d^2 = 4\beta\gamma^2 d^2,$$

and the combined contribution from these two groups is $6\beta\gamma^2 d^2$.

APPENDIX C: CRITERION OF MISCIBILITY

Starting with Eq. (24) and using the SSHS model $\alpha = \alpha_I$, one finds the mixing enthalpy parameter Ω to be

$$\Omega = \frac{3}{2}\bar{\alpha}(d_{AC} - d_{BC})^2 N_0, \quad (C1)$$

where N_0 is Avogadro's number and $\bar{\alpha} = \frac{1}{2}(\alpha_{AC} + \alpha_{BC})$. Then relate the mean-square bond-length fluctuation $\langle \xi^2 \rangle$ at the melting temperature T_m to T_m for a compound by equating the average potential energy per unit cell to half of the thermal energy:

$$\langle V_{\text{pot}} \rangle \simeq 4 \times \frac{1}{2} \alpha \langle \xi^2 \rangle = \frac{1}{2} (2 \times 3 k_B T_m), \quad (C2)$$

where k_B is the Boltzmann constant. Defining a Lieder-mann ratio of melting χ_m by

$$(\langle \xi^2 \rangle)^{1/2} \simeq \chi_m d \quad (C3)$$

and choosing the mixing criterion to be $T_c/T_m < 1$, where T_m now is the smaller value of the two melting temperatures of the constituent compounds, we require that

$$\frac{T_c}{T_m} = \frac{\Omega k}{4R_g \alpha \chi_m^2 d^2} = \frac{3}{8} \frac{(d_{AC} - d_{BC})^2}{\chi_m^2 d^2} < 1 \quad (C4)$$

or

$$|\delta_0|/\delta_m < 1, \quad (C5)$$

where $\delta_m = 1.63\chi_m$ and δ_0 is the percentage bond-length difference.

¹J. C. Mikkelsen and J. B. Boyce, Phys. Rev. Lett. **49**, 1412 (1982); Phys. Rev. B **28**, 7130 (1983).

²A. Zunger and J. E. Jaffe, Phys. Rev. Lett. **51**, 662 (1983).

³J. L. Martins and A. Zunger, Phys. Rev. B **30**, 6217 (1984).

⁴A. Balzarotti, A. Kisiel, N. Motta, M. Zimnal-Starnawska, M. T. Czyzyk, and M. Podgorny, Phys. Rev. B **30**, 2295 (1984).

⁵A.-B. Chen and A. Sher, Microscience **3**, 1 (1984).

⁶A. Sher, A.-B. Chen, and W. E. Spicer, in *13th International Conference on Defects in Semiconductors*, edited by L. C. Kimerling and J. M. Parsey, Jr. (The Metallurgical Society of AIME, New York, 1985), p. 335.

⁷W. A. Harrison, *Electronic Structure and Properties of Solids* (Freeman, San Francisco, 1980); Microscience **3**, 35 (1983); Phys. Rev. B **27**, 3592 (1983).

⁸K. Shih, W. E. Spicer, W. A. Harrison, and A. Sher, Phys. Rev. B **31**, 1139 (1985).

⁹A. Baldereschi and J. J. Hopfield, Phys. Rev. Lett. **28**, 171 (1972).

¹⁰R. M. Martin, Phys. Rev. B **1**, 4005 (1970).

¹¹The experimental elastic constants were taken from the tabulated values in Refs. 10 and 25 except AlP and AlAs, for which we used the estimated values by J. D. Wilev, in *Semi-*

- conductors and Semimetals, edited by R. K. Willardson and A. C. Beer (Academic, New York, 1975), Vol. 10, p. 134.
- ¹²R. Kubuchi, *Physica* **103B**, 41 (1981).
- ¹³A.-B. Chen and A. Sher (unpublished).
- ¹⁴J. B. Boyce and J. C. Mikkelsen, unpublished data for Zn(Se,Te). We thank them for their communication prior to publication.
- ¹⁵Extrapolated results quoted in Ref. 3.
- ¹⁶G. B. Stringfellow, *J. Cryst. Growth* **27**, 21 (1974); **58**, 194 (1982).
- ¹⁷J. A. Van Vechten, in *Semiconductor Handbook*, edited by S. P. Keller (North-Holland, Amsterdam, 1980), Vol. 3, p. 1.
- ¹⁸P. A. Fedders and M. W. Muller, *J. Phys. Chem. Solids* **45**, 685 (1984).
- ¹⁹M. B. Panish and Ilegems, *Prog. Solid State Chem.* **7**, 39 (1972); A. Langier, *Rev. Phys. Appl.* **8**, 2959 (1973).
- ²⁰T. P. Pearshall, R. Carles, and J. C. Portal, *Appl. Phys. Lett.* **42**, 436 (1983).
- ²¹K. Kakimoto and T. Katoda, *Appl. Phys. Lett.* **40**, 826 (1982).
- ²²P. Parayanthal and F. H. Pollak, *Phys. Rev. Lett.* **52**, 1922 (1984).
- ²³G. P. Srivastova, J. L. Martins, and A. Zunger, *Phys. Rev. B* **31**, 2561 (1985).
- ²⁴N. A. Groyunova, A. S. Barshchhevskii, and D. N. Fretiakov, in *Semiconductors and Semimetals*, edited by R. K. Willardson and A. C. Beer (Academic, New York, 1968), Vol. 4, Chap. 1.
- ²⁵S. S. Mitra and N. E. Massa, in *Handbook on Semiconductors*, edited by W. Paul (North-Holland, Amsterdam, 1982), Vol. 1, p. 29.
- ²⁶L. M. Foster, *J. Electrochem. Soc. Solid State Sci. Technol.* **121**, 1662 (1974).
- ²⁷L. M. Foster and J. F. Woods, *J. Electrochem. Soc. Solid State Sci. Technol.* **118**, 1175 (1971).
- ²⁸R. Kubo, *Statistical Mechanics* (University of Tokyo Press, Tokyo, 1971), p. 336.
- ²⁹The critical temperature will be reduced by a few percent if more elaborate models are used. See W. Christian, in *Transformations in Metals and Alloys*, 2nd ed., edited by D. W. Hopkins (Pergamon, New York, 1981), p. 194.
- ³⁰*American Institute of Physics Handbook*, 3rd ed., edited by D. E. Gray (McGraw-Hill, New York, 1972), pp. 9–16.
- ³¹K. C. Hass, R. J. Lempert, and H. Ehrenreich, *Phys. Rev. Lett.* **52**, 77 (1984).

Sensitivity of defect energy levels to host band structures and impurity potentials in CdTe

A.-B. Chen

Physics Department, Auburn University, Auburn, Alabama 36849

A. Sher

SRI International, 333 Ravenswood Avenue, Menlo Park, California 94025

(Received 10 December 1984)

The sensitivity of defect energy levels in semiconductors to the host band structures and impurity potentials has been studied for approximately 30 impurities in CdTe using four different band-structure models. The discrepancies in the defect levels between two different sets of band structures and impurity potentials are found to range from less than 0.1 eV to the whole band gap (1.6 eV). The band-structure effects are analyzed here in terms of detailed partial densities of states. Examples of contradictory predictions from different band structures are illustrated, and ways to improve the theory are suggested.

I. INTRODUCTION

In several of our recent papers,¹⁻⁷ we have applied a method to calculate the band structure of semiconductors that is both efficient and accurate. Because the procedure involves casting the basis functions into orthonormal local orbitals⁶ (OLO), our method has the advantages common to empirical tight-binding (ETB) calculations,⁸⁻¹⁰ except that the Hamiltonian matrix elements to all ranges are retained. The inclusion of these higher coefficients makes it possible to produce excellent band structures including conduction bands and effective masses. The method also yields wave functions for optical property calculations.⁷ Moreover, its OLO description also permits its extension, through the coherent-potential approximation, to alloys.²⁻⁵

The recent attention focused on defects in semiconductors motivated us to apply our method to this problem. The theories of defects have ranged from very sophisticated self-consistent density-functional theory¹¹⁻¹³ (SCDF) to simple ETB calculations. It is generally recognized that SCDF is as accurate in defects for the ground-state properties as it is for pure semiconductors, but less certain in assigning excited energy levels. ETB, because it can produce results for many systems in one study, claims to predict the trends of deep levels¹⁰ even if the accuracy for a given impurity may be poor. However, this contention remains to be verified.

To assess this concern, we ask the following question: "How sensitive are defect levels to host band structures and impurity potentials?" To this end, we have adopted the simple yet nontrivial defect model, that of site-diagonal substitutional defects often used in ETB studies. CdTe was selected in this study because its band structure has been examined in great detail by us, and there are three published band-structure models⁸⁻¹⁰ that we could easily generate for comparison. There is also a considerable body of experimental data on deep states in this system.¹⁴⁻¹⁷

II. CALCULATIONAL PROCEDURE

In the simple site-diagonal substitutional defect model, the impurity energy levels E are determined by the equation

$$1 - \nu_\alpha g_\alpha(E) = 0, \quad (1)$$

where α designates the symmetry of a local state, e.g., Γ_6 , Γ_7 , and Γ_8 on an atomic site in the zinc-blende structure, and g_α is the real part of the diagonal matrix element of the host-crystal Green function. g_α can be calculated from the partial density of states (PDOS) by

$$g_\alpha(E) = \int \rho_\alpha(\epsilon)/(E - \epsilon) d\epsilon. \quad (2)$$

The PDOS is given by

$$\rho_\alpha(\epsilon) = \sum_{n,k} |a_n^\alpha(k)|^2 \delta(\epsilon - \epsilon_n(k)), \quad (3)$$

where $\epsilon_n(k)$ are band energies and $a_n^\alpha(k)$ are the probability amplitudes of the band state in the Bloch basis constructed from the OLO labeled by α . The Brillouin-zone integration in Eq. (3) is calculated using an accurate ray scheme.¹⁸

Because a principal concern of this paper is the sensitivity of impurity levels to the host band structures, we should emphasize the difference between our method and ETB. Our method consists of four steps.

(1) We start with four Gaussian orbitals per atom and empirical pseudopotentials,¹⁹ and compute the Hamiltonian matrix $H(k)$ and overlap matrix $S(k)$ as was done by Kane²⁰ and Chadi.²¹

(2) The Gaussian orbitals are transformed into OLO,⁶ so $H(k)$ is transformed into $H_0(k)$ and S into the identity matrix. The band structures calculated from $H_0(k)$ are accurate to 5% as compared to more sophisticated methods using the same potential.¹

(3) A spin-orbit Hamiltonian in the OLO basis⁴ is incorporated to deal with this interaction.

(4) To compensate for the effects of truncated basis and

nonlocal potentials, a perturbation Hamiltonian H_1 is added. H_1 has the same form as a truncated ETB Hamiltonian. The parameters in H_1 are adjusted to fine tune the important band energies and effective masses.¹⁻⁴

Although both ETB and our methods are empirical, there are two major differences.

(1) While most ETB retains the H matrix elements only to the first- or second-neighbor shell, ours extends to all ranges, so that the high Fourier components needed to produce the sharp band curvatures are properly given.

(2) Our method can directly generate wave functions for calculation of other properties.

Thus, while our method yields more accurate band structures, it retains much of the advantage of ETB, namely the computational speed and a simple direct-space description of the Hamiltonian.

III. BAND STRUCTURES AND PARTIAL DENSITIES OF STATES

Figure 1 depicts the four band structures to be considered for CdTe. Our result is in panel (a); panels (b) (Ref. 8) and (c) (Ref. 9) are two ETB band structures with the Hamiltonian matrix elements truncated at second neighbors. (Because different parameters were selected, these two band structures are not identical.) Panel (d) (Ref. 10) results from the use of five basis orbitals per atom; the extra one is an excited s state. All these band structures are adjusted to have the proper fundamental band gap of 1.6 eV. The principal differences one sees on first inspection are in the band curvatures, especially the conduction bands. The effective mass at the bottom of the conduction band in panel (a) is 0.1 times the free-electron mass, in agreement with experiment,¹⁷ while in other panels it is more than twice as large.

Figure 2 shows the densities of states (DOS) for each of the band structures in Fig. 1. While the valence bands at least exhibit general common features, the conduction bands are almost unrecognizable as representing the same compound. In panels (c) and (d), for example, there is a second band gap above the fundamental gap. Also note that there are two extra narrow peaks associated with the two extra excited s orbitals (one for Cd and the other for Te) included in the calculation.

To analyze the band effects on defect levels [see Eqs. (1) and (2)], the DOS is further decomposed into partial densities of states for $\Gamma_6(s)$, $\Gamma_7(p^{1/2})$, and $\Gamma_8(p^{3/2})$ states on the Cd and Te sites, as shown in Figs. 3–6. The Γ_8 PDOS are not shown because they are nearly the same as Γ_7 with only a slight upward energy shift. These PDOS show how the "atomic" levels evolve into band states. These curves contain useful information about many properties, e.g., the relation between the crystal bonding and atomic energies, and how potential disorder in alloys affects different parts of the bands,²⁻⁵ in addition to defect levels studied here.

The $\Gamma_6(\text{Cd})$ PDOS shown in Fig. 3 split between the conduction and valence bands. It is generally assumed that the cation s states in III-V and II-VI compounds

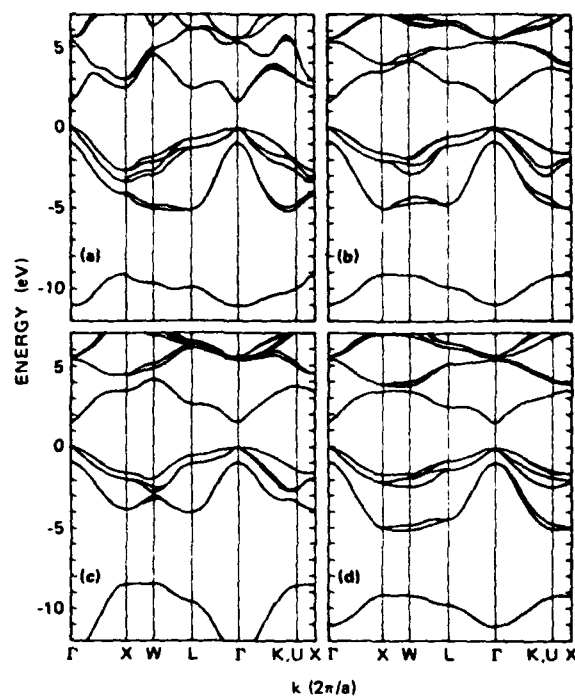


FIG. 1. Four band structures of CdTe used for comparative studies: (a) present work, (b) Ref. 8, (c) Ref. 9, and (d) Ref. 10.

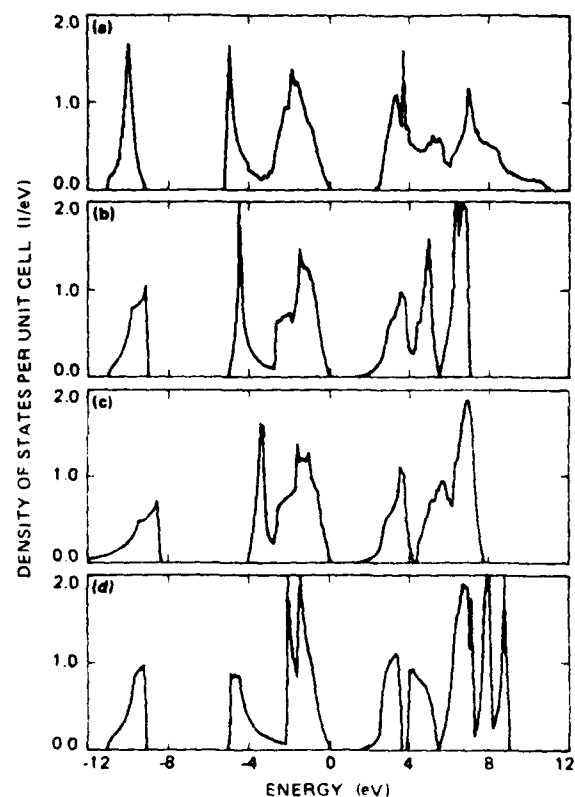
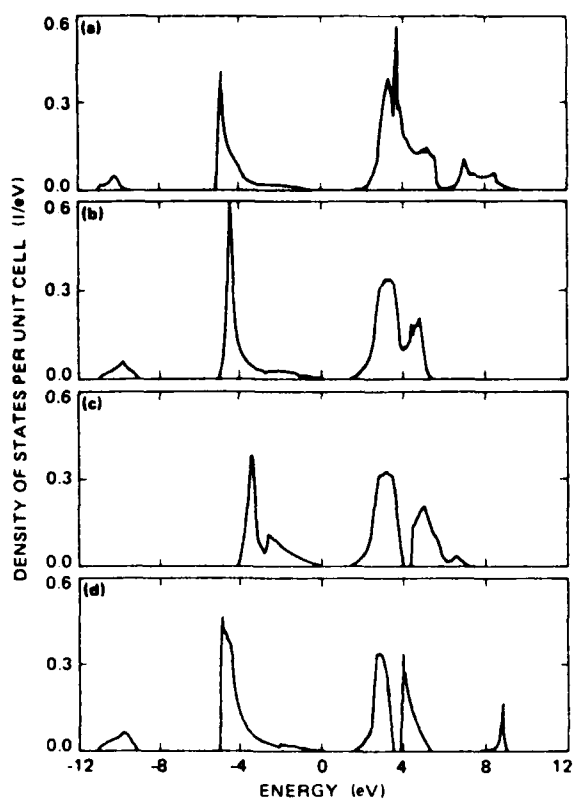
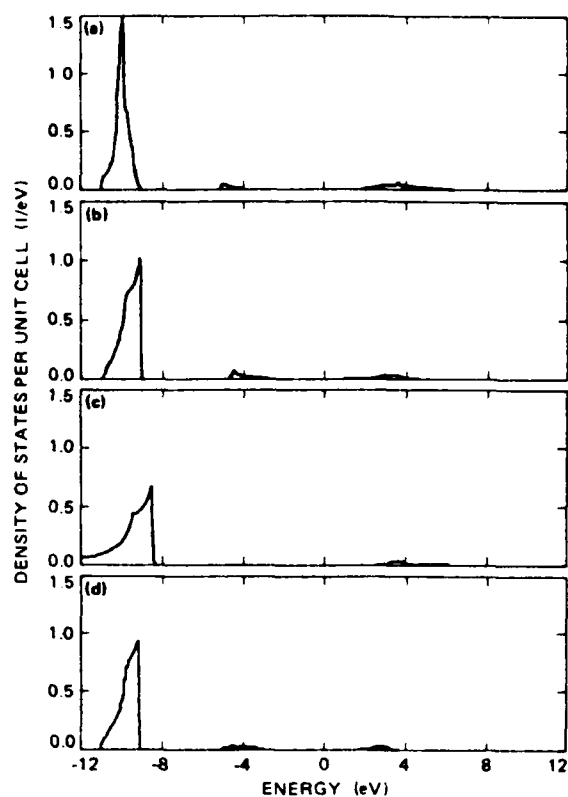
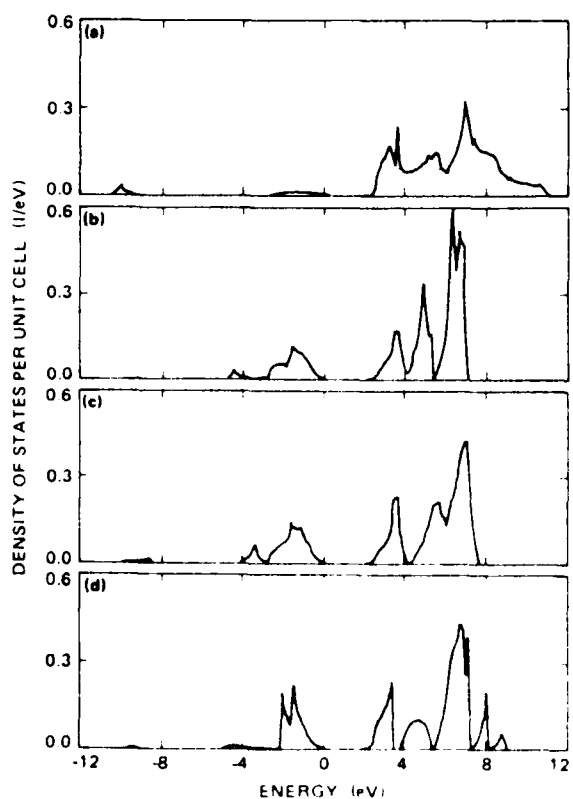
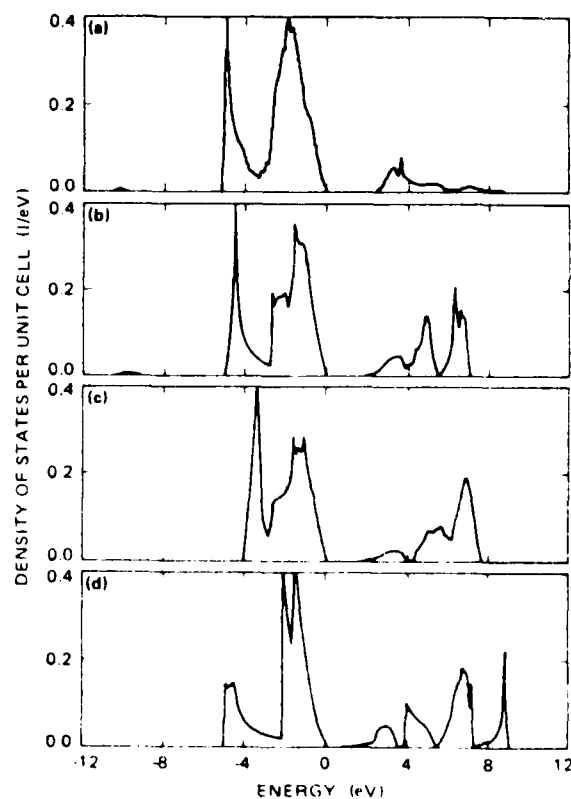


FIG. 2. Densities of states calculated from the four band structures in Fig. 1.

FIG. 3. The Cd Γ_6 partial densities of states.FIG. 5. The Te Γ_6 partial densities of states.FIG. 4. The Cd I_3 partial densities of states.FIG. 6. The Te I_3 partial densities of states.

evolve into the conduction bands, while the anion p states make up most of the major valence bands just below the gap. Thus it is perhaps a surprise to see a prominent peak derived from the cation s states at the bottom of the major valence-band structure. However, this is a general feature for all sp^3 -based compound semiconductors. These are the states responsible for the first observed breakdown of the virtual-crystal approximation for a semiconductor alloy: $\text{Hg}_{1-x}\text{Cd}_x\text{Te}$ (which is caused by the large s -energy shift between the Cd and Hg sites).^{4,5,22}

A more detailed examination draws attention to some important differences among the four panels in Fig. 3: the valence-band peak in panel (c) is about 2 eV higher than the rest, and it is also high compared to experiment.²² Our conduction-band PDOS in panel (a) is broader than the others. The ratio of the integrated PDOS in the conduction bands to that in the valence bands in our model is larger than those in other panels. Also our PDOS just below the valence-band edge is obviously smaller than that found in other models.

Figure 4 shows that the Cd p states are concentrated in the conduction-band states. This is particularly true in panel (a), where their contribution to the valence-band states shrinks almost to nothing. In other panels, there are still sizable ($\sim 20\%$) valence-band states. In contrast,

all four panels in Fig. 5 show that the Te s states are confined to the deep valence-band states, as generally recognized. Finally, Fig. 6 shows that the Te p states dominate the upper valence-band states. Panel (a) has much less conduction-band content than the other three panels. As we will see, these differences can result in quantitatively or even qualitatively different predictions about the deep levels.

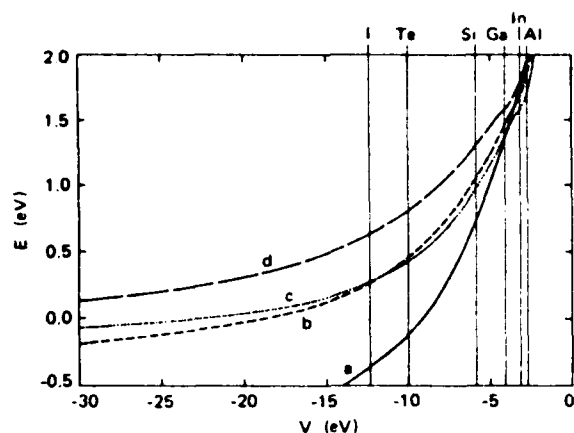
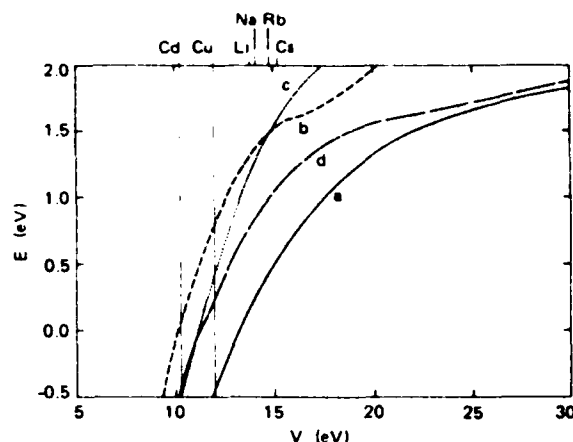
IV. IMPURITY-LEVEL DETERMINATION

A convenient way to study the impurity energy levels using Eq. (1) is to rewrite it as $v_a = 1/g_a(E)$ and plot E as a function of v . Once this E - v curve is deduced for each α , the deep levels E_a for a given impurity can be read off the curve by drawing a vertical line at the appropriate value of v_a for the impurity. We set the zero of energy at the top of the valence bands. Because the gap is 1.6 eV, we will focus on levels in the energy range from -0.5 to 2.0 eV.

Calculations have been performed for all neutral impurities listed in Table I. Because we do not believe that there exists a uniformly accepted table for v we have adopted a table that we used for structural studies.^{23,24} Table I lists the term values, which we obtained from to-

TABLE I. s - and p -state correlated term values in units of $-eV$. The top entry is the s -state, the second the $p_{1/2}$ -state, and the third the $p_{3/2}$ -state energy. (All energies are negative.)

I	II	III	IV	V	VI	VII
Li	Be	B	C	N	O	F
5.390	9.320	14.003	19.814	26.081	28.551	36.229
	5.412	8.300	11.260	14.540	13.613	17.484
	5.412	8.300	11.260	14.540	13.610	17.420
Na	Zn	Al	Si	P	S	Cl
5.140	9.390	11.780	15.027	19.620	21.163	25.812
	4.237	5.980	8.150	10.610	10.449	13.136
	4.011	5.980	8.150	10.550	10.360	13.010
K	Cd	Ga	Ge	As	Se	Br
4.340	8.990	13.230	16.396	20.015	21.412	24.949
	4.313	6.000	7.880	10.146	10.188	12.353
	4.097	5.850	7.694	9.810	9.750	11.840
Rb	Hg	In	Sn	Sb	Te	I
4.180	10.430	12.032	14.525	17.560	19.120	21.631
	4.998	5.780	7.340	9.391	9.951	11.470
	4.031	5.453	6.879	8.640	9.010	10.450
Cs			Pb			
3.890			15.250			
			7.410			
			5.979			
Cu						
7.720						
Ag						
7.570						
3.647						
3.487						
Au						
9.220						
4.349						
3.688						

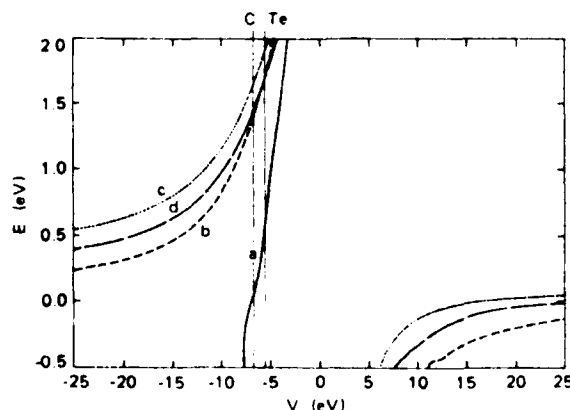
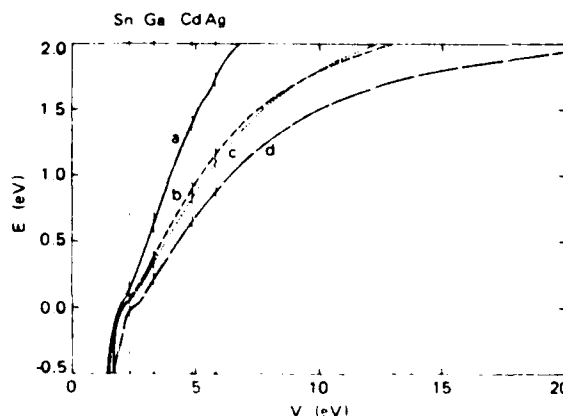
FIG. 7. The E - v curves for the Γ_6 states on a Cd site.FIG. 9. The E - v curves for the Γ_6 states on a Te site.

tal energy differences between atomic configurations calculated using the norm-conserved pseudopotentials²⁵ and self-consistent charge-density-functional theory, with the first ionization energies adjusted to be the experimental values.²⁶ These term values are found to yield consistently better structural properties²³ in Harrison's theory^{27,28} than those based on Mann's values²⁹ adopted by Harrison.²⁸ The impurity-potential parameters will then be taken as the difference of the term values between the impurity atom and Cd (or Te). To study the sensitivity of E_a to v_a , we shift v_a by ± 0.5 eV and compute the corresponding changes in the energy levels.

Figures 7–10 display the E - v curves for several α . Each figure has four curves, corresponding to the four panels of PDOS in each of Figs. 3–6. The functional behavior of these curves can be understood qualitatively using Eq. (2) and Figs. 3–6. If E lies in the gap, the contribution from conduction bands is negative, but positive from the valence bands. The closer the PDOS to the E in question, the larger will be its influence. Applying this argument to the $\Gamma_6(\text{Cd})$ representation, we see that the curves in Fig. 7 are negative in the gap region because the PDOS in Fig. 3 near the bottom of the conduction bands are much larger than those near the valence-band top. Thus, on the Cd site, only impurities with an s energy

below the Cd s level (-8.99 eV) will produce a Γ_6 level in the gap. However, we note that in Fig. 7, $g_a(E)=0$ for models (b) and (c) just below the valence-band edge because of cancellation between the conduction- and valence-band contributions. At this E value, the E - v curve switches from $v=-\infty$ to $v=\infty$ (not shown); an ideal vacancy level (corresponding to $v_a=\infty$) is located at this E . A similar consideration, but with the conduction and valence bands interchanged, leads to an understanding of the curves in Fig. 10. Using the same principle, we can easily understand why all curves in Fig. 9 for the $\Gamma_6(\text{Te})$ representation are positive, but the reasons for the large displacements between these curves are not easy to deduce. In Fig. 8, the curve labeled a is distinctively different from other curves, because the PDOS in panel (a) in Fig. 4 is completely dominated by the conduction band; however, for the other panels the PDOS just below the valence-band edge are as large as those just above the conduction-band edge. This produces a very sharp negative E - v curve for (a), but split behavior for (b), (c), and (d).

These E - v curves provide a clear picture of how different host band structures may affect the deep levels. Numerical values for the impurity levels can be obtained from these figures by drawing vertical lines at the ap-

FIG. 8. The E - v curves for the Γ_6 states on a Cd site.FIG. 10. The E - v curves for the Γ_6 states on a Te site.

proprate impurity potentials (i.e., differences between the term values listed in Table I), as has been shown for several representative impurities. To provide a more quantitative comparison, Table II lists some calculated impurity levels E_a and the corresponding changes ΔE_a due to the 1-eV change in v_a .

V. RESULTS AND CONCLUSION

To summarize we recall that band models (b) and (c) are the same second-neighbor ETB with two different sets of parameters, and model (d) is a first-neighbor ETB with one extra s orbital per atom. Our model [model (a)] has the form of ETB but is derived in a very different manner and includes all the long-range interactions. Therefore, we expect that the results from models (b) and (c) will be close, model (d) will have larger discrepancies from (b) and (c) than that between (b) and (c), and model (a) will differ even more. This is evident from Figs. 7–10 and Table II. We found the energies for the $\Gamma_6(\text{Cd})$, $\Gamma_7(\text{Te})$, and $\Gamma_8(\text{Te})$ states produced by models (b) and (c) agree within 0.1 eV. For the other states, i.e., $\Gamma_6(\text{Te})$, $\Gamma_7(\text{Cd})$, and $\Gamma_8(\text{Cd})$, the energies from (b) and (c) are qualitatively similar, but the difference can be as large as 0.4 eV. The largest discrepancy between models (d) and (b) [or (c)] is more than 0.5 eV, and that between (a) and other models is more than 1 eV. The largest difference comes from the

p levels on a Cd site. For example, the filled p level of C on a Cd site in model (a) is a resonance state just below the valence-band edge but is a donor state in the other models. Similarly, model (a) puts the neutral Te antisite defect p levels at about $\frac{1}{3}$ and $\frac{2}{3}$ of the gap [$E(\Gamma_7)=0.48$ eV and $E(\Gamma_8)=0.95$ eV], while other models assign them as resonance states inside the conduction bands. We also note that the discrepancies between different models are not uniform, but vary with v_a . Consider $\Gamma_6(\text{Cd})$ for example. All four models yield the same ordering and about the same energies for the group-III impurities Al, In, and Ga. However, as v becomes more negative, the splitting between the curves increases, so the discrepancies become larger [~ 1 eV difference between models (a) and (d) for I impurity]. Similarly, for the $\Gamma_7(\text{Te})$ states, all four models put the Sn impurity energies close to the valence-band edge, but the agreement deteriorates as v_a increases.

Regarding the sensitivity of energy levels to impurity potentials, Table II shows that a 1-eV shift in v_a produces a change in E_a ranging from less than 0.1 to 0.65 eV. Very little is known about the size or trends in errors introduced in v_a from the use of atomic term values. However, we know that the discrepancy of v_a between two different tables of atomic term values can be larger than 2 eV. This discrepancy translates into an uncertainty of less than 0.1 to more than 1 eV in the impurity energy levels,

TABLE II. Defect energy levels E and changes ΔE due to a 1-eV change in the impurity-potential parameter. All energies are in units of eV. V_0 stands for ideal vacancy.

Defect	Model (a)		Model (b)		Model (c)		Model (d)	
	E	ΔE	E	ΔE	E	ΔE	E	ΔE
Γ_6 on Cd site								
Ga	1.29	0.39	1.42	0.24	1.33	0.23	1.57	0.18
C	-0.21	0.09	0.38	0.09	0.36	0.13	0.74	0.08
Si	0.67	0.30	1.02	0.10	0.93	0.19	1.27	0.15
P	0.19	0.11	0.39	0.09	0.38	0.08	0.75	0.08
O	< -0.5		-0.02	0.02	0.04	0.01	0.32	0.02
Te	-0.13	0.13	0.44	0.10	0.42	0.08	0.79	0.09
Cl	< -0.5		0.06	0.03	0.10	0.02	0.41	0.04
V_0	< -0.5		< -0.5		-0.30		-0.20	
Γ_7 on Cd site								
C	-0.02	0.37	1.32	0.22	1.59	0.20	1.39	0.19
Si	1.57	0.65	2.0		2.0		2.0	
P	0.16	0.38	1.48	0.26	1.73	0.23	1.52	0.21
O	< 0.5		0.89	0.14	1.22	0.13	1.03	0.12
Te	0.48	0.55	1.60	0.29	1.88	0.23	1.66	0.24
Cl	< 0.5		0.96	0.17	1.29	0.14	1.09	0.14
V_0	< 0.5		0.00		0.21		0.06	
Γ_8 on Te site								
Li	0.14	0.29	1.28	0.22	1.15	0.35	0.76	0.25
Cu	< 0.5		0.54	0.42	0.12	0.52	0.03	0.32
Γ_8 on Te site								
Ag	1.89	0.32	1.26	0.22	1.21	0.23	0.99	0.20
Cd	1.66	0.34	1.11	0.26	1.05	0.26	0.85	0.22
Ga	0.98	0.49	0.61	0.33	0.55	0.32	0.40	0.30
Si	0.07	0.40	0.11	0.36	0.13	0.38	0.38	0.72
Sn	0.28	0.47	0.15	0.31	0.13	0.24	0.02	0.28

which is comparable to that due to different host band structures.

Putting this large uncertainty in the deep levels against a band gap of 1.6 eV, we are left with great doubts about the predictability of this oversimplified theory. Unfortunately, the experimental means available for identifying microdefects in semiconductors are still very limited, and the *ab initio* band theory is still not capable of accurately predicting the energy levels. Thus, there is a great temptation to use simple theories like the one carried out here to help with the identifications. To illustrate this point, consider the following examples: Table II shows that Li on a Te site has an *s* level of 0.14 eV in model (a), so one may be tempted to relate it to the acceptor state identified experimentally.¹⁴ However, this is not the hydrogenic acceptor state on a Cd site, as one might anticipate. One might also want to assign the $\frac{1}{2}$ and $\frac{3}{2}$ gap states for the Te antisite *p* levels on the Cd site found from model (a) as those seen in experiments.^{15,16} Because of the large uncertainty in the calculation, these results should be regarded as suspicious surprises rather than theoretical confirmations.

The results presented here should not discourage continued research on the ETB approach, but improvement is clearly needed. Work ranging from universal^{23,27,30} to specific^{24,31,32} structural studies to our band calculations and alloy studies¹⁻⁷ indicates that the ETB type of theory is practical for both bonding properties and electronic structures. The reason that ETB works well for some properties, e.g., photoemission spectra and bonding properties, but not for impurity levels, is that the former depend only on the gross total density of states, while the

latter have been shown to be sensitive to the details of the partial densities of states.

To establish the credibility of ETB in defect studies, one needs to look at the problem more seriously. The most difficult and yet important task is to develop a better way for determining the Hamiltonian matrix elements. Haas *et al.*⁸ and Harrison^{27,28} have suggested using the atomic term values as the diagonal matrix elements. Our work¹⁻⁴ has suggested using a universal long-range interaction to improve the accuracy of the conduction bands. Several studies^{1,27,28,33} have also pointed out scaling rules of the matrix elements. A combination of these ideas may lead to an acceptable model. Secondly, both the bonding and deep-level states of impurities should be studied at the same time in order to provide correlated information for defect identification. Finally, more realistic models should be examined. Besides the substitutional site-diagonal defects, one should consider the possibility of interstitial, paired, and even more complex defects. One also needs to deal with long-range impurity potentials, possible charge shifts, and lattice distortions. Progress in all these areas can be expected if the calculation is constantly correlated with experiments and available *ab initio* theory.

ACKNOWLEDGMENTS

This work was supported by AFOSR Contract No. F49620-81-K0012 and Grant No. AFOSR-84-0282. A.-B. Chen would like to thank Professor W. E. Spicer of Stanford University for his hospitality.

¹A.-B. Chen and A. Sher, Phys. Rev. B 22, 3886 (1980).

²A.-B. Chen and A. Sher, Phys. Rev. B 23, 5645 (1981).

³A.-B. Chen and A. Sher, Phys. Rev. B 23, 5360 (1981).

⁴A.-B. Chen and A. Sher, J. Vac. Sci. Technol. 121, 138 (1982).

⁵W. E. Spicer, J. A. Silberman, J. Morgan, J. Lindau, J. A. Wilson, A.-B. Chen, and A. Sher, Phys. Rev. Lett. 149, 948 (1982).

⁶A.-B. Chen and A. Sher, Phys. Rev. B 26, 6603 (1982).

⁷A.-B. Chen, S. Phokaichapattana, and A. Sher, Phys. Rev. B 23, 5360 (1981).

⁸K. C. Hass, H. Ehrenreich, and B. Velicky, Phys. Rev. B 27, 5360 (1983).

⁹C. A. Swarts, M. S. Daw, and T. C. McGill, J. Vac. Sci. Technol. 121, 199 (1982).

¹⁰A. Kobayashi, O. F. Sankey, and J. D. Dow, Phys. Rev. B 25, 6367 (1982).

¹¹J. Bernhole, N. O. Lipari, and S. T. Pantelides, Phys. Rev. B 21, 3545 (1980).

¹²G. A. Baraff, E. O. Kane, and M. Schluter, Phys. Rev. B 21, 5662 (1980).

¹³G. B. Bachelet, M. Schluter, and G. A. Baraff, Phys. Rev. B 27, 2545 (1983).

¹⁴K. Zanio, in *Semiconductors and Semimetals*, edited by R. Willardson and A. C. Beer (Academic, New York, 1978),

Vol. 13.

¹⁵C. E. Jones, V. Nair, J. Lundquist, and D. L. Polla, J. Vac. Sci. Technol. 21, 187 (1982).

¹⁶R. T. Collins and T. C. McGill, J. Vac. Sci. Technol. A1, 1833 (1983).

¹⁷K. K. Kanazawa and F. C. Brown, Phys. Rev. 135, A1767 (1964).

¹⁸A.-B. Chen, Phys. Rev. B 16, 3291 (1977).

¹⁹D. J. Chadi, J. P. Walter, and M. L. Cohen, Phys. Rev. B 5, 3058 (1972).

²⁰E. O. Kane, Phys. Rev. B 13, 3478 (1976).

²¹D. J. Chadi, Phys. Rev. B 16, 3572 (1977).

²²J. A. Silberman, P. Morgan, W. E. Spicer, and J. A. Wilson, J. Vac. Sci. Technol. 21, 342 (1982).

²³A.-B. Chen and A. Sher, Microscience 3, 1 (1984).

²⁴A. Sher, A.-B. Chen, and W. E. Spicer, in *International Conference on Defects in Semiconductors*, edited by J. C. Kimerling and J. M. Parsey, Jr., The Metallurgical Society of AIME, 1985, p. 235.

²⁵G. B. Bachelet, D. Hamman, and M. Schluter, Phys. Rev. B 26, 4199 (1982).

²⁶C. Kittel, *Introduction to Solid State Physics* (John Wiley, New York, 1976), p. 75, Table 2.

²⁷W. A. Harrison, *Electronic Structure and Properties of Solids*

(Freeman, San Francisco, 1980).

²⁸W. A. Harrison, *Microscience* 3, 35 (1983).

²⁹J. B. Mann, *Atomic Structure Calculations, I: Hartree-Fock Energy Results for Elements Hydrogen to Lawrencium* (Clearinghouse for Technical Information, Springfield, Virginia, 1967).

³⁰D. G. Pettifor and R. Podloucky, *Phys. Rev. Lett.* 53, 826 (1984).

³¹D. C. Allan and E. J. Mele, *Phys. Rev. Lett.* 53, 826 (1984).

³²D. J. Chadi, *Phys. Rev. Lett.* 52, 1911 (1984).

³³O. K. Andersen, W. Klase, and M. Nohl, *Phys. Rev. B* 17, 1209 (1978).

Binding Energy and Spectral Width of Si 2p Core Excitons in Si_xGe_{1-x} Alloys

S. Krishnamurthy and A. Sher

Physical Electronics Laboratory, SRI International, Menlo Park, California 94025

and

A.-B. Chen^(a)

Department of Physics, Auburn University, Auburn, Alabama 36849

(Received 24 January 1985)

A calculation is presented to explain the anomalous experimental behavior of the Si 2p core-exciton binding energy and linewidth in Si_xGe_{1-x} alloys. The observed minimum in the linewidth near $x \approx 0.15$ can be explained as the result of a competition between intrinsic broadening due to screening and extrinsic alloy broadening. For pure Si, the binding energy is estimated to be 0.15 ± 0.05 eV and the width is shown to be smaller than that observed at $x \approx 0.15$.

PACS numbers: 71.55.Fr, 71.35.+z, 78.70.Dm

Until 1984, the Si 2p core exciton was believed to have an anomalously large binding energy.¹⁻¹⁰ Later, Newman and Dow¹¹ proposed a radically different picture in which the Si 2p core exciton is in fact a resonance with a negative binding energy. They further predicted that the exciton binding energy remains negative throughout most of the Si_xGe_{1-x} alloy composition range, except near $x \approx 0.20$ where it becomes positive. In a recent experiment,¹² Bunker *et al.* found an anomalous sharpening of the exciton spectra near $x = 0.15$; the data were interpreted to support the Newman-Dow point of view. Yet the most recent experiment¹³ still suggests a positive value for the binding energy E_b^0 in silicon.

In this Letter, we present a calculation that offers a plausible resolution to the above problem. In our theory, the calculated Si 2p core-exciton binding energy $E_b(x)$ and the linewidth $\Delta(x)$ in Si_xGe_{1-x} alloys are sensitively dependent on the parameter E_b^0 . A comparison of the calculated $\Delta(x)$ with the experiment¹² suggests a positive value 0.15 ± 0.05 for E_b^0 . The anomalous experimental spectrum¹² near $x \approx 0.15$ is explained as a result of a competition between an intrinsic broadening Δ_i due to screening and an extrinsic alloy broadening Δ_A . In the present theory, there is no need to suppose that the exciton suddenly changes its character from an extended effective-mass-like state to a deep localized state.

We need to calculate E_b and $\Delta = \Delta_i + \Delta_A$ as a function of alloy concentration x . The calculations are based on a quantitative coherent-potential-approximation (CPA) band structure. Details of the CPA calculations will be presented elsewhere. Below, we briefly discuss a Green's-function method for calculating E_b and Δ .

The one-particle effective Green's function in CPA takes the form

$$G(E) = [E - \bar{H} - \Sigma(E)]^{-1}, \quad (1)$$

where \bar{H} is the virtual-crystal approximation Hamil-

tonian and $\Sigma(E)$ is the self-energy. The site-diagonal Green's function is denoted as

$$F_\alpha(E) = \langle \phi_\alpha | G(E) | \phi_\alpha \rangle, \quad (2)$$

where ϕ_α is a localized orbital of specified symmetry. Here we only need to consider $\alpha = s$ for A_1 symmetry. The corresponding function in pure Si is denoted as $F_s^0(E)$. Following the theoretical treatment of deep substitutional-impurity levels,⁸ the core-exciton level for pure Si is determined by

$$F_s^0(E) = (V - E_s^{Si})^{-1}, \quad (3)$$

where E_s^{Si} is the site potential seen by an s electron in bulk silicon, and V is a central-potential parameter. For a chosen value of V_b , Eq. (3) can be solved for E , and vice versa. Then $E_b^0 = E_c^0 - E$, where E_c^0 is the conduction-band edge in pure silicon. Because of the uncertainties in the value of experimental E_b^0 and theoretical V , we treat E_b^0 (or V) as a parameter. The binding energy E_b in a Si_xGe_{1-x} alloy can be calculated by solving

$$F_s(E) = [V - \bar{E}_s - \Sigma_s(E)]^{-1}, \quad (4)$$

where

$$\bar{E}_s = xE_s^{Si} + (1-x)E_s^{Ge}. \quad (5)$$

Then E_b is given by

$$E_b = E_c - E. \quad (6)$$

The calculated values of the conduction-band edge and the exciton level measured relative to the top of the valence band are plotted in Fig. 1. The band gap increases with x with a slope discontinuity at ≈ 0.15 . The dashed lines a , b , and c represent exciton levels obtained with $E_b^0 = 0.1$, 0.15 , and 0.30 eV, respectively. The binding energy E_b is also an increasing function of x , with a slope discontinuity near $x \approx 0.15$. The CPA introduces a slight bowing in E_c and E_b .

Strinati¹⁰ has calculated the variation of Δ_i with E_b

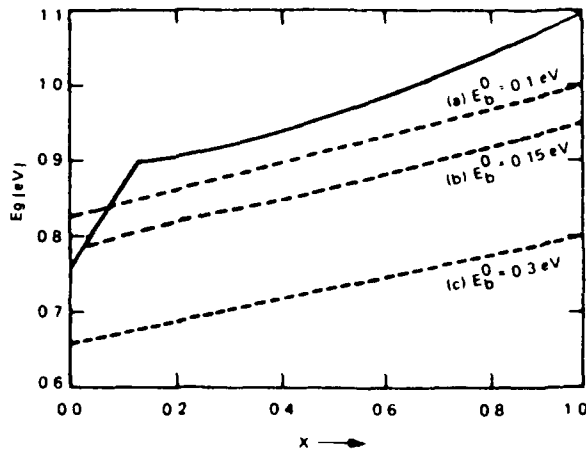


FIG. 1. Variation of the band gap (solid line) and the Si 2p core-exciton level with x in $\text{Si}_x\text{Ge}_{1-x}$ alloys. The energy is measured from the top of the valence band. The dashed curves a , b , and c represent exciton levels calculated with $E_b^0 = 0.1, 0.15$, and 0.3 eV, respectively.

by replacing the short-range Coulomb potential with a spherical square well of variable depth and a screened Coulomb tail. Strinati's results can be used to estimate Δ_I corresponding to the calculated E_b . Δ_I decreases rapidly with E_b , then saturates for larger E_b .

The contribution to the natural linewidth from the alloy broadening is calculated by a consideration of the electron part of the exciton wave function, ψ_s . The ψ_s is expanded in a linear combination of the s part of the conduction-band wave functions ϕ_n^s :

$$\psi_s(\mathbf{k}) = \sum_{n,s} C_{ns} \phi_n^s(\mathbf{k}). \quad (7)$$

We found that alloy scattering is only moderate and s scattering is dominant; thus, the alloy broadening $\Delta_A(E)$ is well approximated by

$$\Delta_A(E) \approx x(1-x)\delta_s^2 \text{Im}F_s(E), \quad (8)$$

where δ_s is the difference between E_s^{Si} and E_s^{Ge} . Hence, the alloy-broadening contribution to Δ is related to the alloy broadening of the band states, $\Delta_n(\mathbf{k}, E)$:

$$\begin{aligned} \Delta_A &= \frac{1}{N} \sum_{\mathbf{k}} (\psi_s(\mathbf{k}) | \Delta_A(E) | \psi_s(\mathbf{k})) \\ &= \frac{1}{N} \sum_{\mathbf{k}} \sum_n C_{ns}^2 \Delta_n(\mathbf{k}, E) \\ &= \int \rho_s(E) \Delta_A(E) dE \\ &= x(1-x)\delta_s^2 \pi \int \rho_s^2(E) dE. \end{aligned} \quad (9)$$

The integral in Eq. (9) is evaluated numerically.

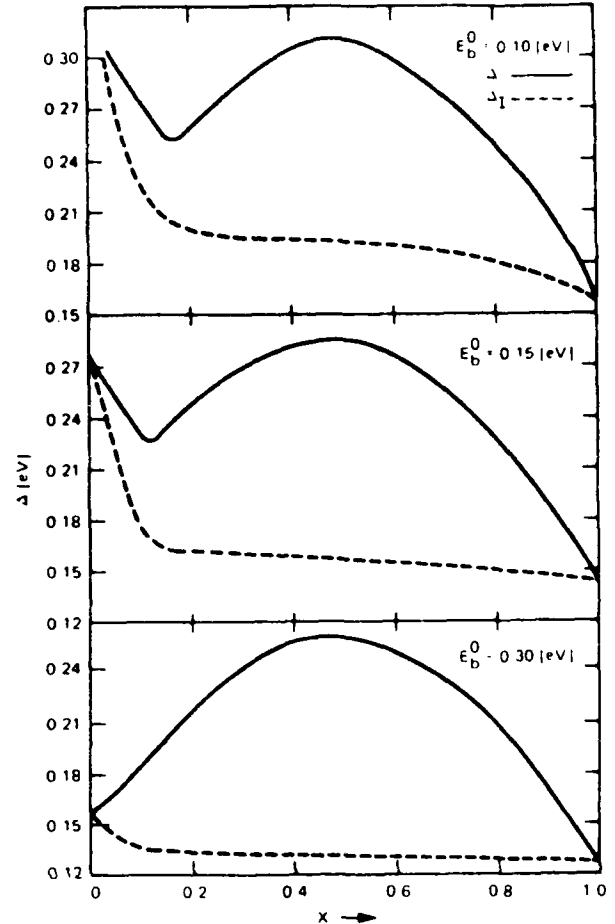


FIG. 2. Variation of Δ (solid lines) and Δ_I (dashed lines) with x for three E_b^0 values.

The calculated Δ , which is the sum of Δ_I and Δ_A , is plotted against x in Fig. 2 for three values of E_b^0 . In all three panels, the dashed curve represents Δ_I and the solid line represents Δ . It is seen from Fig. 1 that the exciton level follows the X edge of the conduction band. Hence the binding energy E_b , relative to the conduction band edge, remains almost constant (for a given E_b^0) until the minimum switches from the X edge to the L edge. Because of the change in the slope of E_g , E_b decreases rapidly when L becomes the minimum. Correspondingly, Δ_I varies slowly until the X to L crossover and then increases rapidly. This feature is clearly seen in Fig. 2.

For $E_b^0 = 0.15$, the Δ_I and Δ_A are comparable near $x = 0.50$, and Δ_I dominates for all small x and large x . These two competing mechanisms give a relative minimum near $x \approx 0.15$, a broader maximum near $x \approx 0.50$, and a smaller minimum for pure silicon. As E_b^0 is decreased, the relative minimum is shifted to larger x , e.g., the minimum shifts to $x = 0.20$ for $E_b^0 = 0.10$ eV. For $E_b^0 = 0.15$ eV, the position of the

relative minimum is in agreement with the experiment.¹² (By measuring the relative width at $x \approx 0.15$ to that at $x = 1$, one can make a better estimate of E_b^0 .) To correlate the theory with experiment, the calculated $1/\Delta^2$ is compared with the measured¹² $(\Delta\mu)^{-1}(d\mu/dE)_{\max}$ in Fig. 3, where $\Delta\mu$ is the edge step and $(d\mu/dE)_{\max}$ are the maximum values of the derivative of absorption spectra with respect to photon energy. Because the experimental values are given in arbitrary units, the values are normalized to agree at $x = 0.5$. The observed anomalous behavior near $x = 0.15$ and the qualitative x dependence in that region is clearly replicated by the theory. However, the calculation predicts a larger maximum at $x = 1$. It would be interesting to have experiments that cover the entire range of x to further test this prediction.

For larger values of E_b^0 , the calculated E_b is also large and hence Δ_f decreases slowly with x . Because the broadening is determined mainly by Δ_4 , the linewidth is expected to be small for $x = 0$ and $x = 1$ only; this occurs for $E_b^0 = 0.30$ eV. For negative values of E_b^0 , E_b remains negative for all values of x . Accordingly, the linewidth is broad for all x , and there would be no such anomaly as in Fig. 3.

The calculations presented in this Letter are slightly different from alchemy approximations.⁸ We treat the central-cell potential V as a parameter and narrow its range from other considerations. We examine values of $V - E_s^{Si}$ of -8.49 , -7.09 , and -6.56 eV, corresponding to E_b^0 values of 0.30 , 0.15 , and 0.10 eV, respectively. If the strict alchemy approximation were taken, the value of $V - E_s^{Si}$ would be $E_s^P - E_s^{Si} = -4.59$ eV in the tight-binding approximation, and a negative

E_b^0 (~ -0.10 eV) would be obtained. When long-range interactions are included, however, the above resonance state becomes a shallow donor level, which is the experimental situation for a P impurity in Si. Our results suggest that V for core excitons in Si is deeper than those implied by alchemy approximations. However, if we use the alchemy approximation as a means of scaling, the value of V for Ge $3p$ core excitons should be deeper than that for Si $2p$ core excitons. Hence, the curve corresponding to $E_b^0 = 0.30$ in Fig. 2 should be a reasonable estimate for Ge $3p$ core-exciton binding energy in alloys. Therefore, we do not expect to see an anomalous behavior of Δ in alloys for this case.

In summary, the present calculations of the Si $2p$ core-exciton binding energy and linewidth suggest that the exciton level is about 0.15 ± 0.05 eV below the conduction-band edge for pure Si. It follows the X edge for $x > 0.15$ in the Si_xGe_{1-x} alloys, and E_b may eventually reach zero in the dilute limit $x \rightarrow 0$. Our value for E_b^0 represents the lower end of the previous measurements,¹⁻⁶ but is in good agreement with a recent experimental¹³ value of 0.120 ± 0.03 eV. By considering the intrinsic linewidth and the alloy broadening, we can explain the observed relative minimum in the linewidth near $x \approx 0.15$, without requiring a sudden change of the exciton character. On the basis of this calculation, we expect the corresponding width in pure Si to be even smaller than that observed near $x = 0.15$. We further argue that the binding energy of Ge $3p$ core excitons should be larger than that of Si $2p$ core excitons and there should be no anomaly in the Ge $3p$ linewidth in alloys.

This work was supported in part by the U.S. Department of Defense Advanced Research Projects Agency, under Contract No. MDA 903-83-C-0108 and the Air Force Office of Science Research through Grant No. AFOSR-84-0282. One of us (A.-B.C.) would like to thank Professor W. E. Spicer for his hospitality at Stanford University.

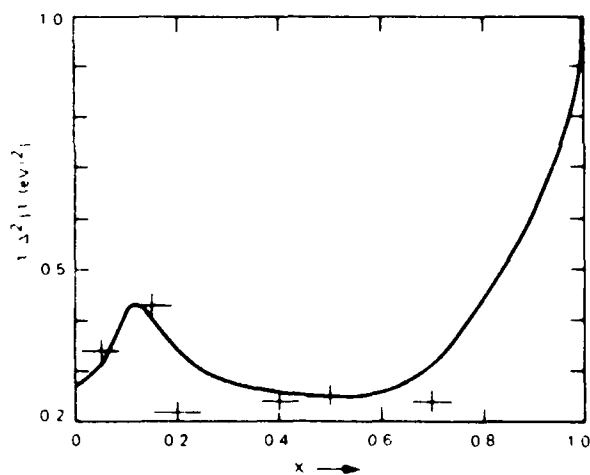


FIG. 3. The calculated $1/\Delta^2$ values (solid line) compared with the experimental results (marks) from Ref. 12. The value of calculated $\Delta(\text{Si})$ is 0.127 eV. The experiment is normalized to the theory at $x = 0.5$.

^(a)Visiting professor at Stanford University.

^(b)W. Eberhardt, G. Kalkoffen, C. Kunz, D. E. Aspnes, and M. Cardona, Phys. Status Solidi (b) **88**, 135 (1978).

^(c)M. Altarelli and D. L. Dexter, Phys. Rev. Lett. **29**, 1100 (1972).

^(d)F. C. Brown, R. S. Bachrach, and M. Skibowski, Phys. Rev. B **15**, 4781 (1977).

^(e)R. S. Bauer, R. S. Bachrach, J. C. McMenamin, and D. E. Aspnes, Nuovo Cimento **39B**, 409 (1977).

^(f)G. Margaritondo and J. E. Rowe, Phys. Lett. **59A**, 464 (1977).

^(g)G. Margaritondo, A. Franciosi, N. G. Stoffel, and H. S.

- Edelman, Solid State Commun. **36**, 298 (1980).
⁷C. Kunz, J. Phys. (Paris), Colloq. **39**, C4-119 (1978).
⁸H. P. Hjalmarson, H. Büttner, and J. D. Dow, Phys. Rev. B **24**, 6010 (1981).
⁹M. Altarelli, Phys. Rev. Lett. **46**, 205 (1981).
¹⁰G. Strinati, Phys. Rev. Lett. **49**, 1519 (1982).
¹¹K. E. Newman and J. D. Dow, Solid State Commun. **50**, 587 (1984).
¹²B. A. Bunker, S. L. Hulbert, J. P. Stoll, and F. C. Brown, Phys. Rev. Lett. **53**, 2157 (1984).
¹³S. E. Schnatterly and R. D. Carson, Bull. Am. Phys. Soc. **30**, 416 (1985).

Generalized Brooks' formula and the electron mobility in $\text{Si}_x\text{Ge}_{1-x}$ alloys

Srinivasan Krishnamurthy and A. Sher
 SRI International, Menlo Park, California 94025

An-Ban Chen
 Auburn University, Auburn, Alabama 36830

(Received 19 March 1985; accepted for publication 7 May 1985)

A formula for alloy-scattering-limited electron mobility in semiconductors is obtained for indirect gap systems with multiple band minima. All the input parameters needed are defined explicitly. The drift mobility of $\text{Si}_x\text{Ge}_{1-x}$ which has a dip at $x \sim 0.13$ and a broader minimum at $x \sim 0.5$ is calculated by adding alloy scattering to other scattering mechanisms and correlates well with the measured Hall mobility.

The electron and hole mobilities in semiconductors are determined by the band structure and various scattering mechanisms, predominately impurity and phonon scattering. For alloys, the mobility is also affected by disorder arising from aperiodic atomic potentials and atomic positions. Many years ago, Nordheim¹ and Brooks² obtained an expression for alloy-scattering-limited electron mobilities in metals and semiconductors, respectively. Brooks' well-known formula reads

$$\mu_A = \frac{\sqrt{2\pi} e \hbar^3 N_0}{3x(1-x)m^{*5/2}} \frac{1}{(\Delta E)^2 \sqrt{KT}}, \quad (1)$$

where N_0 is the number of atoms per unit volume, m^* is a band-edge effective mass, x is the fractional concentration of one of the species, and ΔE is an energy parameter characterizing the alloy potential fluctuations. Although this formula has been widely and, to some extent, successfully used for direct gap materials,³⁻⁵ the identification of the alloy disorder parameter ΔE remains uncertain. Various suggestions have previously been made for ΔE , e.g., and band-edge discontinuity⁶ or band-gap differences.⁷ Any of these simple choices is bound to fail when one applies Eq. (1) to more complicated indirect gap systems such as $\text{Si}_x\text{Ge}_{1-x}$ alloys, where one encounters conduction-band minima transferring between the X and L points of the Brillouin zone. For example, if ΔE is taken to be the difference in corresponding band edges, then one finds that $\Delta E \sim 0.1$ eV for the X (Δ) valley and ~ 1.2 eV for the L valley. The values that fit the experiment are about half this value for L and ~ 0.5 eV for X .⁸ The purpose of this letter is to resolve the identity of ΔE for indirect gap materials.

Moreover, there is a problem with the m^* that enters Eq. (1). For direct gap alloys, the band-edge effective mass at Γ naturally enters Eq. (1). For the indirect gap alloys, the effective mass is anisotropic and hence an appropriate mass must be chosen. Previous authors^{6,7} have chosen m^* to be the effective conductivity mass m_c^* . We shall show that different masses enter for different cases.

The first unambiguous assignment for ΔE in a direct gap alloy was given by Hass *et al.*⁹ To estimate the limiting electron mobility in $\text{Hg}_x\text{Cd}_{1-x}\text{Te}$ based on a tight-binding (TB) band description, they defined ΔE to be $f_s \Delta E_s$, where f_s is the s fraction in the density of states and ΔE_s is the difference between the s atomic term values of the Hg and Cd atoms. By extending this approach to alloys with indirect gaps and

multiple bands, we show that all the uncertainties identified above are resolved. Our generalized Brooks' formula will then be applied to $\text{Si}_x\text{Ge}_{1-x}$ systems to explain their observed mobility.^{7,8}

Because Brooks' formula has never been derived explicitly in the literature, we rederive it first and then generalize it. Consider the case of a single band with an isotropic effective mass. The dc electronic conductivity based on the linear response theory⁹ is given by

$$\sigma = \int \sigma(\epsilon) \left(\frac{-d f}{d \epsilon} \right) d \epsilon, \quad (2)$$

where the energy-dependent $\sigma(\epsilon)$ in the weak alloy scattering limit is

$$\sigma(\epsilon) = (e^2/3) v^2(\epsilon) D(\epsilon) \pi(\epsilon). \quad (3)$$

$D(\epsilon)$ is the density of states (DOS) per unit volume for both spins, so $D(\epsilon) = 2N_A \rho(\epsilon)$, with $N_A = N_0/2$ being the number of unit cells per volume (for the diamond structure, half the number of atoms N_0 per unit volume) and $\rho(\epsilon)$ being the DOS per unit cell per spin. The mean square velocity $v^2(\epsilon)$ for carriers with energy ϵ is given by

$$v^2(\epsilon) = \sum_{\mathbf{k}} v(\mathbf{k})^2 \frac{\delta[\epsilon - \epsilon(\mathbf{k})]}{\rho(\epsilon)}. \quad (4)$$

The scattering lifetime for carriers with energy ϵ , $\pi(\epsilon)$, is related to the alloy broadening $\Delta(\epsilon)$ by $\pi(\epsilon) = \hbar/2\Delta(\epsilon)$, where the energy $\Delta(\epsilon)$ is the imaginary part of the self-energy in the averaged alloy Green's function. For weak scattering $\Delta(\epsilon)$ is

$$\Delta(\epsilon) = \pi x(1-x) (\Delta E)^2 \rho(\epsilon), \quad (5)$$

where in a tight binding (TB) description ΔE is the difference in the term values of the constituents. Then the mobility is $\mu_A = \sigma/ne$ with the electron density given by

$$n = 2 \int f(\epsilon) \rho(\epsilon) d \epsilon. \quad (6)$$

For a nondegenerate semiconductor, $f(\epsilon)$ is the Boltzmann distribution and $f(\epsilon) \propto e^{-(\epsilon - \epsilon_F)/kT}$. Furthermore, for a parabolic band $\epsilon(\mathbf{k}) = \hbar^2 k^2/2m^*$, $\rho(\epsilon) = (2m^*)^{3/2} \epsilon^{1/2}/4\pi^2 \hbar^3$, then all the above equations can be combined to arrive at Eq. (1).

For a real semiconductor alloy in a TB description, the alloy scattering can be characterized by two parameters ΔE_s and ΔE_p , the differences in s and p term values between two substitutional atoms. Then an effective broadening is given

by

$$\Delta(\epsilon) = (\Delta_s \rho_s + \Delta_p \rho_p) / \rho, \quad (7)$$

where ρ_s, ρ_p are partial density of states (PDOS) and Δ_s and Δ_p are similar to Eq. (5), with ρ replaced by ρ_s and ρ_p , respectively. For $\text{Hg}_{1-x}\text{Cd}_x\text{Te}$, the s disorder is predominant^{5,10} and one can neglect ΔE_p . Defining $\rho_s = f_s \rho$ (and $\rho_p = f_p \rho$), one arrives at

$$\Delta \approx \pi x(1-x)(f_s \Delta E_s)^2 \rho.$$

Thus as was pointed out by Hass *et al.*,⁵ $f_s \Delta E_s$ plays the role of ΔE in this special case where ΔE_p can be neglected.

For an alloy with a single indirect gap minimum, one has to consider both s and p contributions to the alloy broadening and the masses that enter ρ and v^2 . Again, Eqs. (2)–(6) can be combined to yield

$$\mu_A = \frac{(e\hbar^2 N_0 \sqrt{2\pi})}{[3x(1-x)m_c^* m_i^* (m_i^*)^{1/2} (kT)^{1/2} N_0 (f_s^2 \Delta E_s^2 + f_p^2 \Delta E_p^2)]}, \quad (8)$$

where m_i^* and m_c^* are respectively the longitudinal and the transverse mass at the band edge, and N_0 is the number of equivalent minima, e.g., 6 for Si. The conductivity mass m_c^* comes from averaging v^2 in Eq. (2) and is given by $3(2/m_i^* + 1/m_t^*)^{-1}$. Equation (8) clearly identifies the masses and the energy parameter that enter Brooks' formula.

Next we consider a still more complicated case where the contribution to the mobility comes from more than one band. For example, in $\text{Si}_x\text{Ge}_{1-x}$ the X and L minima cross near $x = 0.15$.¹¹ There are now two contributions to the net conductivity, so $\sigma = \Sigma \sigma_i$, where i is X or L . The quantities $v^2(\epsilon)$, $D_i(\epsilon)$, and $N_i(\epsilon)$ now take different values for different bands. The structure of $\tau_i(\epsilon)$ requires more careful consideration. The complication comes from the fact that the effective broadening Δ is still given by Eq. (7), but ρ_s, ρ_p , and ρ contain contributions from both the bands. The proper expressions are $\rho = \Sigma_i \rho_i N_i'$ and $\rho_a = \Sigma_i f_{ai} N_i' \rho_i$, where $i = X$ or L , $\alpha = s$ or p , and $N_i^X = 6$, $N_i^L = 4$. The equation for Δ is

$$\Delta(\epsilon) = \pi x(1-x) \sum_i \left(\sum_j f_{aj} N_j' \rho_j(\epsilon) \Delta E_{aj} \right)^2 / \left(\sum_i \rho_i(\epsilon) N_i' \right). \quad (9)$$

The mobility associated with the i th band is defined as $\mu_i = \sigma_i / (n_i e)$, then

$$\mu_i^A = \frac{\pi e \hbar^2 N_0}{3x(1-x) [m_c^* m_i^* (2m_i^*)^{1/2}]} I_i, \quad (10)$$

$$I_i = \int_0^\infty \frac{\epsilon \rho_i(\epsilon) \left(\sum_j N_j' \rho_j(\epsilon) \right) e^{-\epsilon/kT}}{\sum_i \left(\sum_j f_{aj} N_j' \rho_j(\epsilon) \Delta E_{aj} \right)^2} d\epsilon / \int_0^\infty \epsilon^{1/2} e^{-\epsilon/kT} d\epsilon. \quad (11)$$

Thus, the generalized formula no longer has the explicit x and T dependences of the original Brooks' form. However, all the quantities needed—the masses, the scattering parameters ΔE_{ai} , the band gaps, and the fractions f_{ai} —can be evaluated theoretically without resorting to experimentally fitted parameters. To demonstrate, we shall apply Eq. (10) to $\text{Si}_x\text{Ge}_{1-x}$. The band quantities are obtained from our CPA calculation.¹¹ We found that the effective masses vary weak-

TABLE I. Calculation parameters.

Parameter	Si, Ge, $\text{Si}_x\text{Ge}_{1-x}$ systems
$m_c^*(X)$	0.97 m_0
$m_c^*(L)$	0.19 m_0
$m_t^*(X)$	1.64 m_0
$m_t^*(L)$	0.082 m_0
$E_g^X(x)$	0.8941 + 0.0421x + 0.1691x ²
$E_g^L(x)$	0.7596 + 1.0860x + 0.3306x ²
$f_{sX}(x)$	0.333 + 0.05x (0 < x < 0.3)
	0.339 + 0.03x (0.3 < x < 1.0)
$f_{sL}(x)$	0.632 + 0.13x

ly with the concentration, so m_i^* and m_c^* are assumed to be constant and assigned the values 0.97 and 0.19 for the X minima and 1.64 and 0.082 for the L minima, respectively. The calculated energy gaps for the X (Δ) follows the functional form $E_g^X(x) = a + bx + cx^2$ and for L is given by $E_g^L(x) = A + Bx + Cx^2$. All the parameters of our calculations are listed in Table I.

To correlate the calculation with the measured mobilities, we need to have an estimate of scattering rates $1/\tau_0$ due to impurities and phonons. A crude approximation is to assume $1/\tau_0$ for a given valley to be the same as the appropriate constituent's values and add to it the alloy scattering rate $1/\tau_A$. Then the average mobility and the mobility from the i th minimum in the alloy are

$$\mu = \sum_i n_i \mu_i / \sum_i n_i, \quad (\mu_i)^{-1} = (\mu_i^0)^{-1} + (\mu_i^A)^{-1}, \quad (12)$$

μ_i^A is given by Eq. (10) and μ_i^0 are the measured drift mobilities for Si or Ge.¹² The drift mobility, calculated from Eq. (12), is plotted as a function of alloy concentration x in Fig. 1.

For $x < 0.05$ and $x > 0.20$, the energy difference between the X and L edges is large enough so there is a negligible contribution to the mobility from the higher minima. In the $\text{Si}_x\text{Ge}_{1-x}$ system, the s scattering is predominant. Because

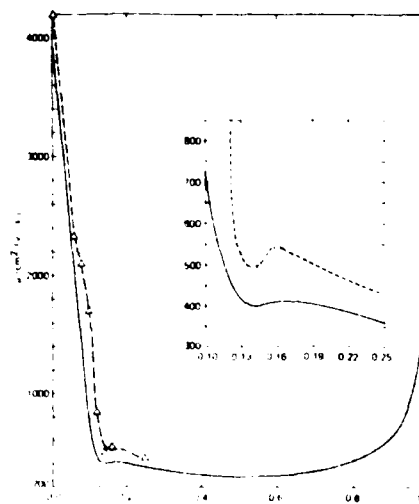


FIG. 1. Calculated (solid line) electron drift mobility and the experimental Hall mobility (dashed line) from Refs. 6 and 8 are plotted as a function of alloy concentration.

the L edges have a larger s content, alloy scattering reduces the average mobility substantially for small x . Even though the s content is almost the same for all $x > 0.20$ at the X edge, the mobility still decreases to $x \approx 0.5$ as shown in Fig. 1 because of the $x(1-x)$ term in Eq. (10).

An interesting feature is obtained for the compositions $0.13 < x < 0.18$. The average mobility attains a local minimum near $x = 0.14$ and a smaller maximum at $x = 0.17$. This feature occurs because of the X to L crossover.¹¹ For $x < 0.14$, the major contribution to μ comes from L minima. Near $x = 0.14$, the density of states increases because the X and L minima merge. So the alloy scattering increases there and the average mobility decreases. For $x > 0.14$, the X bands have the lower minima. As the s content is small at the X minima, the reduced alloy scattering increases the average mobility. For larger values of x , the $x(1-x)$ term takes over and the mobility varies as shown. The values of measured Hall mobility in $\text{Si}_x\text{Ge}_{1-x}$ systems are also plotted in Fig. 1. The interesting feature near $x = 0.14$ is clearly seen. Since the experimental drift mobility μ_D for $\text{Si}_x\text{Ge}_{1-x}$ is not available and the generalization of Eq. (10) to Hall mobility μ_H is less clear, we present the calculated μ_D and experimental μ_H (Ref. 7,8) here. While we do not expect quantitative agreement, because μ_H/μ_D can range from 1 to 2,^{13,14} we do expect them to display the same qualitative x dependence. It is rewarding to note the similarity in the trend in Fig. 1. Previous authors explained the dip in the mobility curve by including intervalley scattering with an arbitrary adjustable coupling constant.⁶ Our calculations automatically include that portion of intervalley scattering that results from alloy disorder with a coupling constant set by the atomic proper-

ties of the constituents. However, the addition of intervalley scattering mediated by phonons and impurities is expected to increase the dip near crossover.

In summary, an expression for alloy-scattering-limited charge carrier mobilities is derived for indirect gap alloys with multiple bands. This expression reduces to Brooks' formula for direct gap alloys. The quantities m^* and ΔE can be calculated exactly. Alloy scattering accounts for the observed mobility features in the $\text{Si}_x\text{Ge}_{1-x}$ alloy, including the anomaly near the L to $X(\Delta)$ crossover.

A.-B. would like to thank Professor W. E. Spicer for his hospitality at Stanford University. This work was supported in part by DARPA contract MDA 903-83-C-0108 and grant AFOSR-84-0282.

¹L. Nordheim, *Ann. Phys.* **9**, 607 (1931); **9**, 641 (1931).

²H. Brooks (unpublished). A discussion of this formula can be found, for example, in L. Makowski and M. Glicksman, *J. Phys. Chem. Solids* **34**, 487 (1973).

³A. Chandra and L. F. Eastman, *J. Appl. Phys.* **51**, 2669 (1980).

⁴D. Chattopadhyay and B. R. Nag, *Phys. Rev. B* **12**, 5676 (1975).

⁵K. C. Hass, H. Ehrenreich, and B. Velicky, *Phys. Rev. B* **27**, 1088 (1983).

⁶J. W. Harrison and J. R. Hauser, *J. Appl. Phys.* **47**, 292 (1976).

⁷M. Glicksman, *Phys. Rev.* **111**, 125 (1958).

⁸M. Glicksman, *Phys. Rev.* **100**, 1146 (1955).

⁹A.-B. Chen, G. Weisz, and A. Sher, *Phys. Rev. B* **5**, 2897 (1972). See Eq. (134).

¹⁰D. S. Montgomery, *J. Phys. C* **16**, 2923 (1983).

¹¹S. Krishnamurthy, A.-B. Chen, and A. Sher (unpublished).

¹²S. M. Sze, *Physics of Semiconductors*, 2nd ed. (Wiley-Interscience, New York, 1981).

¹³V. A. Johnson and K. L. Horowitz, *Phys. Rev.* **79**, 176 (1950); **79**, 409 (1950).

¹⁴H. Jones, *Phys. Rev.* **81**, 149 (1951).

SEMICONDUCTOR ALLOYS: LOCAL BOND LENGTHS, MIXING ENTHALPIES, AND MICROCLUSTERS

A.B. CHEN* AND A. SHER†

*Physics Department, Auburn University, AL 36849

†SRI International, Menlo Park, CA 94025

ABSTRACT

Several recent theoretical studies of the local structure of semiconductor alloys are summarized. First, dilute limit calculations of local bond lengths and mixing enthalpies are discussed. These calculations include effects due to both bond length and bond-angle distortions, as well as local chemical rearrangements. Then, a new statistical theory of concentrated alloys is described. Deviations from random alloy distributions (microclusters) are predicted.

INTRODUCTION

This paper summarizes our recent theoretical studies directed toward understanding the microscopic structures of pseudo-binary semiconductor alloys $A_xB_{1-x}C$. We first present a detailed calculation of the local bond length relaxation in the dilute limit $x \rightarrow 0$, i.e. the case where an A atom is substituted for a B atom in a BC compound. The mixing enthalpy parameter Ω is found to be related to small excess substitution energies. These excess energies are calculated directly through a minimization procedure. Thus, the accuracy of the predicted Ω is not limited by trying to find small differences between large numbers. The theory is then generalized to concentrated alloys using statistics based on combinations of tetrahedral clusters of five atoms. Our results predict that microclustering occurs in a majority of alloys. We conclude by identifying systematic correlations between the theory and several experiments.

Before discussing the calculation, it is useful to provide some background about the structure of these alloys. It was customary to assume that these alloys have two sublattices in which the C atoms occupy one sublattice, and A and B atoms are randomly distributed on the other. This picture, referred to as the virtual crystal approximation (VCA), implies that the nearest-neighbor (nn) bond lengths in the alloy are the concentration weighed average values, i.e. $d_{AC} = d_{BC} = \bar{d} = x d_{AC}^{(0)} + (1-x) d_{BC}^{(0)}$ where the values with a superscript (0) denote the pure-crystal values. On the other hand, according to Pauling's covalent radii approximation (CRA), the local bond lengths retain their respective pure-crystal values, i.e. $d_{AC} = d_{AC}^{(0)}$ and $d_{BC} = d_{BC}^{(0)}$.

If we define $\delta_0 = (\bar{d} - d_{AC}^{(0)}) / \bar{d}$ and $\delta = (\bar{d} - d_{AC}) / \bar{d}$, then the ratio δ/δ_0 in VCA is zero, but in CRA it is 1. However, Mikkelsen and Boyce¹⁾ found from their EXAFS experiment on $Ga_xIn_{1-x}As$ that the nn bond lengths do not fit either VCA or CRA. Instead, they found the value of δ/δ_0 to be close to 3/4. Since then, similar experiments have been done for a number of zinc-blende pseudo-binary alloys,¹⁾ and the 3/4 rule appears to be quite general.

DILUTE LIMIT

The dilute limit is the easiest case but is still not trivial. Its solution provides both end-point results ($x = 0$ and 1), as well as insight into the extension to the concentrated alloy case. A complete description of this case is being reported elsewhere; here we summarize the essential results. The substitution energy Δ_s for an A atom replacing a B atom in a BC compound is calculated and minimized to find the relaxed configuration. Δ_s can be written as $\Delta_s = 4(\Delta E_b + \Delta E_s + \Delta E_{ch})$, where ΔE_b is the binding energy difference between the AC and BC compounds, ΔE_s is the strain energy, and ΔE_{ch} is a chemical energy shift. All ΔE 's are energies per bond. Then, $\Delta E = \Delta E_s + \Delta E_{ch}$ is the excess energy per bond for the impurity substitution. ΔE_s is calculated by dividing the crystal into two regions. Outside R (which is the distance of the second-shell atoms to the impurity), the distorted crystal is treated as an elastic continuum with a radial displacement field which is inversely proportional to the square of the radial distance, so $\Delta E_s^{(out)} = 1/4RCu^2$, where C is an effective shear coefficient,

$$C = \pi (1.6 (C_{11} - C_{12}) + 4.8 C_{44}), \quad (1)$$

and u is the magnitude of the displacement at R. Inside R, the strain energy $\Delta_s^{(in)}$ is treated with a valence force field (VFF).⁽²⁾ Finally, the chemical energy shift ΔE_{ch} is calculated from Harrison's model and arises from changes in the metalization energies caused by different bond lengths $\Delta d \equiv d_{BC} - d_{AC}$ and covalent energies $\Delta V_3 \equiv V_3(AC) - V_3(BC)$. Note that $\delta_0 = (d_{BC}^{(0)} - d_{AC}^{(0)}) / d_{BC}^{(0)}$ and $\delta = (d_{BC}^{(0)} - d_{AC}) / d_{BC}^{(0)}$ in this dilute limit, so the excess energy ΔE can be expanded up to second order in δ , u , and ΔV_3 . For a given pair A and B, ΔE is an explicit function of δ and u . Minimization of ΔE with respect to δ and u leads to the equilibrium local bond length d_{AC} and energy ΔE . Then, ΔE is used to estimate the mixing enthalpy parameter Ω in the mixing enthalpy $\Delta H = x(1-x)\Omega$ by

$$\Omega = 2 (\Delta E (A \text{ in } BC) + \Delta E (B \text{ in } AC)). \quad (2)$$

A systematic comparison with other models based on strain energy alone shows that an increase of the range of the fixed boundary R increases the relaxation of d_{AC} , i.e., it causes δ/δ_0 to increase. The inclusion of the bond angle restoring force, on the other hand, reduces the relaxation. It turns out that a delicate cancellation of these two effects causes a simple spring model pointed out by Shih et al. (SSHS)⁽³⁾ to yield accurate results. In this model $\delta = \delta_0 / (1 + 1/3 \alpha/\alpha_1)$, where α and α_1 are the bond-stretching force constants for the host (BC) and the impurity (AC) crystals. With $\alpha \approx \alpha_1$, this model predicts $\delta = 3/4\delta_0$ for a zinc-blende alloy. Although our full perturbation theory (FPT) and the VFF model of Martin and Zunger (MZ)⁽⁴⁾ predict d_{AC} with an average absolute deviation comparable to the experimental uncertainty of 0.01 Å, the simple spring model is even better.

We note that while in our theory, MZ and SSHS, the Ω values are directly calculated without any adjustable parameters, our theory and SSHS agree with the experiment as well or even slightly better than the one-parameter theories.^{5,6} Although our theory predicts a negative Ω value for all three (Ga, Al) alloys, the magnitude ($|\Omega| = 0.17$ kcal/mole) is too small to account for the ordering of $\text{Ga}_x\text{Al}_{1-x}\text{As}$ grown at 600 to 700°C found recently.⁷ The calculated Ω values also provide guidance in separating miscible from immiscible alloys. In a random alloy, the criterion for alloy

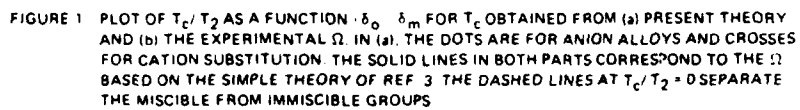
mixing for all x is $T > T_c$, where the critical temperature T is given by $T_c = \Omega/2R_g$ with R_g being the universal gas constant. Figure 1 is a plot of T_c/T_2 against $|\delta_0|/|\delta_m|$, where T_2 is the lower of the two constituent's melting temperatures, and $\delta_m = 1.63x_m$ with x_m being the ratio of rms bond length amplitude fluctuation to the bond length at T_2 . The simple spring model gives $T_c/T_2 = (\delta_0/\delta_m)^2$ as indicated by the solid curves.

There is an empirical rule stating that a miscibility gap will occur if $|\delta_0|$ between two alloy components exceeds 7.5%. However, if T_c/T_2 is plotted against $|\delta_0|$, the simple spring model would not exhibit a smooth simple quadratic curve, and our theoretical points would be much more scattered. This suggests that $|\delta_0|/|\delta_m| > 1$ is a better criterion than $|\delta_0| > 0.075$. Figure 2 also clearly shows the chemical effects, namely negative and positive chemical energies ΔE_{ch} for cation and anion substitutions respectively. The full theory and the experiments correlate within the experimental uncertainties. The simple SSHS model clearly is an excellent universal representation. However, T_c/T_2 varies faster than quadratically for larger $|\delta_0/\delta_m|$ values, as born out from both the experimental data and the full theory.

CONCENTRATED ALLOYS

Turn now to the concentrated alloy case. First, an improved statistical model is required. We have extended regular solution theory based on pair energies to one for five-atom clusters. For an $A_mB_{4-m}C$ alloy, the building blocks are clusters of $A(m)B(4-m)C$, where m ranges from 0 to 4. For a given alloy concentration x and for a given set of energies ϵ_m associated with these clusters, we have derived expressions for the cluster population distribution $x_m \equiv \bar{n}_m / N$, where N is the total number of unit cells and \bar{n}_m is the averaged number of cells with $A(m)B(4-m)C$ clusters. The partition function Z is obtained using a steepest descents argument which then yields the mixing Helmholtz free energy ΔF . The result reduces to Guggenheim's tetrahedron case⁽⁷⁾ if pair potentials (for the second-neighbors) are assumed. Another major difference is that we only need to solve a single quartic equation, while Guggenheim needed to solve four simultaneous quartic equations.

The key to the problem, however, lies in the calculation of the energies ϵ_m . If one assumes that the size of the tetrahedra for all m -clusters at a given alloy concentration takes on the corresponding VCA values but allows the central C atom to relax, then the energies as functions of x behave like those shown in Figure 2(a). There are at least two major flaws in this result. First, the energies are too large and would correspond to Ω values many times the experimental values. Second, at $x = 0.75, 0.5$, and 0.2 , these energies imply compound formation for $A_3B_1C_4$, $A_2B_2C_4$, and $A_1B_3C_4$, respectively, which is opposite to the known tendency for spinodal decomposition of $Ga_{1-x}In_xAs$ at low T . However, if the local cell volume of each cluster is allowed to be in mechanical equilibrium with a continuous medium with an effective shear coefficient $\bar{C} = xC_A^{(0)} + (1-x)C_B^{(0)}$, where the C value for the pure material is given by Eq. (1), then, the corresponding energies ϵ_m as a function of x are given in Figure 2(b), which now yields a reasonable value of mixing enthalpy and correctly predicts the tendency toward spinodal decomposition at low temperature. With this set of energies, one can then calculate the cluster distribution x_m , and compare them with the corresponding values for a random alloy, i.e. $x_m^{(0)} = (4_m x^m (1-x)^{4-m})$. Figure 3 shows the deviation from randomness $\Delta x_m = x_m - x_m^{(0)}$ as a function of x for four arbitrarily chosen growth



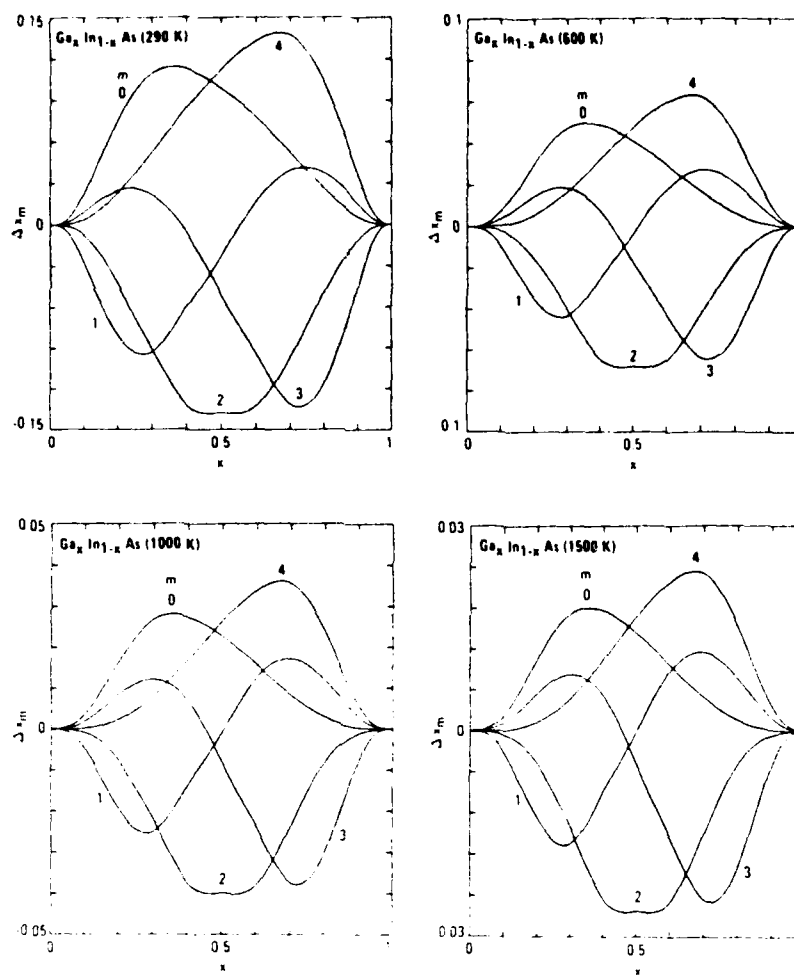


FIGURE 3 DEVIATIONS FROM RANDOM DISTRIBUTIONS FOR THE FIVE CLUSTERS AT SEVERAL GROWTH TEMPERATURES

Band structures of $\text{Si}_x\text{Ge}_{1-x}$ alloys

Srinivasan Krishnamurthy and A. Sher

SRI International, Menlo Park, California 94025

and

A.-B. Chen

Physics Department, Auburn University, Auburn, Alabama 36849

ABSTRACT

Starting from realistic band structures of the constituent materials, the electronic structure of $\text{Si}_x\text{Ge}_{1-x}$ alloys are obtained in the coherent potential approximation (CPA). Various quantities, including the bowing parameter of the fundamental gap and the energies of several optical gaps, the masses, and the linewidths of the E_0 and E_1 transitions, are calculated on the basis of both diagonal and off-diagonal CPA. All of the band-energy and line-width predictions are in good agreement with experiments. Furthermore, the theory yields alloy-scattering-limited electron-drift mobility in qualitative agreement with experimental results.

I. INTRODUCTION

Semiconductor alloys offer the freedom to design material properties by choosing appropriate alloy constituents. In some cases, the physical properties of the alloys can be quite different from those of the constituents.⁽¹⁻⁴⁾ In recent years, there has been a renewed interest in $\text{Si}_x\text{Ge}_{1-x}$ alloys⁽⁵⁾ and superlattices.⁽⁵⁻¹⁰⁾ Because silicon is the most technologically advanced semiconductor, the results on SiGe systems have many potential applications.

The lattice constants of silicon and germanium differ by $\sim 4\%$. Hence, the strain introduced in the formation of $\text{Si}_x\text{Ge}_{1-x}$ alloys can affect the band structure⁽¹⁰⁾ and the transport properties.⁽⁸⁾ Prior authors used virtual crystal approximation (VCA)^(11,12) and coherent potential approximation (CPA)⁽¹³⁾ to study the band structure and related properties. Either because of less accurate band structures of the constituent materials, or because of the approximations involved in the alloy formalism, these calculations predicted only trends of specific quantities, not quantitatively accurate results. Because the s-state site potentials (ϵ_s) for silicon and germanium differ by approximately 1.5 eV, VCA cannot accurately describe effective masses and other finer details of the band structure. Because of the use of poor basis functions, earlier CPA work⁽¹³⁾ predicted alloy broadening of conduction band states substantially differing from experiment. The purpose of this paper is to correct these flaws and treat transport phenomena.

Because of a substantial difference between the site potentials and lattice constants of silicon and germanium, we incorporated both chemical and structural disorder in the calculation of the electronic structure of $\text{Si}_x\text{Ge}_{1-x}$ alloys. Thus, both diagonal and off-diagonal CPA are included in the predicted band structure and related quantities. Parts of the band structure have been used to study the Si-2p core-exciton⁽¹⁴⁾ and the alloy mobilities.⁽¹⁵⁾ A comprehensive report of the calculations and results is presented here.

The rest of the paper is arranged as follows. The detailed procedure of fitting silicon and germanium band structures is given in Section II. The VCA, CPA, and off-diagonal CPA calculations are described in Section III. The results and interpretation of the alloy band structures and mobility are given in Section IV.

II. BAND STRUCTURE BASIS

In order to derive an accurate alloy band structure, one must start from a realistic band structure of the constituent materials. Chen and Sher have developed a method⁽¹⁶⁾ following a prescription of Kane⁽¹⁷⁾ and Chadi⁽¹⁸⁾ that includes all long-range interactions, and then fine tuned the band structure with an adjustable local Hamiltonian. Because the details have already been published,^(16,19) the underlying method will be presented here in brief.

Gaussian orbitals of the type α (α can be s, p_x , p_y , or p_z) for each sublattice in a cell are used to construct the corresponding Bloch basis. In this basis set, the overlap matrix and the Hamiltonian derived from empirical pseudopotentials can be calculated.^(17,18) It is possible to cast the problem in a basis set of Gaussian orbitals in which, in crystal units (cu), the same exponential factors apply for all III-V compounds.⁽¹⁹⁾ In this universal basis, the overlap matrix and the kinetic energy matrix are same for all III-V compounds. Then, by a unitary transformation, the basis set is orthonormalized.⁽²⁰⁾ The Hamiltonian in this new basis set is denoted $H_0(\vec{k})$. The band structure resulting from this method reproduces the results of elaborate band structure calculations within a few percent throughout the Brillouin zone (BZ). To establish accurately certain important band structure features adjacent to the gap, an extra small 8×8

Hamiltonian matrix $H_1(\vec{k})$ is added to $H_0(\vec{k})$. This $H_1(\vec{k})$ has the form of a tight-binding (TB) Hamiltonian, in which only the nearest neighbor interactions are included, and stimulates the effect of nonlocal pseudopotentials and an expanded orbital set. The total Hamiltonian, $H(\vec{k})$, in this orthonormalized basis set is diagonalized to obtain the band energies and the corresponding wave functions.

Following this procedure with the same exponential factor $\beta = 0.26$ in the Gaussian orbitals for both silicon and germanium, the matrix $H_0(\vec{k})$ is obtained. For silicon and germanium, H_1 contains 6 adjustable parameters: namely, the corrections to the term values Δ_s and Δ_p and to the nearest-neighbor interactions V_{ss} , V_{sp} , V_{xx} , and V_{xy} . The values of Δ_s , Δ_p , V_{ss} , and V_{xx} are determined from fitting the three experimental energy gaps⁽²¹⁻²⁸⁾ at $\Gamma(\vec{k} = 0)$: $\Gamma_2' - \Gamma_1$, $\Gamma_{15} - \Gamma_{25'}$, and $\Gamma_2' - \Gamma_{25'}$, and the photoelectric threshold (PT) values -5.07 and -4.80 eV for silicon and germanium respectively.⁽²⁹⁾ The remaining parameters V_{sp} and V_{xy} are obtained from the experimental values^(21-28,30) of the gaps $X_{1c} - X_{1v}$ and $L_{1c} - L_{3v}$. Some adjustments in these input quantities are made to obtain an overall good band structure with more accurate effective masses. Table I lists the empirical pseudopotential form factors and the parameters used to obtain the band structure. The calculated band structures and experimental values are given in Table II. From Table II, one can see that an excellent fit to the silicon and germanium band structure is obtained: All the calculated values lie within the experimental uncertainties. The optical difference between L_{1c} and L_{3v} , $\Gamma_{25'}$ and Γ_{15} are in excellent agreement with the known optical transition values.

Although the calculated effective transverse masses agree very well with experiment, the effective longitudinal mass for germanium is less than the experimental value. This is due mainly to our attempt to have a common β and the choice of local pseudopotentials, causing $H_0(\vec{k})$ to be the same in crystal units (cu) for both germanium and

silicon. Because of the common $H_0(\vec{k})$, the alloy disorder is contained in these adjusted parameters. This H_0 would also be useful for the interface and superlattice(30) problems. If we grant ourselves the freedom to adjust V_{xy} , longitudinal effective mass in germanium can be fitted to the experimental value. When V_{xy} is changed, the L_{1c} , L_{3c} will also change. We have chosen not to do this because little is gained for the extra complexity. For an indirect gap semiconductor, the important effective mass used in transport studies is the conductivity mass, $3 \left(1/m_{el}^* + 2/m_{et}^* \right)^{-1}$. Because $m_{el}^* \gg m_{et}^*$ in germanium, m_c^* will not be much different if a less accurate value of m_{el}^* is used. Moreover, the Si_xGe_{1-x} alloys which have potential device applications are in the silicon-rich region, where the effective mass at the L edge is not expected to affect the further studies.

It is important to note that an excellent fit to the experimental values can be obtained with only seven adjustable parameters (β , Δ_s , Δ_p , V_{ss} , V_{sp} , V_{xx} , V_{xy}), with β being universal in cu. The calculated band structure of silicon and germanium are shown in Fig. 1(a) and 1(b) respectively. The characteristic indirect gaps are clearly seen. These band structures compare favorably with the best results available, and, in contrast with those obtained in the usual empirical TB approaches, produce good conduction bands.

III. ALLOY CALCULATION

A. VCA

Because we have the same $H_0(\vec{k})$ matrix for both silicon and germanium, it is only the H_1 matrices of the constituents in scaled VCA which distinguishes them. In this approximation, the diagonal elements of the alloy Hamiltonian $\bar{H}(\vec{k})$ are simply the concentration-weighted average of the corresponding elements of the pure silicon and germanium Hamiltonians, whereas the off-diagonal elements of $\bar{H}(\vec{k})$ are obtained by assuming a $1/d^2$ dependence. $\bar{H}(\vec{k})$ can be diagonalized to obtain the VCA band structure for various concentrations, x . The VCA band structures for $x = 0.1$ and 0.5 are shown in Fig. 1(c) and 1(d) respectively.

B. Diagonal CPA

An earlier work on CPA band structure of SiGe alloys⁽¹³⁾ is based on a local but energy-dependent pseudopotential approximation. While the value of the scattering potential parameter was 1.49 eV, close to our value, the calculation predicted too-large linewidths in the E_0 spectrum and essentially no effect on the electron mobility. With the availability of a set of good basis functions and constituent band structures, more realistic band structures of the alloy can be obtained.

In the current model, we have a TB Hamiltonian, which contains matrix elements to all ranges. The simplest alloy model is to assume that the important disorder resides only in the diagonal matrix elements, ϵ_s and ϵ_p . In our model, the ϵ_s^{Si} and ϵ_s^{Ge} differ by

1.46 eV, whereas ϵ_p^{Si} and ϵ_p^{Ge} differ by 0.21 eV. For the present, we neglect the disorder in the off-diagonal element. Mathematically, we have

$$H_{\text{alloy}} = H + \sum_{\vec{T}} V_{\vec{T}} \quad , \quad (1)$$

where \vec{T} is a fcc lattice vector identifying a site, and $V_{\vec{T}}$ is the 8x8 diagonal matrix with elements $U_s = \epsilon_s - \bar{\epsilon}_s$, $U_p = \epsilon_p - \bar{\epsilon}_p$ in the orthonormal local orbitals $|\vec{T}j\alpha\rangle$; j denotes the two atoms in the unit cell labeled \vec{T} , α represents s or p symmetry, and $\bar{\epsilon}_s$ and $\bar{\epsilon}_p$ are the concentration-weighted average values of s and p silicon and germanium term value energies.

The one particle alloy Green's function is defined as

$$G_{\text{alloy}}(Z) = \frac{1}{Z - H_{\text{alloy}}} \quad (2)$$

We are after the configuration average of this Green's function, which, in effective medium theory, is replaced by an effective Green's function G ,

$$G(Z) = \frac{1}{Z - H - \Sigma(Z)} \quad , \quad (3)$$

where Σ is the self energy. In CPA, we can now write $\Sigma = \sum_I (\Sigma_I)$, with Σ_I being an 8x8 matrix in the basis $|\bar{l}j\alpha\rangle$ having the form

$$\Sigma = \begin{pmatrix} A & 0 \\ 0 & A \end{pmatrix} , \quad (4)$$

where

$$A = \begin{pmatrix} \Sigma_s & 0 & 0 & 0 \\ 0 & \Sigma_p & 0 & 0 \\ 0 & 0 & \Sigma_p & 0 \\ 0 & 0 & 0 & \Sigma_s \end{pmatrix} .$$

Here Σ_s and Σ_p are the s and p parts of the self energy. The Σ_s and Σ_p are determined from the conditions that the average atomic t-matrix with respect to the CPA Green's function G is zero. With our ansatz for Σ , the matrix equation $\langle t \rangle = 0$ reduces to two coupled equations $\langle t_s \rangle = 0$ and $\langle t_p \rangle = 0$, where the average is the concentration-weighted average $\langle Q \rangle = xQ^{\text{Si}} + yQ^{\text{Ge}}$, and the t is defined as

$$t_\alpha^\beta = (U_\alpha^\beta - \Sigma_\alpha) [1 - F_\alpha (U_\alpha^\beta - \Sigma_\alpha)]^{-1}$$

$$(\alpha = s \text{ or } p, \beta = \text{Si or Ge}) . \quad (5)$$

In the above expression, F_α is the diagonal matrix element of G in the local basis $F_\alpha(Z) \equiv \langle \bar{l}j\alpha | G(Z) | \bar{l}j\alpha \rangle$. Σ_s and Σ_p are coupled because F_s and F_p each contain both Σ_s and Σ_p .

An iterative average-t-matrix (IATA) procedure⁽¹⁹⁾ is employed to solve the CPA equation. This procedure improves Σ_a upon a guessed solution Σ_a^o through the following equations

$$\Sigma_s = \Sigma_s^o + \langle t_s^o \rangle [1 + F_s^o \langle t_s^o \rangle]^{-1} ,$$

$$\Sigma_p = \Sigma_p^o + \langle t_p^o \rangle [1 + F_p^o \langle t_p^o \rangle]^{-1} , \quad (6)$$

where $\langle t_s^o \rangle$ and F_s^o are similar to those in Eq. (5) except that Σ_a^o now replaces Σ_a . The most time-consuming calculation is then the computation of the local Green's functions F_s^o and F_p^o , given by the BZ summation; e.g.

$$F_s^o(Z) = \frac{1}{N} \sum_{\vec{k}} \left(\frac{1}{Z - H(\vec{k}) - \Sigma_s^o} \right)_{11} ,$$

where the inverse of an 8x8 matrix is involved for every \vec{k} . This can be simplified by observing that Σ_a^o has the same form as Σ in Eqs. (4) and (5) and that the 4x4 A matrix can be written as $A = \Sigma_p \tilde{I} + (\Sigma_s - \Sigma_p)J$, where \tilde{I} is the identity matrix and

$$J = \begin{pmatrix} 1 & 0 & 0 & 0 \\ 0 & 0 & 0 & 0 \\ 0 & 0 & 0 & 0 \\ 0 & 0 & 0 & 0 \end{pmatrix} .$$

Defining the matrix

$$\sigma = (\Sigma_s^o - \Sigma_p^o) \begin{pmatrix} J & 0 \\ 0 & J \end{pmatrix}$$

$F_s^o(Z)$ and $F_p^o(Z)$ can now be calculated from

$$F_s^o(Z) = \frac{1}{N} \sum_{\vec{k}} g_{11}(\vec{k}, Z) \quad ,$$

$$F_p^o(Z) = \frac{1}{3N} \sum_{\vec{k}} (g_{22}(\vec{k}, Z) + g_{33}(\vec{k}, Z) + g_{44}(\vec{k}, Z)) \quad , \quad (7)$$

where

$$g = g^o + g^o(1 - \sigma g^o)^{-1} \quad . \quad (8)$$

with

$$g_{\alpha\beta}^{(o)}(\vec{k}, Z) = \sum_n \frac{U_{\alpha n}(\vec{k}) U_{\beta n}^*(\vec{k})}{Z - \epsilon_n(\vec{k}) - \Sigma_p^o} \quad . \quad (9)$$

In Eq. (9), $\epsilon_n(\vec{k})$ is the band energy in VCA and $\{U_{\alpha,n}(\vec{k})\}$ satisfy the following Eigen equation:

$$\sum_{\beta} H_{\alpha,\beta}(\vec{k}) U_{\beta,n}(\vec{k}) = \epsilon_n(\vec{k}) U_{\alpha,n}(\vec{k}) .$$

Because the σ matrix has only two nonzero elements, the matrix inversion in Eq. (8) is obtained analytically.

A substantial reduction in computer time is made possible by using an analytical continuation method.⁽³²⁾ In this method, Σ_s and Σ_p are calculated as a function complex Z , and then, using the analytical properties of the self energy and Green's functions, they are interpolated for real Z . Because the functions Σ_s , Σ_p , and G are smooth for complex Z , the CPA iterations and BZ integrations can be carried out with substantially less computer time.

For the concentration $x = 0.10$ and $x = 0.50$, the L and X(Δ) gap respectively are preferred. The L to X(Δ) crossover takes place near $x \approx 0.15$. The CPA correction to L and X edges at $x = 0.10$, 0.15, and 0.50 should be good enough to study the quantitative variation of band gap in $\text{Si}_x\text{Ge}_{1-x}$ alloys. Hence, the calculations are carried out for these three cases. In addition, because the experimental results are available for $x = 0.109$, CPA calculations are also done here for comparison. As expected, Σ_s is much larger than Σ_p for all the cases. The self energy as a function of energy is plotted in Fig. 2 for an $x = 0.50$ alloy.

C. Off-Diagonal CPA

As mentioned earlier, silicon and germanium differ in their lattice constant by $\sim 4\%$. In order to include the effect of the structural disorder, the CPA calculation is repeated next with off-diagonal (OD) disorder included. By an application of the molecular coherent potential approximation (MCPA)⁽³³⁾, Hass et al. included OD disorder in the CPA calculation of $A'_x A'^{1-x} B$ semiconductor alloys.⁽³⁴⁾ Assuming that B atoms occupy the sites of an ordered zinc-blende virtual lattice, they modeled the dominant structural effect as the difference in $A'-B$ and $A'^{1-x}-B$ hopping matrix elements. Hence, the chemical and structural disorder effects are treated as random variations of ϵ^A , V_1^A , V_2^{AB} , where the symbols have their usual meaning.⁽³⁵⁾

The extension of the method to $Si_x Ge_{1-x}$ alloys is not straightforward, mainly because silicon and germanium can occupy both sublattices; hence, there can be no ordered virtual lattice in this case. If we choose the tetrahedral unit cell as the molecular unit for MCPA, we see that the disorder is not cell diagonal. However, by choosing an appropriate basis set, we can make the intercell interaction be the highest order effect. We start with a hybrid basis $|\bar{h}\rangle_i$ obtained from the sp^3 hybrid orbitals.⁽³⁵⁾ The hybrids 1 through 4 ($i = 1-4$) are obtained from orbitals centered on a sublattice I-site, and the states 5 through 8 ($i = 5-8$) are those from the orbitals located at the four nearest neighbor sites on sublattice II. The Bloch basis states, corresponding to A_1 , T_2 symmetries, $|k\rangle_i$ located on an I-site ($i = 1-4$) and II-site ($i = 5-8$) are obtained from the corresponding hybrid states given by the relation

$$|\bar{T}\rangle_i = \sum_{j=1}^8 C_{ij} |\bar{h}\rangle_j, \quad (10)$$

where

$$C = \begin{pmatrix} c_1 & 0 \\ 0 & c_1 \end{pmatrix}$$

and

$$c_1 = \frac{1}{2} \begin{pmatrix} 1 & 1 & 1 & 1 \\ 1 & 1 & -1 & -1 \\ 1 & 1 & 1 & -1 \\ 1 & 1 & -1 & 1 \end{pmatrix}$$

An explicit definition of these orbitals can be found in Ref (20). In this new basis, the self energy Σ at the given site takes the form

$$\Sigma = \begin{pmatrix} \sigma_0 & \sigma_2 \\ \sigma_2 & \sigma_0' \end{pmatrix} \quad (11)$$

where

$$\sigma_0 = \begin{pmatrix} \Sigma_s & 0 & 0 & 0 \\ 0 & \Sigma_p & 0 & 0 \\ 0 & 0 & \Sigma_p & 0 \\ 0 & 0 & 0 & \Sigma_p \end{pmatrix} \quad (12)$$

$$\sigma_2 = \begin{pmatrix} \Sigma_{2s} & 0 & 0 & 0 \\ 0 & \Sigma_{2p} & 0 & 0 \\ 0 & 0 & \Sigma_{2p} & 0 \\ 0 & 0 & 0 & \Sigma_{2p} \end{pmatrix}$$

$$\sigma_{0'} = \begin{pmatrix} \Sigma_b' & 0 & 0 & 0 \\ 0 & \Sigma_b' & 0 & 0 \\ 0 & 0 & \Sigma_b' & 0 \\ 0 & 0 & 0 & \Sigma_b' \end{pmatrix} ,$$

and

$$\Sigma_b' = \frac{1}{4} (3\Sigma_p + \Sigma_s) . \quad (13)$$

The self energies can be obtained again from the IATA iteration procedure.

$$\Sigma = \Sigma_0 + \langle\langle T \rangle\rangle [1 + F \langle\langle T \rangle\rangle]^{-1} , \quad (14)$$

where

$$F_{ij} = \frac{1}{N} \sum_a \sum_{\vec{k}} \frac{Q_{ia}^+ Q_{aj}}{Z - E_a(Z, \vec{k})} , \quad (15)$$

with

$$(\bar{H}(\vec{k}) + \Sigma)Q = E(Z, \vec{k})Q ,$$

$$\langle\langle T \rangle\rangle = x \langle T_A \rangle + y \langle T_B \rangle ,$$

and

$$\langle T_A \rangle = x^4 t_{A_4}^A + 4x^3y t_{A_3B}^A + 6x^2y^2 t_{A_2B_2}^A + 4y^3x t_{AB_3}^A + y^4 t_{B_4}^A, \quad A \equiv \text{Si}, \quad (16)$$

with a similar expression for $\langle T_B \rangle$. Physically, for a given A atom at the center, the other four atoms in the molecular unit cell can be all A atoms, 3 A atoms and 1 B atom, 2 of each 1 A atom and 3 B atoms, or all four can be B atoms. $\langle T_A \rangle$ or $\langle T_B \rangle$ represents the configuration-averaged t-matrices, and $\langle \langle T \rangle \rangle$ is the concentration-weighted average of the configuration. By exploiting the symmetry, as seen in Eq. (11), one can reduce this problem to solving two 2x2 coupled matrix equations. Eq. (14) can be iterated to obtain Σ_s , Σ_p , Σ_{2s} , and Σ_{2p} . After every iteration, we get a new set of Σ_s , Σ_p , Σ_{2s} , Σ_{2p} , and Σ_b' : The new set has not been tested to see if Σ_b' is still given by Eq. (13). In our calculation, we did not iterate to obtain a new Σ_b' ; instead we fixed it by the relation given in Eq. (13). The error introduced by this approximation is expected to be very small. As in the case of diagonal CPA, the computation can be substantially reduced by the method of analytical continuation.⁽³²⁾

IV. DISCUSSION

A. E_0 and E_1 Optical Transition

The VCA values of E_0 ($\Gamma_{2'c} - \Gamma_{25v}$) and E_0' ($\Gamma_{15c} - \Gamma_{25v}$) and their measured values are plotted as a function of x in Fig. 1(e). Because the measurements⁽³⁶⁾ are made at room temperature, the experimental values are smaller than the values

calculated from the zero temperature band structure. Inclusion of the relativistic effects, which are not present in our calculations, is expected to form a more accurate basis for comparison with the experiments. As seen from Fig. 1(e), the theoretical and the experimental values both have a linear variation with x . Similar calculations of E_1 ($L_{1c} - L_{3'v}$) also have a linear variation on x and are in qualitative agreement with experiments.(36)

From the CPA self energies Σ_s and Σ_p , it is straightforward to calculate the correction to the VCA bands. The calculated complex band structure is plotted for $x = 0.50$ in Fig. (3). The CPA corrections are shown only in the vicinity of the band gap. The shaded portion represents the half-width of that energy state. Because s -scattering is dominant in these alloys, we see that the major disorder lies in the conduction band. The topmost valence band, with its rich p -content is least affected. The CPA band structure is used to calculate the E_0 and E_1 peak positions for $x = 0.10, 0.109, 0.15$, and 0.50 concentrations. The calculations and the data from Reference (36) show a small bowing that is not seen on the scale of Fig. 1(e).

The self energies Σ_s , Σ_p , Σ_{2p} , and Σ_{2s} are calculated in MCPA for the $x = 0.50$ alloy. As in the case of CPA, the self energies associated with s -symmetry are much larger than the ones associated with the p -symmetry. While Σ_{2s} is found to be very small, Σ_{2p} is at least an order of magnitude smaller—almost zero. However, the $\text{Im}\Sigma_s$ obtained by CPA and MCPA differ considerably. As seen from Fig. 4, the difference increases as one goes away from the band edge. Therefore, the lifetime associated with the alloy disorder is decreased by the inclusion of OD structural disorder. In addition, the OD disorder lowers the conduction band, introducing an extra bowing. The E_0 and E_1 values are reduced by 27 and 12 meV respectively. The VCA, CPA, and MCPA values of E_0 and E_1 are listed in Table III.

The half-width of the alloy states is calculated from the imaginary part of the CPA self energies. The half-width of the lowest-lying conduction band of $\text{Si}_{0.5}\text{Ge}_{0.5}$ alloy is plotted in Fig. 5 as a function of K_x in the $[100]$ direction. The calculated half-width is 186 meV for the Γ_2' state and decreases to zero at the band edge. Because of the negligible alloy broadening of the topmost valence band state, the half-width corresponding to the E_0 transition, $\Delta(E_0)$, is 186 meV, which is approximately one-half of the previously published CPA results.⁽¹³⁾ The CPA value of the half-width corresponding to the E_1 transition, $\Delta(E_1)$, is 31 meV. Because of the increase in the imaginary part of the self energies, the MCPA values of the half-widths of the E_0 and E_1 transitions are 206 meV and 32 meV respectively. Because the complete E_0 peak is not shown in the published electroreflectance spectrum⁽³⁶⁾, it is difficult to estimate the corresponding half-width. However, one can conclude from the spectrum of the $x = 0.458$ alloy that the half-width of the E_1 transition is considerably smaller (≈ 50 meV) than that of the E_0 transition. The agreement between the experimental and the theoretical values can be regarded as good because there are errors in estimating the width from the published spectra, and we have neglected the extrinsic broadening due to the apparatus used in the experiments.

In order to make a more accurate comparison with the experiments, the CPA values of $\Delta(E_0)$ and $\Delta(E_1)$ are calculated for the $x = 0.109$ alloy. The calculated half-widths of the E_0 and E_1 transitions are 13 and 2 meV respectively. From the spectrum, we estimate the corresponding values to be 8 to 15 meV and 3 to 6 meV. We see that CPA values are in excellent agreement with these experiments. Because x is small, the inclusion of off-diagonal disorder is not expected to change the calculated values significantly.

B. Energy Gap

The fundamental gaps of these alloys are calculated as a function of concentration. The VCA gap is an increasing function of x with a slope discontinuity at $x \simeq 0.11$. The conduction band minimum changes from L-point to X(Δ)-point at this crossover. In addition to the band gap, the effective electron masses and the band edge K_0 are also calculated. When the X(Δ) gap is preferred, the band edge moves linearly from \vec{k} at $(0.9,0,0)_{x=0.15}$ to $(0.8,0,0)_{x=1}$. The effective masses at a given minimum increase linearly from their pure germanium values to the corresponding pure silicon values.

Using CPA self energies, the band gap, band masses, and the band edge are also calculated. The position of the band minimum did not change by virtue of the inclusion of off-diagonal disorder. While the effective transverse mass remains almost the same as the VCA value, the longitudinal mass has a maximum of 12% enhancement. Because the real part of CPA self energies is negative in the forbidden gap region, an extra bowing is introduced to the VCA energy gap. Because of this bowing, the L-X(Δ) crossover takes place near $x \simeq 0.13$. The VCA, CPA, and experimental⁽³⁶⁾ bowing parameters are 0.06, 0.18 and 0.24 respectively. The calculated energy gap is plotted as a function of x in Fig. 6.

Because of the negligible change in the effective masses, the corresponding values in the pure materials are used in the calculation of the alloy-scattering-limited electron mobility. The CPA X-gap E_g^X and L-gap E_g^L are fitted to a polynomial form. The generalized Brooks' formula that is applicable to the alloys with an indirect gap and multiple bands is used.⁽¹⁵⁾ The calculated electron drift mobility and the experimental Hall mobility⁽¹⁾ are plotted in Fig. 7, where the theory explains the qualitative behavior of experimental results.⁽¹⁾ As observed,⁽⁵⁾ even a few percent alloy concentration can reduce the drift mobility substantially. It can be seen that the rate of decrease near

0 and $x = 1$ are quite different. This is because the L-edge has more s content than the X-edge. Because the s scattering is dominant in these alloys, the L electrons are scattered more than the X electrons. Precisely for this reason, one observes a dip in the mobility near the L to X(Δ) crossover. For $x < 0.13$, the minimum gap is the L gap. After the crossover, the minimum gap is the X(Δ) gap, and the reduced alloy scattering increases the average mobility. For still larger x , the mobility decreases because of the increased alloy disorder. All these features are clearly seen in Fig. 7. While our calculations include the inter-valley scattering mediated by alloy disorder, the effect of other scattering mechanisms is expected to increase the dip near the crossover.

The calculated alloy scattering rate for the holes is several orders smaller than that for the electrons, because (1) the valence band edge has dominant p content, (2) the p-scattering parameter ($\Delta\epsilon_p = 0.21$) is only 1/7 of $\Delta\epsilon_s$, which alone decreases the scattering rate for holes by a factor of 50, and (3) finally, the imaginary part of the self-energy is proportional to the density of states, which approaches zero at the band edge. Hence, the hole mobility in this system is insensitive to alloy disorder.

In MCPA, the conduction band is pushed down, because of an increase in the imaginary part of the self energy, giving rise to an additional bowing in the fundamental gap. For an $x = 0.50$ alloy, the gap is reduced by 7 meV. The bowing parameter, including the MCPA correction, is 0.21, which is in excellent agreement with experiment.⁽³⁷⁾

It is interesting to compare the results of our calculations with those of Hass et al.⁽³⁴⁾ In their calculations on the $\text{Ga}_{1-x}\text{In}_x\text{As}$ alloy, CPA introduced an extra bowing in the fundamental gap. However, after the MCPA corrections, the total scattering was diminished and the results were similar to VCA results. These results were explained in terms of the relative strength and sign of the atomic term values and V_2^{AB} . We extend

their argument to $\text{Si}_x\text{Ge}_{1-x}$ alloys. The hybrid level of silicon is higher than that of germanium. Because of its shorter bond length, the V_2 of silicon is larger than that of germanium. Thus, in this case, both effects combine to give more disorder in the conduction and valence bands. Therefore, the scattering is enhanced in these alloys. This explains the increase in the imaginary part of the self energy due to inclusion of OD disorder in our calculation.

In conclusion, we have incorporated both chemical and structural disorder into the calculation of the CPA band structure of $\text{Si}_x\text{Ge}_{1-x}$ alloys. The calculation, based on a realistic band structure of silicon and germanium, suggests that the band gap is an increasing function of x with a slope discontinuity at $x \simeq 0.13$. The linewidths of the E_0 and E_1 transitions calculated by CPA and MCPA are in good agreement with experiments. Addition of the structural disorder to the diagonal CPA decreases the band gap slightly but increases the s -part of the self energy considerably over certain energy ranges. The calculated alloy-scattering-limited electron-drift mobility is in qualitative agreement with the observed Hall mobilities.

ACKNOWLEDGMENTS

This work was supported in part by Grant AFOSR-84-0282 and DARPA/AFOSR PR: FQ8671-851100. A.-B. Chen would like to thank Professor W.E. Spicer for his hospitality at Stanford University.

REFERENCES

- ¹M. Glicksman, Phys. Rev. *111*, 125 (1958); Phys. Rev. *100*, 1146 (1955).
- ²B.A. Bunker, S.L. Hulbert, J.P. Stotl, and F.C. Brown, Phys. Rev. Lett. *53*, 2157 (1984).
- ³H.J. Lee, L.Y. Juravel, and J.C. Woolley, Phys. Rev. *B21*, 659 (1980).
- ⁴N. Lifshitz, A. Jayaraman, and R.A. Logan, Phys. Rev. *B21*, 670 (1980).
- ⁵H.M. Manasevit, I.S. Gergis, and A.B. Jones, Appl. Phys. Lett. *41*, 464 (1982); J. Elec. Materials *12*, 637 (1983).
- ⁶S. Krishnamurthy and J.A. Moriarty, Superlattices and Microstructures *1*, 209 (1985); Phys. Rev. *B* in press (1985).
- ⁷J.C. Bean, L.C. Feldman, A.T. Flory, S. Nakahara, and I.K. Robinson, J. Vac. Sci. Technol. *A2*, 436 (1984).
- ⁸R. People, J.C. Bean, D.V. Lang, A.M. Sergent, H.L. Stormer, K.W. Wecht, R.T. Lynch, and K. Baldwin, Appl. Phys. Lett. *45*, 1231 (1984).
- ⁹F. Cerdeira, A. Pinczuk, and J.C. Bean, Phys. Rev. *B31*, 1202 (1985).
- ¹⁰T.P. Pearsall, F.H. Pollak, and J.C. Bean, Bull. Am. Phys. Soc. *30*, 266 (1985).
- ¹¹K.E. Newman and J.D. Dow, Phys. Rev. *B30*, 1929 (1984).
- ¹²M.Z. Huang and W.Y. Ching, Superlattices and Microstructures *1*, 137 (1985).

- 13D. Stroud and H. Ehrenreich, Phys. Rev. *B2*, 3197 (1970).
- 14S. Krishnamurthy, A. Sher, and A.-B. Chen, Phys. Rev. Lett., in press (July 1985).
- 15S. Krishnamurthy, A. Sher, and A.-B. Chen, Appl. Phys. Lett., in press (1985).
- 16A.-B. Chen and A. Sher, Phys. Rev. *B22*, 3886 (1980).
- 17E.O. Kane, Phys. Rev. *B13*, 3478 (1976).
- 18D.J. Chadi, Phys. Rev. *B16*, 3572 (1977).
- 19A.-B. Chen and A. Sher, Phys. Rev. *B23* 5360 (1981).
- 20A.-B. Chen and A. Sher, Phys. Rev. *B26*, 6603 (1982).
- 21R.R.L. Zucca, J.P. Walter, Y.R. Shen, and M.L. Cohen, Solid State Commun. *8*, 627 (1970).
- 22R.R.L. Zucca and Y.R. Shen, Phys. Rev. *B1*, 2668 (1970).
- 23M. Welkowsky and R. Braunstein, Phys. Rev. *B5*, 497 (1972).
- 24R.A. Pollak, L. Ley, S. Kowalczyk, D.A. Shirley, J. Joannopoulos, D.J. Chadi, and M.L. Cohen, Phys. Rev. Lett. *29*, 1103 (1973).
- 25L. Ley, R.A. Pollak, F.R. McFeely, S.P. Kowalczyk, and D.A. Shirley, Phys. Rev. *B9*, 600 (1974).
- 26W.D. Grobman and D.E. Eastman, Phys. Rev. Lett. *29*, 1508 (1972).
- 27D.E. Eastman, W.D. Grobman, J.L. Freeouf, and M. Erbudak, Phys. Rev. *B9*, 3473 (1974).

- 28W.E. Spicer and R.C. Eden, *Proceedings of the Ninth International Conf. Phys. Semiconductors*, 1968 (Nauka, Leningrad, 1969), Vol. 1, p. 61.
- 29G. W. Gobeli and F.G. Allen, *Phys. Rev. A* **24**, 137 (1965).
- 30J.R. Cheliskowsky and M.L. Cohen, *Phys. Rev. B* **14**, 556 (1976); and the references cited therein.
- 31J.A. Moriarty and S. Krishnamurthy, *J. Appl. Phys.* **54**, 1892 (1983).
- 32K.C. Hass, B. Velicky, and H. Ehrenreich, *Phys. Rev. B* **29**, 3697 (1984).
- 33F. Ducastelle, *J. Phys. C* **7**, 1795 (1974).
- 34K.C. Hass, R.J. Lampert, and H. Ehrenreich, *Phys. Rev. Lett.* **52**, 77 (1984).
- 35W.A. Harrison, *Electronic Structure and the Properties of Solids*, (W.H. Freeman and Co., San Francisco, 1980) p. 65.
- 36J.S. Kline, F.H. Pollak, and M. Cardona, *Helv. Phys. Acta.* **41**, 968 (1968).
- 37R. Braunstein, A.R. Moore, and F. Herman, *Phys. Rev.* **109**, 695 (1958).

TABLE I. Pseudopotential form factors
and the band parameters (in eV).

Parameter	Silicon	Germanium
$V(\sqrt{3})$	~ 2.872	$- 2.872$
$V(\sqrt{4})$	0.124	0.124
$V(\sqrt{8})$	0.638	0.638
$V(\sqrt{11})$	0.109	0.109
Δ_s	-16.175	-16.922
Δ_p	-16.109	-14.971
V_{ss}	~ 0.111	0.131
V_{sp}	0.040	0.150
V_{xx}	0.025	0.030
V_{xy}	0.050	0.100

TABLE II. Band structure of silicon and germanium

(all energies are expressed in eV).

Bands	Silicon		Germanium	
	Calculated	EXPTL ^a /EPM ^b	Calculated	EXPTL ^a /EPM ^b
Γ_1	-12.60	-12.4 ± 0.6	-12.56	-12.6 ± 0.3
L_{2v}	-10.26	-9.3 ± 0.4	-10.74	-10.6 ± 0.5
L_{1v}	-6.99	-6.8 ± 0.2	-7.65	-7.4 ± 0.3
X_{1v}	-8.29		-9.20	
X_{4v}	-2.55		-2.55	
$L_{3'v}$	-1.11	-1.2 ± 0.2	-1.13	-1.1 ± 0.2
Γ_{25v}	0.0	0.0	0.0	0.0
L_{1c}	2.24		0.76	0.76
$\Gamma_{2'c}$	4.10	4.00 ± 0.05	0.99	0.99
Γ_{15c}	3.43	3.40	3.24	
X_{1c}	1.34	1.17	0.95	
$L_{3'c}$	4.34		4.16	
E_g	1.11	1.11	0.76	0.76
K_0	(0.8,0.0)	(0.8,0.0)	(0.5,0.5,0.5)	(0.5,0.5,0.5)
m_{el}^*	0.89	0.91	1.09	1.59
m_{et}^*	0.16	0.19	0.077	0.082
m_v^*	0.35	0.50	0.28	0.34

(a) References 21-28

(b) Reference 30

TABLE III. Calculated values of E_0 , E_1 and their respective half-widths

$\Delta(E_0)$ and $\Delta(E_1)$ (all energies are in eV).

X	Quantity	VCA	CPA	MCPA
0.10	E_0	1.290	1.248	--
	$\Delta(E_0)$		0.011	--
	E_1	2.016	1.995	--
	$\Delta(E_0)$		0.001	--
0.109	E_0	2.028	2.009	--
	$\Delta(E_0)$		0.013	--
	E_1	1.318	1.275	--
	$\Delta(E_1)$		0.002	--
0.15	E_0	1.442	1.382	--
	$\Delta(E_0)$		0.032	--
	E_1	2.083	2.051	--
	$\Delta(E_1)$		0.002	--
0.50	E_0	2.517	2.418	2.391
	$\Delta(E_0)$		0.186	0.206
	E_1	2.578	2.510	2.498
	$\Delta(E_1)$		0.0308	0.0319

FIGURE CAPTIONS

- FIG. 1. Calculated VCA band structures of (a) silicon, (b) germanium, (c) $\text{Si}_{0.5}\text{Ge}_{0.5}$ alloys, and (d) $\text{Si}_{0.10}\text{Ge}_{0.90}$. (e) Calculated VCA values (solid) and the experimental values (dashed) of the E_0 and E_0' peak positions are plotted as a function of alloy concentration x .
- FIG. 2. The variation of the imaginary part of the self energy Σ_i (CPA) as a function of energy for $x = 0.50$.
- FIG. 3. Calculated CPA complex band structure of the $\text{Si}_{0.5}\text{Ge}_{0.5}$ alloy. Only the bands in the vicinity of the energy gap are shown. The shaded portion represents the alloy broadening.
- FIG. 4. Imaginary part of Σ_i (CPA) and Σ_i (MCPA) as a function of energy for $x = 0.50$ alloy.
- FIG. 5. The variation in the width of the lowest lying conduction band as a function of K_x in the $[100]$ direction for the $x = 0.50$ alloy.
- FIG. 6. The variation of the VCA energy gap (dash-dotted) and the CPA energy gap (solid) as a function of x .
- FIG. 7. Calculated drift mobility (solid) and the experimental (dashed) Hall mobility (Reference 1) as a function of x .

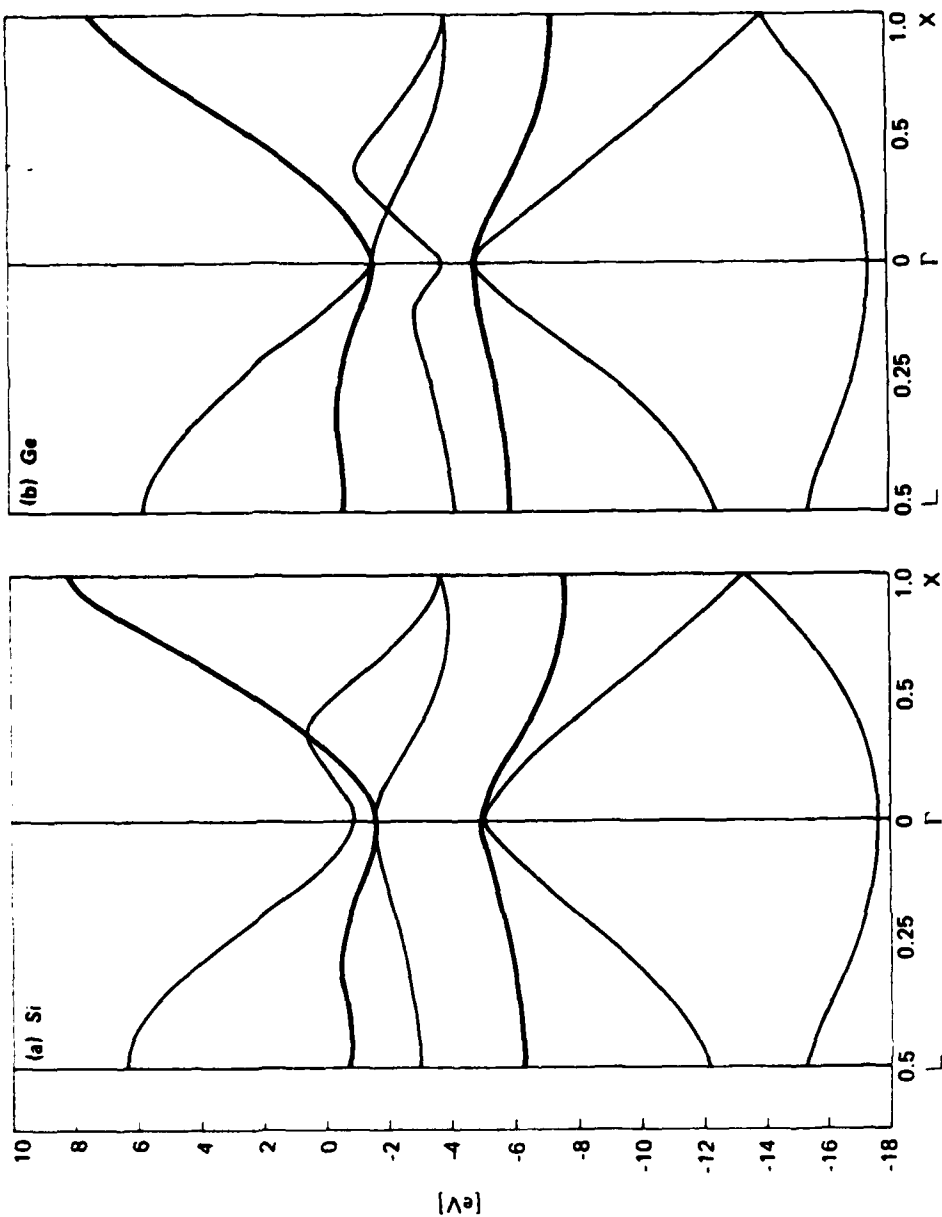


FIGURE 1

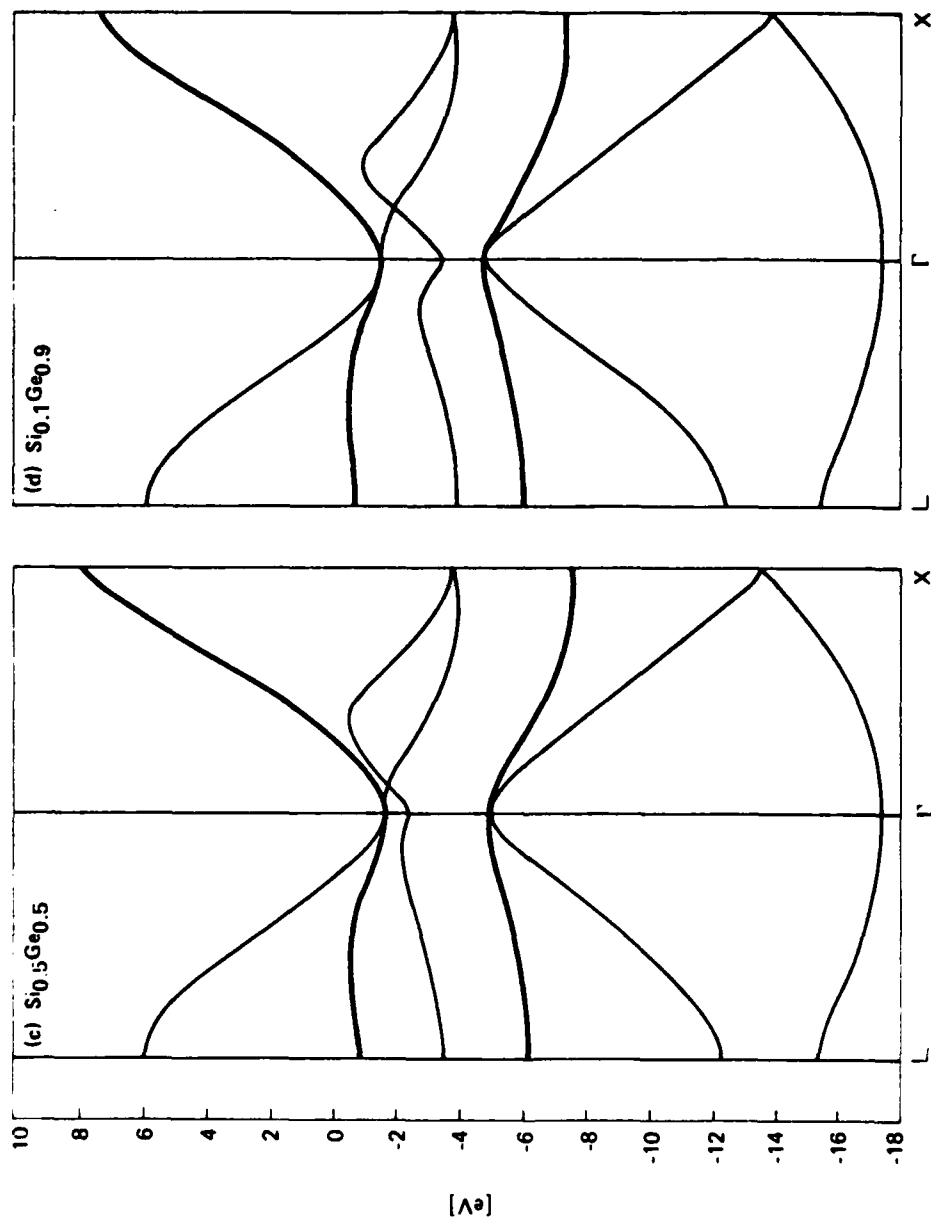


FIGURE 1 (cont'd)

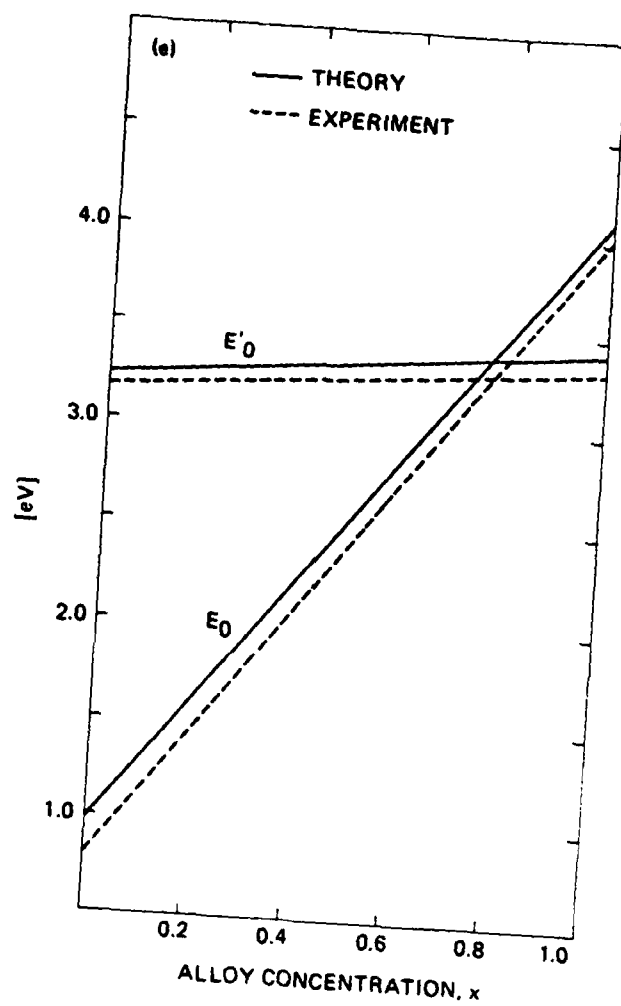


FIGURE 1 (concluded)

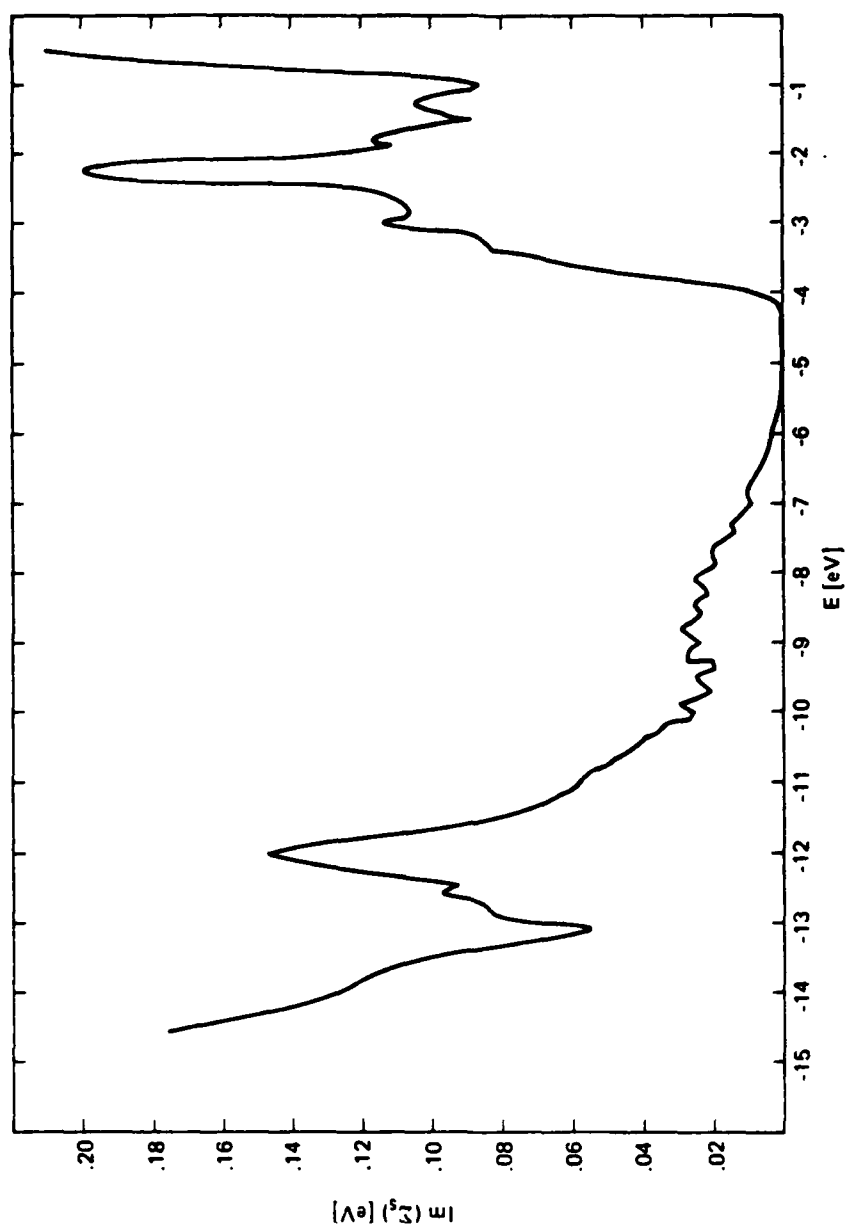


FIGURE 2

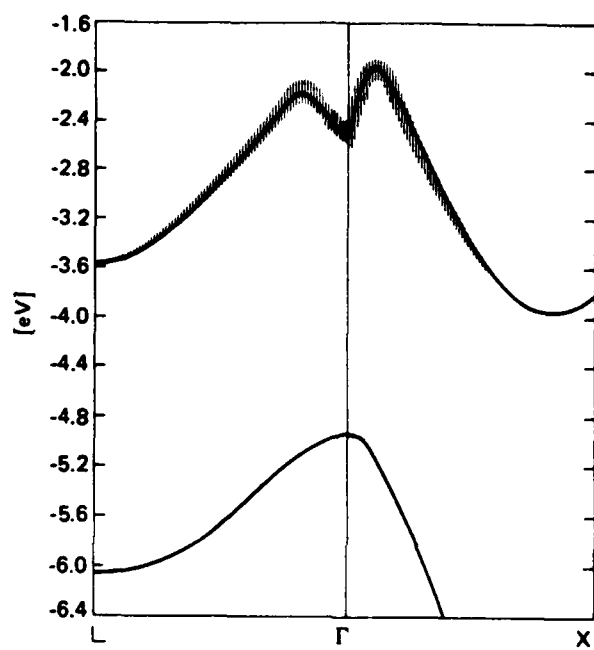


FIGURE 3

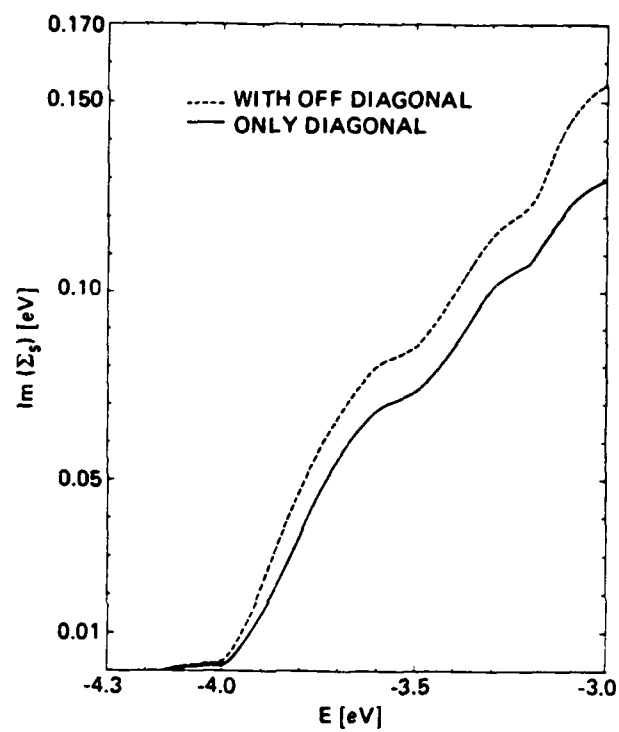


FIGURE 4

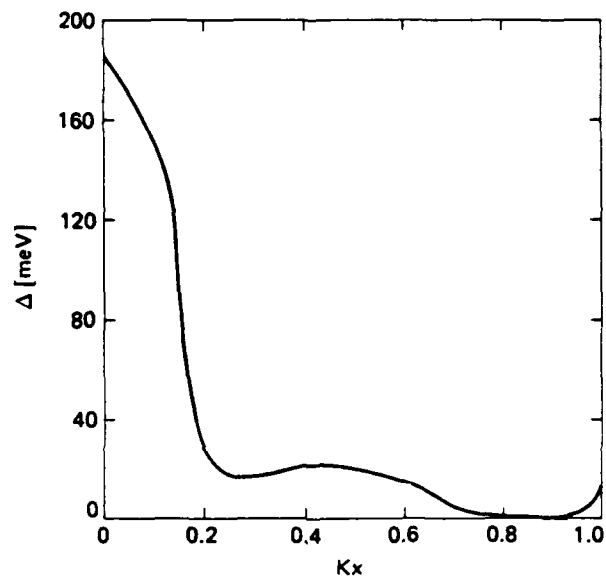


FIGURE 5

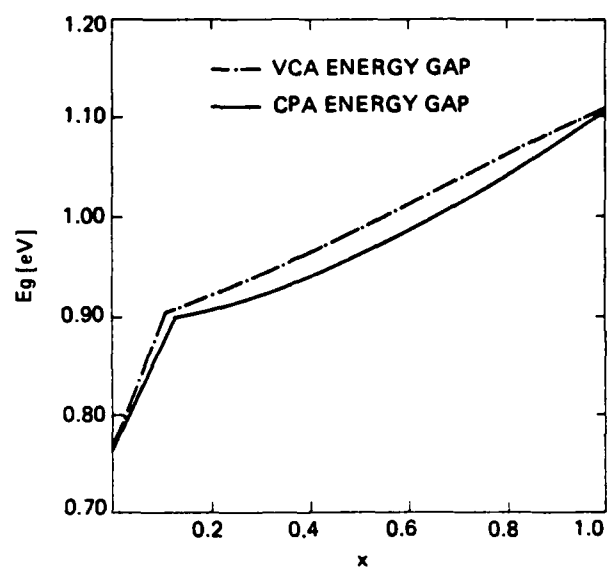


FIGURE 6

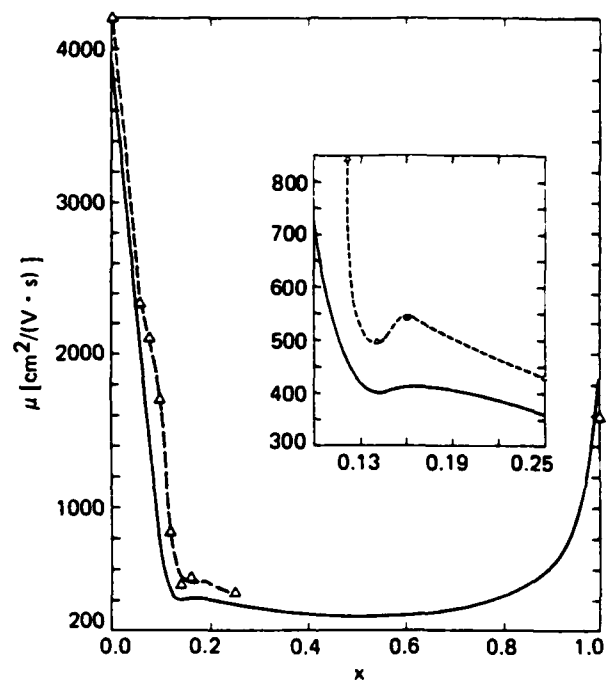


FIGURE 7

END

FILMED

6-86

DTIC